Design of Silica-Collagen Nanocomposite for Corneal Replacement

A DISSERTATION
SUBMITTED TO THE FACULTY OF
UNIVERSITY OF MINNESOTA
BY

Michael Dominick DiVito

IN PARTIAL FULFILLMENT OF THE REQUIREMENTS
FOR THE DEGREE OF
DOCTOR OF PHILOSOPHY

Allison Hubel, Ph.D., Advisor

September 2015

Some of the work in this dissertation has been published previously:

Chapter 6
Rudisill, SG, DiVito MD, Hubel A, & Stein A. In vitro collagen fibril alignment via incorporation of nanocrystalline cellulose. *Acta biomaterialia.* 2015;12: 122-128.

Chapter 7
DiVito MD, Rudisill SG, Stein A, Patel SV, McLaren JW, & Hubel A. Silica hybrid for corneal replacement: optical, biomechanical, and ex vivo biocompatibility studies. *Investigative ophthalmology & visual science*. 2012; 53(13): 8192-8199.

Acknowledgements

I acknowledge every person who has contributed their time and effort toward this project.

DR. SANJAY PATEL, DR. JAY McLAREN, and the ophthalmology department at Mayo Clinic performed *ex vivo* biocompatibility studies and confocal backscatter measurements. DR. ANDREAS STEIN and DR. STEPHEN RUDISILL were the main contributors to the concept, experimentation, and writing process of the nanocrystalline cellulose-collagen experiments. Additionally, their expertise in chemistry and nanomaterials was valuable in the development of silica-collagen nanocomposites. GAIL CELIO and FANG ZHOU prepped and obtained TEM images of collagen hydrogel cross-sections. NICK SEATON trained and assisted me with SEM. SPENCER LAKE trained and offered guidance on tensile testing of collagen hydrogels. DR. BETH STADLER, ANDREW BLOCK, and DANIEL SHORE synthesized nanowires, performed polarized light transmittance experiments, and helped with the manuscript writing process for nanowire-collagen studies. DR. ANIRUDH SHARMA was an equal contributor toward the concept, experimentation, and writing of nanowire-collagen studies.

Special thanks goes to all of my past and present lab members, especially DR. JUNJIE ZHU, GUANGLIN YU (performed Raman spectroscopy on silica-collagen hydrogels), and KATIE POLLOCK (trained me on cell culture, edited manuscripts and this dissertation). Also, I greatly appreciate the time my committee members DR. RUSEN YANG, DR. JOAN BECHTOLD, and DR. MICHAEL McALPINE have contributed during the preliminary and final exam process.

ALLISON HUBEL has been an exceptional and patient advisor and key in my development as a researcher. I am very grateful for the opportunity to be part of MS. HUBEL'S lab and wish to especially thank her for the unwavering support over the past five years.

Finally, I would like to thank all of my friends and family who have given me so much love and encouragement during my time in graduate school.

Dedication

I would like to dedicate this work to my loving parents, Donna and Michael DiVito, as well as my three sisters, Michel Harris, Carly DiVito, and Jenna DiVito.

Abstract

The cornea is the most commonly transplanted tissue in the United States. Globally, corneal diseases are the second leading cause of blindness[1]. Due to strict FDA regulations, lack of eye banking facilities, and other factors which limit the supply of donor tissue[2,3], designing an artificial cornea made of readily available materials is of great interest. The synthetic constructs that are currently clinically available in the United States have had moderate success, but biocompatibility issues such as stromal melting and epithelial defects are still common[4–7].

When considering a potential material for corneal replacement, it must meet the design criteria of the normal functioning cornea. The relevant design criteria can be broken down into three main groups: optical behavior, biomechanical properties, and biocompatibility. The presented work proposes silica-collagen nanocomposites as a viable candidate material to meet these design criteria. A bottom-up approach starting from the molecular level is utilized to modify the surface chemistry and physical properties of collagen fibrils. In doing so, methodologies are presented which allow for fine-tuning of optical, biomechanical, and biodegradation behavior.

The first part of this work validates the theory that light scattering of collagen hydrogels is heavily dependent on the change in the material's index of refraction over length scales comparable to the wavelength of incident light. This work shows that light scattering of collagen hydrogels can be minimized by a rapid neutralization technique, and by the addition of nanocrystalline cellulose. Additionally, collagen hydrogels with embedded magnetic nanowires can be polarized to form an aligned fibril microstructure and show an increase in light transmission.

The second part of this thesis characterizes the mechanical and optical behavior, as well as the biocompatibility of silica-collagen nanocomposites. This work shows that a

copolymerization method can be used to make implants which have improved biomechanical properties (when compared to pure collagen hydrogels) and can be re-epithelialized in an *ex vivo* rabbit model. Additionally, an improved two-step process for silica deposition onto collagen fibrils is presented. This new method shows that poly-L-lysine can be used to induce a uniform silica shell around collagen fibrils in the absence of large silica aggregates. This new method increases mechanical stiffness and enzymatic degradation resistance without producing any additional light scattering in the material.

Silica-collagen nanocomposites show great potential in the context of corneal replacement. The methods developed and results presented here can be useful for improving any collagen-based corneal replacement, as well as in other applications such as drug delivery and silica nanoparticle templating.

Table of Contents

List of Tables

List of Figures

Abbreviations and Symbols

α	Confidence coefficient
α_c	Beer-Lambert coefficient
ν	Degrees of freedom
λ	Incident light wavelength
θ	Polarization angle
APTES	3-aminopropyltriethoxsilane
ARVO	Association for Research in Vision and Ophthalmology
Au	Gold
B	Magnetic field vector
CDI	N,N'-Carbonyldiimidazole
CO_2	Carbon dioxide
COL	Type I collagen
COOH	Carboxylic acid group
CRM	Confocal reflectance microscopy
d	Path length
DI	Deionized
DIC	Differential interference contrast
DMEM	Dulbecco's modified eagle's medium
EDX	Energy dispersive X-ray spectroscopy
FBS	Fetal bovine serum
FDA	Federal drug administration

FITC	Fluorescein isothiocyanate
FTIR	Fourier transform infrared spectroscopy
He	Helium
HFF	Human foreskin fibroblast
IPN	Interpenetrating network
KBr	Potassium bromide
KPro	Keratoprosthesis
MCC	Microcrystalline cellulose
NCC	Nanocrystalline cellulose
Ne	Neon
Ni	Nickel
N	Number of samples
O	Oxygen
PBS	Phosphate buffered saline
PEG	Poly(ethylene glycol)
PI	Propidium iodide
PKP	Penetrating keratoplasty
PLL	Poly(L-lysine)
PMMA	Poly(methyl methacrylate)
Pt	Platinum
R	Water/silica precursor molar ratio
s.d.	Standard deviation

SEM	Scanning electron microscopy
Si	Silicon
T	Transmittance
t	Two-sided t-distribution value
TEM	Transmission electron microscopy
TEOS	Tetraethyl orthosilicate
TRITC	Tetramethylrhodamine isothiocyanate
UTS	Ultimate tensile strength
UV	Ultraviolet light
VIS	Visible light

Units

°	Angular degrees
cm	Centimeters
°C	Degrees Celsius
g	Grams
Hz	Hertz
h	Hour
kPa	Kilopascals
kV	Kilovolts
MPa	Megapascals
µg	Micrograms
µL	Microliters
µm	Micrometers
mg	Milligrams
mL	Milliliters
mm	Millimeters
mM	Millimoles per liter
mW	Milliwatts
min	Minutes
M	Moles per liter
nm	Nanometers
rpm	Revolutions per minute

s	Seconds
U	Units
W	Watts

Chapter 1

Introduction

1.1 Motivation

The cornea is the most commonly transplanted tissue in the United States[8] and corneal disease is the second leading cause of blindness throughout the world[1]. Over 40,000 corneal transplants are performed annually in the United States alone. On a global scale, the supply of donor tissue has never met transplant demands. In many parts of the world, this mismatch is due to a lack of eye banking facilities. However, even in places with eye banking facilities like the United States, donor tissue supply is limited by quality and safety considerations. An increasing number of organ donors are ineligible to donate corneal tissue due to previous refractive and cataract surgery[3], and organ donation from subjects with common viral infections (e.g. hepatitis B)[2] is considered unsafe in general.

Due to these supply limitations, there exists a great need for artificial corneal tissue made from readily available materials which does not require eye-banking resources. Artificial corneas that are currently available (keratoprostheses) do not truly biointegrate with the surrounding native tissue[9,10]. More specifically, fully synthetic implants do not allow for re-epithelialization on the anterior surface, and ingrowth of host tissue around the periphery is limited or non-existent. While surgical techniques and implant designs have improved to allow for higher short-term success rates with limited complications, these host-implant interactions have proven to be vital for long-term implant stability.

Because of synthetic materials' poor biointegration, a regenerative approach to corneal replacement has been recently adopted. Natural materials such as collagen scaffolds have been designed *in vitro,* and unlike synthetic polymers have the ability to host native cells. This cell-

scaffold interaction allows for remodeling of the implant, and promotes complete integration with the host tissue. There has been some in-vivo integration success with chemically cross-linked collagen hydrogels[11,12], but only a handful of clinical procedures have been reported for partial thickness transplantation and none for full thickness replacements.

The native cornea is primarily composed of type I collagen, and some of the most successful artificial corneas to date are collagenous hydrogels[11,12]. Collagen hydrogels made *in vitro* often have insufficient mechanical properties and degrade rapidly, and chemical cross-links or addition of other synthetic materials are necessary to match corneal specifications[13]. Silica is one such addition, and silica-collagen hybrid materials have been produced using the sol-gel process[14–22]. The addition of silica using the sol-gel procedure is attractive as networks of silica can be synthesized from different molecular precursor solutions in a variety of chemistries. Silica-collagen composites have been proven to possess sufficient biocompatibility[14,18–20], as well as tunable mechanical[19] and biodegradation behavior[23–29]. As artificial corneal replacement requires a material whose small-scale features can be tuned and controlled efficiently, silica-collagen composites represent a widely available and easily tunable design choice.

1.2 Hypothesis and aims

The long-term objective of this project is to create an artificial cornea with sufficient mechanical, optical, and biological properties to operate as a long term, full thickness corneal replacement. We hypothesized that chemical and microstructural properties of silica-collagen composites can be tuned to yield favorable mechanical and degradation behavior for corneal replacement without reducing the optical properties of the hydrogel. This hypothesis produced the following aims:

(1) **Tune optical properties of collagen hydrogels by modulating and characterizing relevant microstructural features: fibril diameter, spacing, and orientation.** Chapters 4-6 address this aim by showing how neutralization methods, collagen concentrations, and additives (i.e. nanocrystalline cellulose, magnetic nanowires) affected collagen network features and light scattering behavior.

(2) **Tune mechanical and degradation properties of transparent collagen hydrogels without reducing optical properties via silica deposition onto collagen fibrils.** Chapter 7 describes a copolymerization method while Chapter 8 introduces a two-step process to produce silica-collagen composites. The resulting microstructures and bulk behaviors of the composites were evaluated.

After addressing these specific aims, it was found that ammonia vapor neutralization produces collagen hydrogels with favorable microstructure for appropriate optical transparency. Additionally, the transparency of hydrogels using this method can be improved when fibril alignment is induced using magnetic nanowires and nanocrystalline cellulose. Two methods of silica addition were shown to significantly improve the mechanical properties of collagen gels. However, the two-step process was superior because it produced transparent hydrogels composed of collagen fibrils with uniform coatings of silica, which acts as a barrier against enzymatic degradation. A suitable material for corneal replacement can be obtained with additional optimization experiments using the methods presented in this work to modulate collagen concentration, induce fibril arrangement, and apply uniform coatings of silica onto fibril surfaces.

Chapter 2

Background

2.1 Cornea

The cornea is the transparent connective tissue located at the anterior of the eye, which protects the eye from infection and structural damage while providing approximately 70% of the eye's total refracting power[30]. The cornea's ultrastructure is composed of five layers. The layer most relevant to this project is the stroma, which makes up approximately 90% of the cornea's thickness[31–33]. The stroma acts as the main structural component of the cornea and is composed of type I/V collagen fibrils that are orientated in a highly organized lamellar structure[32,34] (Figure 2.1). The fibrils are evenly spaced at about 60 nm apart in a close packed hexagonal array, and each fibril is approximately 30 nm in diameter[31,34,35]. This uniform spacing is maintained by proteoglycans which form interfibrillar crosslinks and also help regulate hydration[32]. Within the network of collagen fibrils are keratocytes, which maintain the environment of the stroma by remodeling collagen fibrils and proteoglycans.

While the stroma is the layer that makes up the bulk of the tissue, the other layers play a significant role in the function of the cornea. For instance, the anterior and posterior surfaces of the cornea are composed of an epithelial and endothelial cell layer, respectively. The epithelial layer is vital for preventing infection of the deeper parts of the cornea, as well as maintaining an even tear film on the surface of the eye. The endothelial layer is a monolayer of flat cells that are tightly adhered to one another, controlling ion flux, and therefore the osmotic gradient, across the cornea. This control of hydration is vital for the cornea to maintain its transparency. Upon damage, excess hydration can result in edema, causing the cornea to become opaque[36–38].

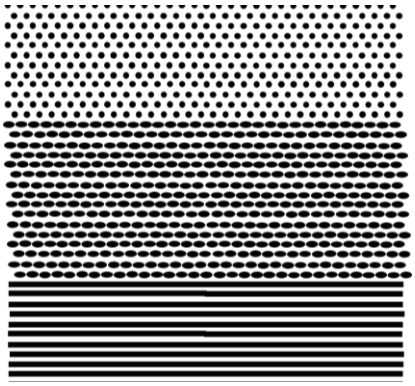

Figure 2.1: Illustration depicting cross-section of corneal stroma. Each lamellae is 1-2 µm in thickness, and the fibrils within each lamellae take on a given direction (dots represent cross fibrils oriented perpendicular to the page, straight lines represent fibrils oriented parallel to the page, and ellipses are fibrils oriented that form an oblique angle with the page)

The main challenge in developing a corneal replacement is recapitulating the critical unique optical and mechanical properties of the cornea. Figure 2.2 shows the spectral transmittance curve for the human cornea reported by van den Berg and Tan[39], and Walsh et al.[40]. The two curves reported by van den Berg and Tan represent two different acceptance angles used for light transmittance experiments. The significant difference between these two curves is a prime example of how reported optical properties are sensitive to measuring apparatus parameters. However, the curve of the spectral light transmission curve in this range should always behave like a low-pass filter in the cornea, resulting in significant attenuation of UV light followed by significant transmittance of light in the visible spectrum.

Table 2.1 lists estimates of mechanical properties of the human cornea reported by different authors. Similar to optical properties of the cornea, there have been a wide range of mechanical property values reported for the cornea. This is due to the cornea's viscoelastic behavior which is sensitive to strain rate. The cornea's nonlinear behavior results in strain

dependence for moduli values as well. Other factors such as the geometry and dimensions of the specimen, as well as the excising technique and hydration can affect mechanical measurement. With all of these factors considered, it is important to understand the experimental protocols associated with moduli and UTS values.

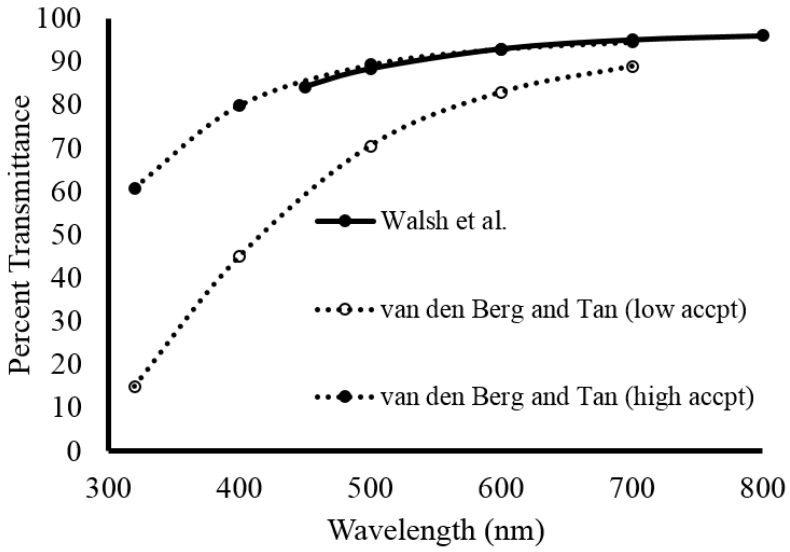

Figure 2.2: Spectral transmittance of human cornea for detectors with different acceptance angles[39]*, and intact rabbit cornea*[40]*.*

Table 2.1: Mechanical properties of the cornea previously published

Authors	Protocol Details	Modulus	Ultimate Tensile Strength
Elsheikh and Anderson[41]	0.1% strain/second	at 1% strain: 0.1 MPa at 10% strain: 2.0 MPa	~10 MPa
Andreassen et al.[42]	4.8 % strain/second	> 10% strain: 57 MPa	~12.7 MPa
Nash et al.[43]	-	at 1% strain: 0.5 MPa at 2.5% strain: 1.3 MPa	-
Hoeltzel et al.[44]	< 0.1% strain/second	< 1% strain: 0.34 MPa 2% strain: 4.1 MPa	-
Wollensak et al.[45]	0.3% strain/second	4% strain: 0.8 MPa 6% strain: 1.3 MPa 8% strain: 2.2 MPa	-

Figure 2.3 shows the *in vitro* degradation behavior for human corneas from experiments performed by Liu et al.[46]. These samples were exposed to a diluted collagenase solution and residual sample mass measurements were made at advancing time points. By using similar experimental conditions, artificial material degradation can easily be compared to the native cornea's degradation *in vitro*. One can see that the cornea experiences large amounts of swelling followed by a significant reduction of mass within 4 days of collagenase exposure.

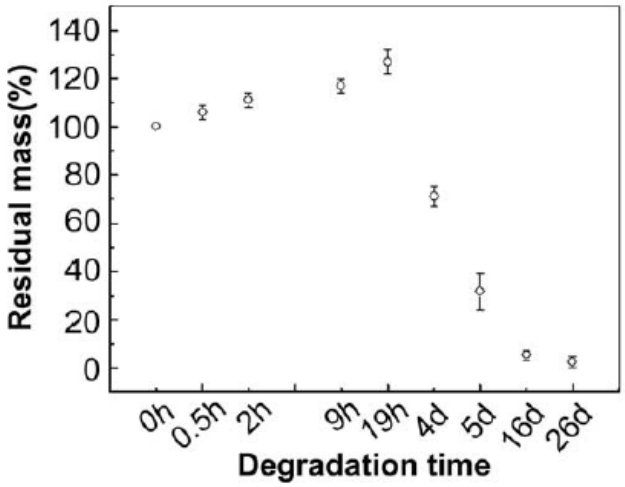

Figure 2.3: Residual mass of human cornea when exposed to collagenase in vitro reported by Liu et al.[46]

Collagen hydrogels with collagen concentrations similar to the concentrations found in the native cornea do not possess the transparency that the cornea does in the visible light spectrum, and degrade rapidly when they are not chemically cross-linked. Therefore, using silica to enhance the mechanical properties while increasing the enzymatic degradation resistance of collagen hydrogels will allow for lower, and more transparent collagen concentrations to be used.

If the optical properties of concentrated collagen gels are improved, the introduction of silica should not contribute significantly to light scattering.

2.2 Corneal Replacements

2.2.1 Penetrating keratoplasty (PKP)

PKP is the most successful tissue transplantation procedure. However, there is a shortage of eligible transplantable tissue, magnified by a lack of eye banking facilities. This is an even greater problem in under developed countries. In the United States, strict FDA regulations which require testing for the presence of specific viruses limit the donor pool[2]. The recent surge of refractive eye surgery (which deems tissue ineligible for transplantation) has also depleted the amount of donor tissue available[47]. There is a growing need for an artificial material that will eliminate the dependence on the human tissue supply.

2.2.2 Keratoprostheses (KPros)

KPros are currently available for patients who are at high risk of failure with PKP. Dohlman and Doan used a PMMA front and back plate which sandwiched a skirt ring made of donor cornea tissue[48]. This device is now known as the Boston KPro and is arguably the best performing KPro in clinical use[49]. Various groups have reported on the performance of this device in the past decades. The short-term retention rate has improved greatly, but complications such as severe glaucoma, epithelial defects, and stromal melting still occur, especially at longer time points post surgery[4–7,50]. FDA approval for clinical use of the Boston KPro was granted in 1992, and it has since become the most commonly used KPro in the United States. The Chirila KPro, now known as the AlphaCor device, is the only other KPro that has received FDA approval in the United States[51,52]. The schematics of both KPros are shown in Figure 2.4. This hydrogel

alternative is composed entirely of poly(2-hydroxyethyl methacrylate). The clear center optic and porous opaque skirt are chemically identical, but different in their physical properties[53]. Varying degrees of retention were shown after three years, but stromal melting was a common problem amongst surgeons[51,54–56].

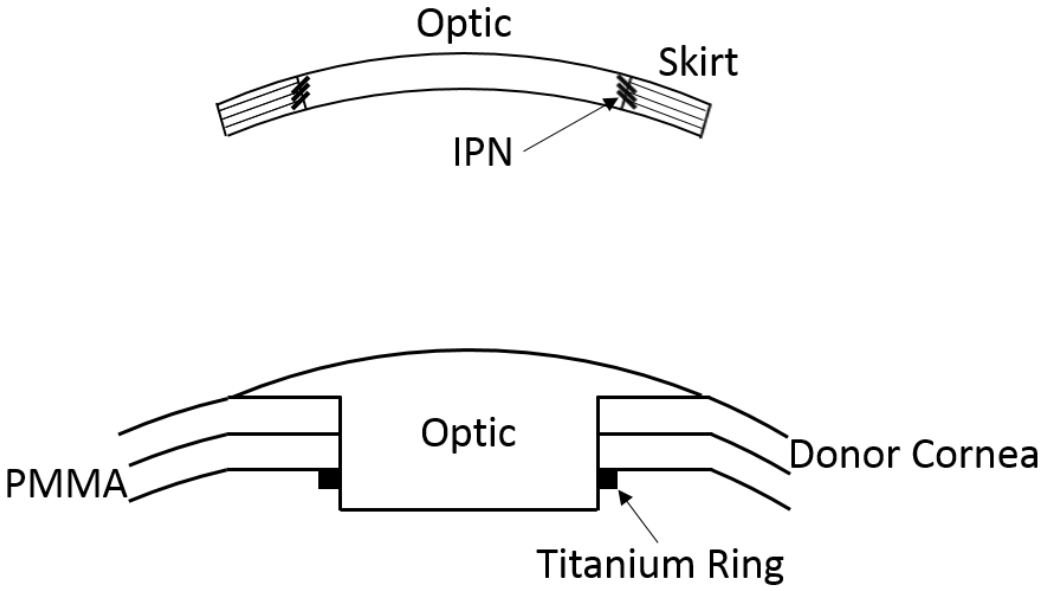

Figure 2.4: (top) Chirilia KPro devices[53] and (bottom) Boston KPro device[57]. Both types of devices utilize the common skirt-optic design.

The biggest problem associated with these synthetic devices is biointegration. The purpose of the skirt design is to provide an intermediate material that bonds the optic to the host tissue, but no synthetic material has shown consistent long-term biocompatibility. A KPro designed by Strampelli, which uses an extracted tooth from the patient as a skirt, has displayed the best long-term stability. However, it requires complex and tedious surgical procedures[58,59]. Recent efforts have focused on attaching biomolecules to synthetic materials to improve

biointegration[60,61]. Using natural materials (such as collagen) eliminates many of the complications that are associated with synthetic materials' poor long-term biocompatibility.

2.2.3 Tissue engineered corneas

Due to well-published complications associated with fully synthetic KPros, the research efforts towards producing an artificial cornea in recent years have taken a biomimetic approach. A variety of materials that act as a scaffold for cells and other molecules native to the cornea have been explored. Germain et al. were the first to engineer a collagenous matrix by culturing corneal epithelial cells and keratocytes[62]. The cultured cells synthesized a scaffold that mimicked the cornea's epithelial and stromal ultrastructure. However, these artificial corneas took weeks to months to form a bulk gel, and the bulk gel's mechanical properties were not quantified.

Frank and Griffith have made hydrogels that mimic both the mechanical and optical properties of the cornea while maintaining biocompatibility. Frank et al. have developed an interpenetrating network (IPN) of poly(acrylic acid) and poly(ethylene glycol) (PEG)[63,64], and Griffith et al. have developed implants with type III recombinant collagen[65]. Both groups have modulated specific properties by changing the synthesis conditions and concentrations of various cross-linking agents. Frank et al. have recently published a 6 month *in vivo* study of his IPN hydrogel implanted into a rabbit stromal pocket[49]. At the end of 6 months, the host material and implant appeared to be stable. Griffith et al. have reported a 4-year follow-up study of a human clinical trial[12]. After four years, the cross-linked collagen implants completely integrated with the host material. It is the first example of regeneration of epithelium, nerves, and stroma of an artificial cornea in a human. However, this was for partial thickness implants, which did not match the mechanical properties of the cornea and experienced significant thinning upon implantation.

2.3 Collagen

As described in Chapter 1, this investigation hypothesizes that the chemical and microstructural properties of silica-collagen composites can be tuned to yield favorable mechanical and degradation behavior for corneal replacement without reducing the optical properties of the gel. The following section will describe each component of the hybrid material and the manner in which interactions between those materials can be controlled and modulated.

2.3.1 Overview

Collagen is the most ubiquitous protein in the animal kingdom[66]. There is some form of collagen in every tissue of the human body with functions ranging from structural reinforcement in load bearing tissue to extracellular matrix for hosting tissue specific cells and macromolecules. There are over twenty different types of collagen which possess a triple helical section that is a right-handed super helix composed of three left-handed 'alpha' chains. The alpha chains can vary in amino acid sequence relative to the same triple helix, and can vary in length with respect to different types of collagen. However, every type of alpha chain has the same general amino acid repeat sequence of Glycine-X-Y, with glycine as the only amino acid that can occupy the central backbone position of the triple helix (X and Y are amino acids specific to the alpha chain type, and are commonly Proline and Hydroxyproline). There are 10 residues for 3 left-handed turns and 1 right-handed supercoil. This corresponds to an axial distance of 2.86 nm (0.286 nm per residue)[67–69].

The biosynthesis of collagen involves the synthesis of a larger precursor molecule called procollagen. Propeptide domains are enzymatically cleaved just prior to fibril formation. Telopeptides, also known as terminal sequences which are not triple helical and do not have glycine at every third residue, are short domains that are present at both ends of the collagenous

domain and are left behind after the cleavage of propeptide domains[66,70]. They are thought to be rich in lysine crosslinks and play an important role in directing fibril formation. These regions are also sensitive to proteolysis caused during chemical extraction and isolation of collagen molecules.

2.3.2 Type I collagen hydrogels

Amongst the variety of collagen types, type I collagen is a fibrillar-forming protein that makes up 90% of the collagen found in the human body[71]. The general methodology for forming collagen hydrogels requires an acidic solution of monomeric collagen that is extracted from animal tissue or recombinant collagen that can be synthesized from cells such as bacteria and yeast. If the pH and temperature of the acidic solution is raised, a fibril formation process is initiated and a collagen hydrogel is formed. This fibrillogenesis is an entropy driven process in which collagen molecules prefer collagen-collagen interactions over collagen-solvent interactions[72]. The fibrils' cylindrical structure possesses a circular cross-section, which results spontaneously as it minimizes the surface area of collagen exposed to the surrounding solvent. There have been many different theories proposed that explain this complex monomer-to-fibril transition. In general, the process consists of the formation, linear growth, and lateral growth of fibril sub units[73–82]. Hydrophobic and electrostatic interactions amongst amino acid side chains are thought to dominate the alignment of collagen molecules within subunits[79,83]. Further details of this process are outside the scope of this work. However, it is important to note that the size and arrangement of fibrils is dependent on parameters such as extraction method[75,84–89], ionic strength[76,90,91], temperature[75,76,82,90,91], concentration[82,92–94], and pH[76,91]. Additionally, the fibril formation process can be altered by the addition of other materials, such as sodium silicate[17], proteoglycans[95], synthetic polymers[96], and type V collagen[97]. As such, fibril formation conditions

can be modified to achieve collagen fibril networks of different stiffness, strength, and optical behavior.

2.4 Silica-collagen composites

2.4.1 Sol-gel method

Porous networks of amorphous silica can be prepared using the sol-gel process. Silica precursor molecules composed of a central silicon atom surrounded by ligands of various compositions are commercially available. When mixed with water, these molecules undergo a reversible hydrolysis reaction that replaces a ligand with a functional silanol (Si-OH) group (Figure 2.5). This reaction requires a water molecule and results in a ligand-based byproduct. A silanol group has the potential to take part in a reversible condensation reaction with either another silanol group or an unhydrolyzed ligand (Figure 2.6). The byproduct of each reaction is a water or an alcohol molecule respectively and results in a siloxane bond (Si-O-Si) in both cases.

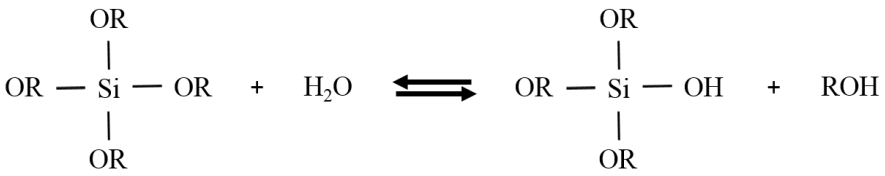

Figure 2.5: Hydrolysis reaction of tetrafunctional silica precursor molecule with R representing a ligand.

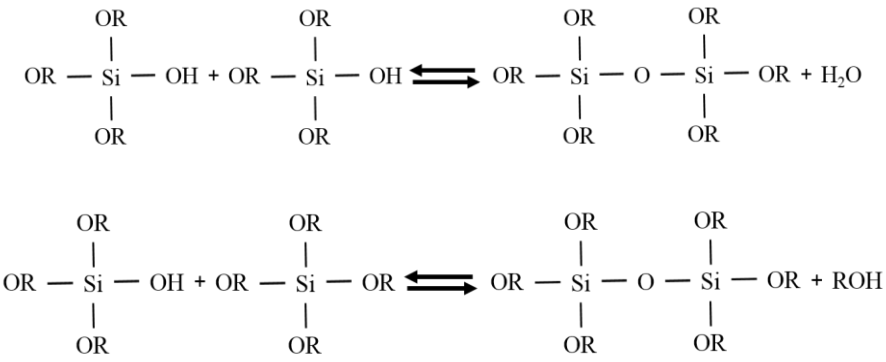

Figure 2.6: Condensation reactions of tetrafunctional silica precursor molecule.

The kinetics of hydrolysis and polymerization are dependent upon the precursor ligands, water content, temperature, pH, and the types of added solvents and catalysts[98]. Depending on the conditions of the reaction, silica networks of varying meso-structures can be formed, such as stable sols of highly condensed spheres, or gels consisting of a branched siloxane bond network.

2.4.2 Silica-collagen composites

The sol-gel method described above allows for silica networks to be formed at low temperatures, which advantageously allows for collagen to be present without denaturing. Additionally, the sol-gel processing conditions can be adjusted to modulate physical, mechanical, and biodegradation behavior. By performing this sol-gel method in the presence of collagen, the mechanical properties of collagen hydrogels can be enhanced, and their biodegradation rate can be modulated.

Ono et al. were the first to report a silica-collagen hybrid material using a co-polymerization process with tetraethyl orthosilicate (TEOS)[21]. Coradin et al. used a similar process with waterglass to observe the effects of silica precursors on collagen fibril formation[15]. The same group showed freeze-dried silica-collagen-hydroxyapatite gels have favorable properties for bone replacement. The gels possessed high compressive strength and allowed for

attachment, proliferation, and osteogenic differentiation of bone marrow stromal cells[99]. From these studies and other *in vitro* experiments, silica has been shown to degrade in physiological conditions at rates dependent upon the synthesis conditions and chemical properties of the gel[23–27,29]. The degradation rate can be significantly reduced by increasing the degree of condensation through aging with appropriate pH and temperature conditions[23,25].

Therefore, a sol-gel process can be modified to fine-tune collagen hydrogel structures from the molecular level up to the bulk scale. By using dilute concentrations of silica precursors, collagen fibrils can be uniformly coated with silica layers that are nanometers in thickness. This will allow for the silica to act as a physical barrier to enzymes which degrade collagen, while improving the stiffness and strength of the gel itself. Most importantly, the nano-scale control of silica coatings will minimize the light scattering contributions of the silica network. In addition to the physical and geometrical properties of silica formed, there is a vast collection of silane molecules commercially available that can be incorporated into the silica synthesis to vary the chemical composition of the silica network. This secondary chemical modification will add additional flexibility to the control of the gel's mechanical properties, degradation, or any other tunable property. For instance, PEG-silanes have been used to passivate silica surfaces, and mPEG(PEG with methyl terminal)-silanes have been used to make a silica particles more hydrophobic[100–102].

Chapter 3

Materials and Methods

3.1 Materials

Table 3.1 lists all of the materials mentioned in the following methods section, along with associated abbreviations and manufacturer information.

Table 3.1: Materials used with associated details and abbreviations.

Material	Details	Abbreviation	Man./Supplier
Polyethylene glycol	35 kDa	PEG	Sigma Aldrich, St. Louis, MO
Cellulose dialysis membrane	12 kDa	-	Sigma Aldrich, St. Louis, MO
Soluble type I collagen	Rat tail tendon, 5 mg/mL	-	Alphabioregen, Worcester, MA
Soluble type I collagen	Bovine skin	-	Organogenesis, Canton, MA
Ammonium hydroxide	28-30% (w/w)	-	Sigma Aldrich, St. Louis, MO
Sodium phosphate dibasic	-	-	Sigma Aldrich, St. Louis, MO
Monopotassium phosphate	ACS grade, 99%	-	Sigma Aldrich, St. Louis, MO
Microcrystalline cellulose	ACS grade, 20 µm	MCC	Sigma Aldrich, St. Louis, MO
Methyl cellulose	ACS grade	-	Sigma Aldrich, St. Louis
NH_2-PEG-COOH	1 kDa	-	Creative PEGWorks, Chapel Hill, NC
N,N'-Carbonyldiimidazole	Reagent grade	CDI	Sigma Aldrich, St. Louis, MO
3-aminopropyltriethoxsilane	99%	APTES	Sigma Aldrich, St. Louis, MO
Phosphate buffered saline	Tablet	PBS	Sigma Aldrich, St. Louis, MO
Poly-L-lysine	1-5 kDa	PLL	Sigma Aldrich, St. Louis, MO
Tetraethyl orthosilicate	Reagent grade, 98%	TEOS	Sigma Aldrich, St. Louis, MO
Ludox SM	30% (w/w)	-	Sigma Aldrich, St. Louis, MO
Human foreskin fibroblasts	-	HFF	ATCC, Manassas, VA

Dulbecco's Modified Eagle's Medium	Cell culture medium	DMEM	Gibco, Carlsbad, CA
Calcein AM	Live cell fluorescent stain	-	Life Technologies, Carlsbad, CA
Propidium iodide	Dead cell fluorescent stain	PI	Sigma Aldrich, St. Louis, MO
DMEM/Ham's F-12 with 20 mM L-Glutamine	Cell culture medium	-	Sigma Aldrich, St. Louis, MO
Antibiotic/Antimycotic Suspension	Pencillin G 100 units/mL, streptomycin 100 μg/mL, amphotericin B 0.25 μg/mL	-	Sigma Aldrich, St. Louis, MO
Insulin-Transferrin-Selenium	-	-	Gibco, Carlsbad, CA
Collagen IV	-	-	Abcam, Cambridge, MA
Keratin AE1/AE3	-	-	Millipore, Billerica, MA
Alexa Fluor 546	Secondary antibody	-	Invitrogen, Molecular Probes, Eugene, OR
488 Goat anti-Rabbit IgG (H+L)	Secondary antibody	-	Invitrogen, Molecular Probes, Eugene, OR
Vectashield/DAPI	-	-	Vector Laboratories, Burlingame, CA
Glutaraldehyde	25%, in water	-	Sigma Aldrich, St. Louis, MO
Sucrose	-	-	EMD Millipore, Billerica, MA
Sodium cacodylate trihydrate	-	-	EMS, Hatfield, PA
10-0 nylon suture	-	-	Ethicon, Blue Ash, OH
Polybed 812	resin kit	-	Polysciences, Inc., Warrington, PA
Osmium tetroxide	4%, in water	-	Sigma Aldrich, St. Louis, MO
Collagenase	Type I from clostridium hystolyticum	-	Sigma Aldrich, St. Louis. MO
Trypsin-EDTA	0.25%	-	Gibco, Carlsbad, CA
Formaldehyde	35%, in H_2O	-	Sigma Aldrich, St. Louis, MO
Fetal bovine serum	10%	FBS	Gibco, Carlsbad, CA
Penicillin-Streptomycin	10,000 U/mL	-	Gibco, Carlsbad, CA
ActinGreen 488 ReadyProbes	-	-	Life Technologies, Carlsbad, CA
Hoechst 33342 blue nuclear stain	-	-	Life Technologies, Carlsbad, CA

3.2 Manufacture of a collagen hydrogel

For every section presented, collagen hydrogels were solidified using one of two different neutralization methods: ammonia vapor exposure or buffer neutralization.

The stock collagen solution used was soluble type I collagen from rat tail tendon, and was dissolved in HCl (pH 3, 5 mg/mL). In most cases, dialysis against PEG was used to increase the concentration of the stock soluble collagen solution. Briefly, a cellulose dialysis membrane was soaked in deionized (DI) water, and collagen was poured into one end of the tubing while the opposing end was clamped shut by a dialysis clip. The open end was sealed with another dialysis clip. The dialysis bag containing collagen was then dialyzed against a 0.1 g/mL PEG solution at 4 °C until target concentrations as high as 150 mg/mL were reached. The collagen mass was assumed to remain constant throughout, and the collagen concentration was estimated by the final volume of the solution. Post concentration, the collagen solution was put into specific molds dependent on the characterization to be performed. The most common geometry used was a disk with 500 μm thickness, but samples as thin as 200 μm were possible to produce.

In the ammonia vapor method of gelation, collagen filled molds were placed in a sealed chamber alongside an opened container containing 1 mL of ammonium hydroxide. The samples were exposed to ammonia vapor for 10 min at room temperature. After gelation, the samples were rinsed with DI water.

Gels were also obtained by neutralizing with a buffer. For a 5 mg/mL collagen concentration, 1 mL of collagen solution was dialyzed against 20 mL of buffer solution at 4 °C for 24 h. The buffer solution was a 19:1 (v:v) mixture of 0.2 M sodium phosphate dibasic and 0.2 M monopotassium phosphate, respectively. The solution was then incubated at 37 °C for 1 h to allow gelation to occur. For higher concentrations of collagen, premature fibril formation occurs during buffer dialysis at 4 °C. Therefore, the higher concentrated collagen solutions were heated to 37 °C and put into the desired mold prior to neutralization. Then, a preheated bag filled with buffer solution was placed in contact with the top surface of the collagen solution for 1 h.

3.3 Nanocrystalline cellulose-collagen hydrogel method

Chapter 6 describes the results of studies using nanocrystalline cellulose (NCC) to induce collagen fibril alignment during collagen fibrillogenesis. NCC was prepared by sonicating 20 g of MCC in 500 mL of water with a Cole-Parmer 750 W ultrasonicator. The ultrasonicator was pulsed on for 2 s every 6 s for a total of 36 h (12 h total sonication time) at 38% amplitude. The resulting thick, milky-white suspension of NCC was added to concentrated collagen in a petri dish and then manually stirred until visibly homogenous. The relative NCC loadings in weight percent reported for the samples refer to solid NCC to solid collagen, not considering the water content. The ammonia vapor neutralization previously described in section 3.2 was used to form NCC-COL hydrogels.

The same methodology was used to make methylcellulose-collagen hydrogels with slight modification to the procedure above. Before sonication, 20 g of methylcellulose powder was dissolved in 500 mL water at 70 °C, and then cooled. This resulted in a viscous, slightly hazy suspension, which was sonicated according to the procedure detailed above. After sonication, the material was added to the appropriate amount of concentrated collagen and gelled following a procedure identical to the procedure for NCC-COL hydrogels.

3.4 Nanowire-collagen hydrogel method

In Chapter 5, magnetic nanowires were used to induce fibril alignment during collagen fibrillogenesis. An electrodeposition method was used to make Ni wires 6 μm in length and either 35 or 100 nm in diameter. A detailed methodology for this process can be found in the paper published by Sharma et al.[103]. The nanowires initially suspended in ethanol were rinsed with DI water 3 times by collecting the nanowires on the vial wall with a magnetic stand and aspirating the solvent. The nanowires were then soaked in an NH_2-PEG-COOH solution (0.2

mass %, pH 7) at a concentration in the range of 10-100 million wires per mL. The nanowires were ultrasonicated (sweep-frequency) for 10 minutes and incubated at 4 °C overnight. The sample was aspirated of PEG solution and rinsed with DI water. The nanowires were then soaked in a CDI solution (0.2 M, in 1 mM HCl) at the same nanowire concentration that was used with the PEG solution. The sample was sonicated for 10 min and incubated at room temperature overnight. The CDI solution was replaced with an equal volume of soluble collagen solution and pipette-mixed until the nanowires were uniformly suspended, and was then incubated at room temperature overnight.

The collagen-nanowire solution was pipette-mixed and placed in a rubber mold. The sample was placed in the center of a SuperMACS magnetic separator (Miltenyi Biotec, Bergisch Gladbach, Germany) for two minutes to allow for nanowire alignment. Under the same magnetic field, collagen fibril formation was induced by ammonia vapor neutralization using a 30 µL drop of ammonium hydroxide placed next to the sample. The vapors from the ammonia were trapped next to the sample using a petri dish cover. After 10 min of ammonia exposure, the hydrogel was rinsed with DI water.

3.5 Silica-collagen copolymerization

In chapter 7, results of silica-collagen composite material characterization are presented. Silica-collagen composite materials were made using a copolymerization process (Figure 3.1) by mixing type I collagen with APTES. APTES was mixed with acetic acid in a bath sonicator at 4°C. The molarity of the acetic acid was varied to adjust the pH of the hybrids. Soluble type I bovine collagen was mixed with the diluted APTES at a 10:3 volume ratio for 10 minutes with a magnetic stir bar. To prevent premature gelation, the mixing vial was submerged in an ice bath. The ratios describing the hybrid composition are silica to collagen weight ratios. The two

compositions investigated in the study described in Chapter 7 were 3:1 and 9:1. The silica to collagen ratio was modulated with the volume of acetic acid used in the APTES dilution.

Immediately after mixing, the gels were de-aerated by centrifugation and poured into rubber molds. For manufacturing of the *ex vivo* implants, the gel was allowed to cure in a hemispherical mold, with curvature similar to that of the native cornea, and after gelation were punched with a corneal trephine to an 8.2 mm diameter. Conventional methods of hybrid manufacturing involve formation of the hybrid under fully hydrated conditions (100% relative humidity). In addition to conventional manufacturing, studies were performed on hybrids that were dehydrated (cured at 72% relative humidity for 24 h) which are described as 'xerogels'. After complete formation and dehydration of the material, the xerogel samples were rehydrated in PBS. The rehydrated samples were kept in 100% relative humidity conditions prior to testing. Because all xerogels were rehydrated prior to testing, rehydrated xerogels will be referred to as simply xerogels.

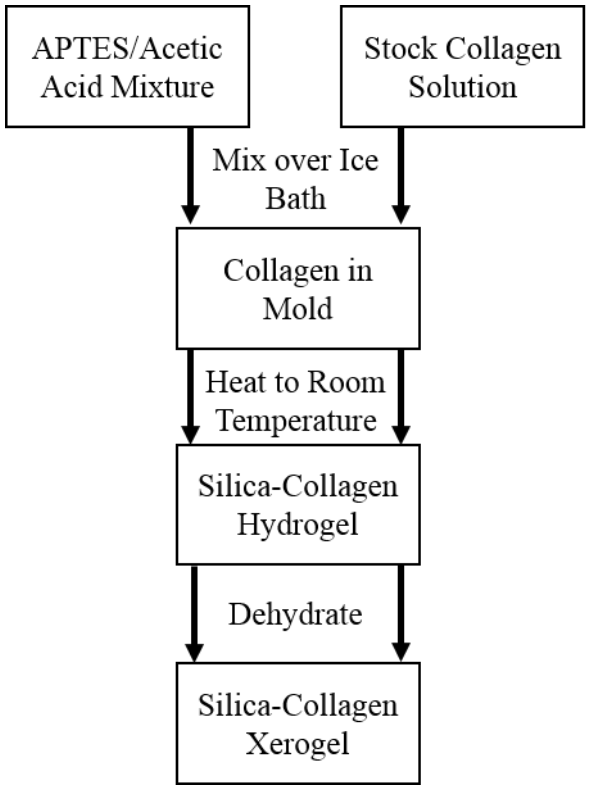

Figure 3.1: Copolymerization process for fabricating silica-collagen composites

3.6 Silica-collagen two-step coating process

Characterization results of silica coated collagen fibril networks described here are presented in chapter 8 (Figure 3.2). First, a collagen hydrogel (fabricated using the methods described in section 3.2) was soaked in a 10µg/mL PLL solution for 1 hour at room temperature., Next, solvent exchange was performed prior to soaking PLL-treated collagen hydrogels in a Stöber solution. Hydrogels were sequentially soaked in 20%, 40%, 60%, and 80% ethanol baths for 10 min each. These samples were then placed in an ethanol/water/TEOS/ammonium hydroxide solution. Silica precursor solutions for single hydrogel discs (5 mm diameter)

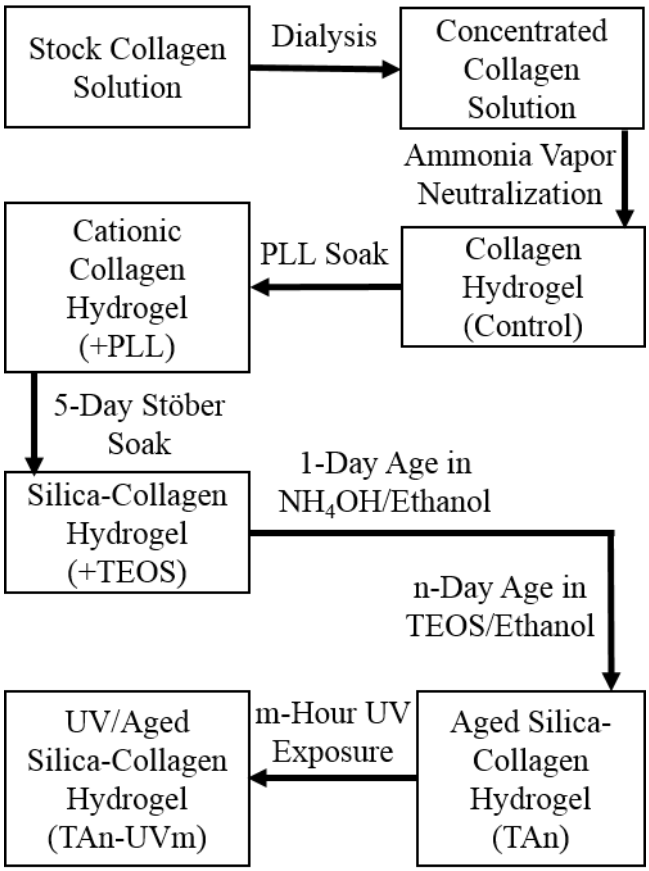

Figure 3.2: General two step-procedure for making silica-collagen composite.

were prepared in the following manner. TEOS, pure ethanol, and DI water were mixed vigorously. This Stöber solution had an H_2O:Si molar ratio (R) of 40,000 and a 4:1 ethanol:H_2O volumetric ratio. This R-value was used for all gels unless stated otherwise. Ammonium hydroxide was added dropwise until the pH of the solution was approximately 9. The PLL-treated hydrogel was then placed in the Stöber solution and gently agitated. After 24 h of soaking, the Stöber solution was replaced with a fresh solution. For some 5 mg/mL hydrogels, a one-hour soak in a stable Ludox SM silica sphere suspension (3% w/w) was performed between the PLL treatment and Stöber soaking steps.

Aging methods were used to maximize the condensation of silica networks formed during deposition. The methods used were similar to those used by Hæreid et al.[104] for TEOS alcogels.

Briefly, after silica deposition, each sample was put in a solution consisting of 1 mL of 80% ethanol and 30 µL of ammonium hydroxide for 24 h. These samples were then incubated in a TEOS/ethanol solution (7:3 volume ratio) for different periods of time. In an attempt to densify this network and maximize condensation of the deposited silica, the aged gels were exposed to ultraviolet radiation (UV) by placing hydrated gels in the center of a sterile laminar flow hood with a 39 W UV light source. The effects from time of UV exposure were examined.

3.7 Chemical characterization

Fourier transform infrared spectroscopy (FTIR) and Raman spectroscopy were used to characterize the chemical bonds present in silica-collagen and NCC-collagen composites. FTIR was performed with a Nicolet Magna-IR 760 spectrometer from 4000 to 800 cm^{-1} with a resolution of 2 cm^{-1}. Samples were ground with KBr powder and pressed into pellets for FTIR analysis. In some cases, Raman spectroscopy was performed. Raman samples were critical-point dried, and spectra of the samples was collected with a Witec (Ulm, Germany) alpha300 R confocal Raman microscope equipped with a UHTS spectrometer and DV401 CCD detector. A 10 mW Nd:YAG laser was used as an excitation source and was focused on the sample with a Nikon 10x air objective (Melville, NY). Spectra collection consisted of 20 accumulations each with a 30 second integration time. The spectra was collected and processed using the Witec control software.

3.8 Mechanical testing

All mechanical tests were performed using a low force Intron tensile tester (Norwood, MA). Two types of tests were performed to quantify the mechanical behavior of various materials: uniaxial tensile testing and suture pullout testing.

Samples were formed in dogbone shaped molds or cut into rectangular strips for uniaxial tensile testing. A PBS bath was used to maintain sample hydration for the duration of the experiments. The sample ends were loaded into two opposing grips with a constant gauge length of 3 mm. The specimens were preconditioned with ten cycles of a sinusoidal strain (amplitude = 5% strain, wavelength = 4 s). Following preconditioning, the strain was ramped at rates of 1% per second to 8, 18, and 30%, respectively (Figure 3.3). At each step strain, the material was allowed to relax for 3 min. The stresses after three minutes of relaxation were plotted versus strain, and the slope of this curve was defined as the relaxed modulus of the material. In some cases, a simple ramp to failure protocol was used to quantify and compare stiffness values in a timely manner.

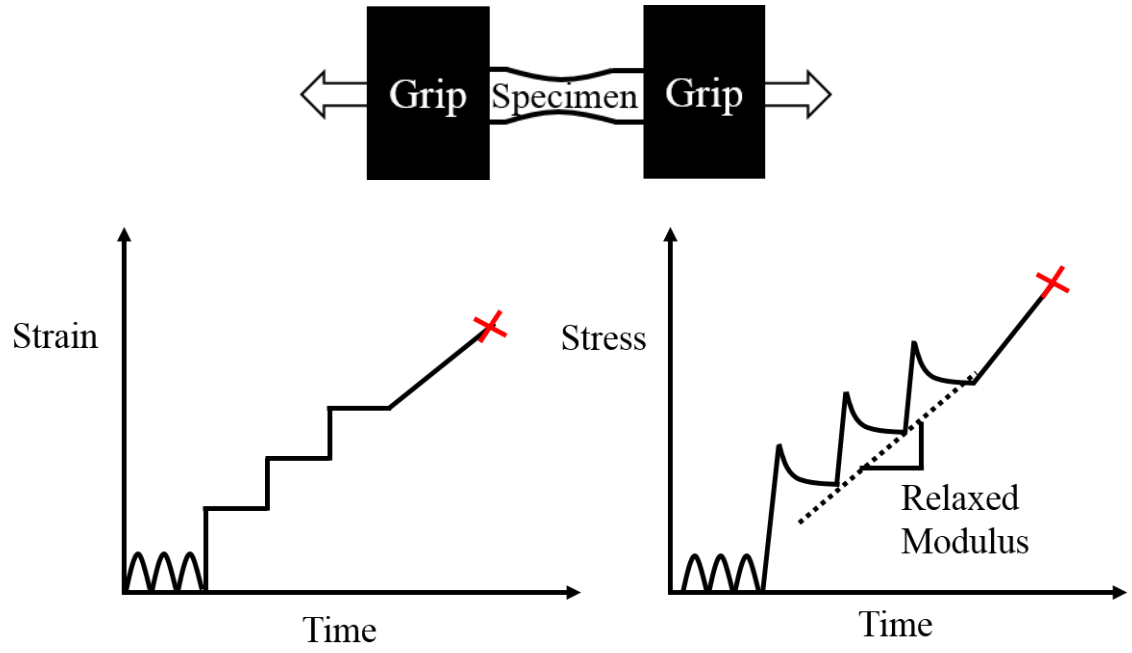

Figure 3.3: (Top) Top view of a typical dog-bone specimen loaded into grips. (Bottom Left) An example of a strain protocol consisting of preconditioning, step-strain holds, and ramp to failure. (Bottom Right) An example of the stress response for a viscoelastic sample illustrates how relaxed modulus is defined and calculated.

Chapter 7 describes the results of hybrid material suture pullout tests, which were performed as follows. An 8 mm-diameter corneal trephine was used to punch out disc-shaped test implants, which were approximately 200 µm thick. One half of each disc was clamped in a spring-loaded grip. A 10-0 nylon suture was placed 2 mm from the edge of the opposite half of the implant, and the two free ends of the suture were placed in the other grip (Figure 3.4). All implants were tested in a PBS bath to prevent dehydration. The grip holding the suture was displaced at a rate of 0.1 mm/s relative to the opposing grip until the suture was pulled completely

through the implant. The failure point was considered to be the first showing of ripping or tearing. Rupture strength was defined as the force at failure divided by the thickness of the disc.

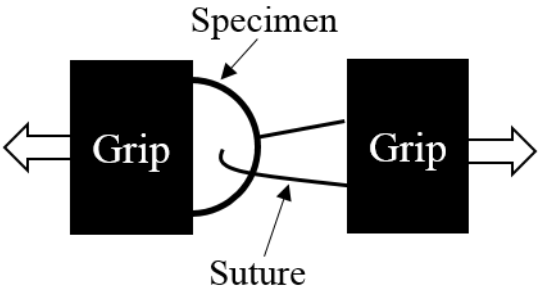

Figure 3.4: Top view of the suture pullout setup.

3.9 Optical characterization

UV/Vis transmittance

The transmittance *T*, defined as the ratio of transmitted light intensity to incident light intensity, of composites was measured at room temperature in either a 96 well plate or a cuvette using a spectrophotometer (SpectraMax Plus, Molecular Devices; Sunnyvale, CA). All samples were measured while hydrated with PBS, and blank data was collected for wells/cuvettes containing the same volume of PBS used with samples. The fraction of transmittance (ratio of the amount of light that passed through the sample to the amount of light that passed through the blank) was calculated for wavelengths of 300 to 800 nm. Most samples were 500 μm in thickness to make direct comparisons with the native cornea. For samples with a thickness *d*, a material constant α_c was calculated from Equation 3.1.

$$\log T^{-1} = \alpha_c d \qquad \text{(Eq. 3.1)}$$

The material constant is an intrinsic material property. If the sample thickness varied from 500 μm, the calculated α_c could be used to estimate the transmittance of the same material with a 500 μm.

Refractometry

Refractive indices of materials were measured at room temperature with an Abbe refractometer (Zeiss, Oberkochen, Germany). Samples were individually immersed in saturated sucrose solutions. Solutions that contained a sample were diluted dropwise with DI water until the sample became more transparent. An aliquot of the sucrose solution was removed and its refractive index was measured. After this first measurement, the solution was again diluted with a few drops of DI water, and the refractive index was re-measured. Changes in refractive index between dilutions were approximately 0.004. This procedure was repeated until each sample became more opaque, and the refractive indices of these endpoint solutions were recorded.

Polarized light transmittance

Chapter 5 describes results of polarized light transmittance testing (measured with respect to polarization angle) used to characterize the alignment of collagen fibrils of synthetic matrices. Briefly, a 633 nm wavelength HeNe excitation laser emitted incident light normal to the top surface of a synthetic matrix. Prior to incidence on the top surface, the beam travelled through a linear polarizer, rotating the beam through 360^0. An optical chopper set to a frequency of 380 Hz was used in conjunction with a lock-in amplifier set to the same frequency and a detector to sense the transmitted polarized beam. A Labview (National Instruments, Austin, TX) interface was used to control the polarization angle and collect real-time data.

3.10 *In vitro* Biocompatibility

HFF biocompatibility test

The ability of HFFs to attach to the surface was tested as one measure of biocompatibility. HFFs were cultured normally at 37 °C, 70% relative humidity, and 5% CO_2. At 80% confluence, cells were detached from their culture flasks by addition of 3 mL of trypsin, followed by quenching with 5 mL of media after 3 minutes. The suspended cells were pelleted by centrifugation in a 15 mL centrifuge tube for 10 min at 1000 rpm. The supernatant was removed and cells were resuspended in 3 mL of DMEM. Cells were loaded into a hemocytometer and counted using a Nikon TMS bright-field microscope (Tokyo, Japan). Based on the initial cell concentration, DMEM was added to the suspension to adjust the final cell concentration to 10^5 cells/mL. Unless stated otherwise, hydrogels were prepared in a six well plate, rinsed with PBS, and 2 mL of DMEM cell solution was pipetted into each well over the prepared hydrogels. The well plate was covered and incubated for 1 h in a Forma Steri Cult CO_2 incubator (Thermo Fisher, Waltham, MA) at 37 °C, 70% relative humidity, and 5% CO_2.

The viability of the cells was assessed at three different time points after cell seeding (1h, 24h and 72 h). A solution of Calcein AM (2 mM) and PI (0.5mg/mL) diluted in PBS was used to stain live cells and dead cells respectively. For each given time point, the supernatant DMEM was aspirated, and 2 mL of calcein AM/PI solution was added to each well. The sample was incubated for 20 min. Live cell images were taken on a Zeiss Axioskop light microscope with a fluorescein isothiocyanate (FITC) filter (Zeiss 10, 450–490 nm excitation, 515–565 nm emission). Dead cell images were taken on the same microscope using a tetramethyl rhodamine isothiocyanate (TRITC) filter (Zeiss 20, 530–560 nm excitation, 590–650 nm emission).

Arachnoid cell contact alignment studies

Immortalized arachnoid cells isolated from rat arachnoid meninges were derived and cultured as described previously.[105]. The arachnoid cells were cultured in 6 well plates using arachnoid media composed of DMEM, 10% FBS, and 2% Penicillin-Streptomycin. The cells were grown to 80-90% confluence, washed with 2mL of PBS and released from the surface using 1mL of 0.25% Trypsin-EDTA for 1 min. The trypsin reaction was quenched with 1 mL of arachnoid media and the cell suspension was transferred to a centrifuge tube and pelleted at 1000 rpm for 10 min. The supernatant was aspirated and the cells were re-suspended in 4 mL of arachnoid media, and 1mL of this cell suspension was added to each well containing collagen gels. Collagen gel preparation was described previously and gels were washed 3x with PBS before cell seeding, then covered in 1 mL of prewarmed media to promote protein deposition on the collagen surfaces before cells were added. The total volume in each well was 2 mL and promoted cell seeding at approximately 20% confluence (~150,000 cells/well = ~ 16,000 cells/cm^2). After 72 h, cell seeded collagen gels were processed using the fixing and staining procedures described below.

Cell seeded samples were washed twice with PBS and fixed for 10 min at room temperature with a 3.7% formaldehyde solution diluted in PBS. Next, samples were washed twice with PBS and soaked in a 0.1% Triton x-100 solution for 5 min. The samples were subsequently washed and soaked in a methanolic solution (2.5% in PBS). Finally, samples were stained with ActinGreen 488 ReadyProbes reagent and Hoechst 33342 blue nuclear stain using established protocols available on the Invitrogen product website. Nikon biostation IM phase contrast and fluorescence microscopy were used to image the cells and synthetic matrix. Images were acquired using a high sensitivity monochrome CCD detector.

3.11 *Ex vivo* biocompatibility

Preliminary biocompatibility of corneal re-epithelialization of copolymerized composites was studied in a rabbit cornea organ culture model using methods similar to those described by Evans et al[106]. Dr. Sanjay Patel at the Mayo Clinic in Rochester, MN performed all of the ex-vivo biocompatibility experiments described below. Five New Zealand white rabbits were euthanized with an overdose of intravenous sodium pentobarbital immediately before operating on both corneas. All the procedures involving these animals adhered to the ARVO Statement for Use of Animals in Ophthalmic and Vision Research and were approved by the Mayo Clinic Institutional Animal Use and Care Committee. Under sterile conditions, the center of the cornea was marked and the anterior stroma was incised with a guarded diamond blade to a depth of 200 μm. A 9 mm-diameter circular lamellar pocket was created at a depth of 200 μm from the anterior surface. The anterior lamella was excised centrally to create a keratectomy approximately 5 mm in diameter.

After surgical preparation of the cornea for implantation, the eye was enucleated and the anterior segment was excised, including removal of the lens and iris. The anterior segment had an approximately 3 mm rim of sclera and was mounted to a modified Petri dish designed for rabbit anterior segment organ culture. The corneoscleral rim was clamped with a locking ring and culture medium was infused to fill and maintain the anterior chamber. The culture medium used was DMEM/Ham's F-12 with 20 mM L-Glutamine with a 1:100 dilution of Antibiotic/Antimycotic Suspension and a 1:100 dilution of Insulin-Transferrin-Selenium. A sterile film of the hybrid was punched with a corneal trephine to create an 8.2 mm button. The button was then implanted into 8 corneas with the periphery of the implant enveloped in the lamellar pocket and the center of the implant exposed due to the previous keratectomy. The dimensions of the keratectomy, i.e., the de-epithelialized region over the implant, were measured

by staining the region with sodium fluorescein and examining with a blue light. Culture medium was added externally until it just covered the center of the cornea and implant.

Two control eyes received an identical surgical procedure without implantation of a bio-hybrid. In all cases, the epithelial defect was measured daily until closure, and time to closure was recorded. Culture medium was changed daily. Anterior segments were incubated for 7-18 days at 37 °C in humidified air containing 5% CO_2, after which the corneoscleral rims were fixed in 4% paraformaldehyde for examination by light and fluorescence microscopy. The fixed tissue was embedded in paraffin, cut into 4 µm-thick sections, and stained with hematoxylin and eosin or de-parrafinized and rehydrated for immunostaining with antigen retrieval. Sections were incubated overnight at room temperature with collagen IV 1:500 or with keratin AE1/AE3, 1:250. After washing, sections were incubated at room temperature with secondary antibodies (Alexa Fluor 546 or 488 Goat anti-Rabbit IgG (H+L)) for 45 minutes, then washed and stained with Vectashield/DAPI prior to examination. Positive and negative controls were stained at the same time as experimental tissue.

3.12 Biodegradation assay

The resistance of a material to enzymatic degradation was quantified using an *in vitro* assay with bacteria-derived collagenase. An enzyme solution was prepared by dissolving lyophilized collagenase in PBS at a concentration of 10 U/mL. The solution was preheated to 37 °C in a petri dish. For every sample (0.5 mm thick, 20 mm^2 area), 0.5 mL of enzyme solution was added. The samples were incubated at 37 °C, and the weight of each sample was measured hourly until samples became too weak to handle.

3.13 Scanning electron microscopy (SEM)

Hydrogel samples were fixed according to standard methods. Briefly, samples were soaked in a 2% glutaraldehyde solution containing 0.1 M sucrose and 0.1 M sodium cacodylate for 1 h at room temperature. The samples were then post fixed in a 1% osmium tetroxide solution for 30 min, after which they were sequentially soaked in 20%, 40%, 60%, 80%, 95%, and 100% ethanol solutions for 10 min each. Samples were critical-point dried (CPD) with a Tousimis samdri-780A CO_2 critical point dryer (Tousimis, Rockville, MD), attached to SEM stubs with carbon tape, and coated with 5 nm of Pt. Images were obtained using a JEOL 6500 SEM (JEOL USA, Peabody, MA) with a 5 kV beam.

3.14 Transmission electron microscopy (TEM)

TEM samples were prepared using the same methodology as SEM preparation. After the sample solvent was replaced with ethanol, samples were soaked in ethanol/resin solutions with volume ratios of 2:1, 1:1, and 1:2 for one hour each. Samples were soaked in pure resin for one hour, and then in a fresh resin solution overnight. Samples were placed in TEM stub molds with fresh resin and cured at 60 °C for 48 h. Samples were then sectioned and stained according to standard procedures at the University of Minnesota Imaging Center. TEM images were obtained using a CM12 transmission electron microscope (Phillips, Amsterdam, Netherlands) by Gail Celio.

3.15 Rayleigh scattering model

The Lord Rayleigh light scattering model (derived for small cylinders with infinite lengths relative to the incident light wavelength) was applied to predict the optical behavior of the collagen hydrogels described in these studies. Benedek used the same model when discussing

optical theories to explain the transparency of the cornea[107]. Using these calculations, the amount of light scattered for gels with a given fibril diameter and position distribution were estimated, and theoretical trends found were compared to the experimental results obtained from electron micrographs and light transmittance data.

3.16 Statistical analysis

In order to quantify the statistical significance of the data reported, all nominal values were reported with a confidence limit, which is defined as the uncertainty associated with an estimated mean. The following formula was used to calculate the confidence limit of the mean for a given sample,

$$Confidence\ Limit = mean\ value \pm \frac{t_{\vartheta,\alpha} * s}{\sqrt{N}} \qquad \text{(Eq. 3.2)}$$

where t is the two-sided t-distribution value for a given degrees of freedom ν and confidence coefficient α, and s is the standard deviation of the sample. A confidence coefficient of 95% was used when calculating the confidence limit. If the confidence limit of one sample did not overlap the confidence limit of another sample, the difference in mean values of these two samples was deemed statistically significant.

Chapter 4

Optical behavior of collagen hydrogels

4.1 Introduction

As mentioned in Chapter 2, the cornea is estimated to refract 70% of the light that reaches the retina[30]. Additionally, the tissue must act as a low pass filter, allowing visible light to pass through while impeding the transmittance of harmful ultraviolet frequencies that cause damage to internal parts of the eye. This wavelength-dependent transmittance is shown in Figure 2.1. There have been many theories proposed to explain the manner by which collagen (which is present in most connective tissues in the body) and other components of the cornea are transparent in the visible light spectrum. Prior to the development of the electron microscope, it was believed that all of the components that make up the cornea were similar in refractive index, explaining the limited degree of light scattering[108]. However, while the exact difference between the refractive indices' of collagen fibrils and the ground substance of the cornea is still a topic of debate, a significant difference in refractive index between these two components exists[109].

More notable theories were developed once the cornea's unique ultrastructural properties were discovered. Maurice suggested crystalline packing of the cornea consisting of uniform spacing and monodisperse fibril diameters was necessary to achieve minimal scattering due to destructive interference of the summed scattering field[109]. Hart and Farrell disputed this claim by showing that the corneal structure was quasi-regular, and demonstrating that crystallinity is not required for transparency using numerical scattering solutions[110]. Benedek and Goldman made similar observations noting the amorphous structure of the shark's Bowman's layer, which takes up 15% of the cornea's thickness, but is still transparent[111].

Benedek, using a scattering model similar to Maurice's, was able to mathematically prove the dependence of transparency on the spatial density distribution within the cornea[107]. More specifically, he suggested that the opacity from corneal swelling was due to fluctuations in the indices of refraction for wavelengths larger than one half the wavelength of incident light (i.e. void spaces with absent fibrils termed 'lakes'). By adopting a direct-summation method similar to the method used by Benedek, as well as Freund et al.[112] for corneal optical theory, trends in the optical behavior of collagen hydrogels can be observed. This direct-summation is used in the Rayleigh scattering model, based off of Rayleigh's solution for scattering of light from aligned cylinders of infinite length. The model considers the refractive index of the fibrillar component and surrounding medium, as well as fibril position, diameter, and incident wavelength.

A great amount of previous research has been dedicated to characterizing the microstructural, optical, and mechanical behavior of collagen hydrogels. However, there has been a limited amount of work that reports the microstructural differences between collagen hydrogels made using a buffer neutralization, and those made from ammonia vapor exposure. In this chapter, collagen hydrogels of varying concentrations were made using both methodologies. Their microstructural properties were characterized using SEM and TEM, and their light transmittance over the UV and visible spectrum was measured. From these experimental results and the simulation results obtained from the Rayleigh scattering model mentioned above, conclusions were made about which microstructural features are the most significant in controlling the optical behavior of collagen hydrogels.

4.2 Methods

Collagen hydrogels were made according to the procedures detailed in sect. 3.1. Ammonia vapor and buffer dialysis neutralizations were used on collagen solutions with concentrations of 5, 50, and 100 mg/mL. The spectral transmittance of these gels was measured

with a spectrophotometer (sect. 3.9) and compared with the microstructural features found in SEM (sect. 3.13) and TEM images (sect. 3.14). SEM and TEM images were used to estimate fibril diameters by manual image analysis in ImageJ. Inverted TEM images were further evaluated by performing line scans to illustrate the spatial fluctuations of density in the materials.

The Rayleigh scattering model briefly described in section 3.15 was used to estimate the transmittance of fibril arrays. Two main simulations were performed: relative transmittance (compared to the human cornea) for a comprehensive fibril diameter-fibril spacing parametric space, and relative transmittance for different arrangements of fibril bundling. The diameter/spacing simulations established a region in the previously mentioned two-dimensional design space that matched corneal transmittance across the UV/VIS light spectrum. The bundling simulations held fibril density and size constant, but the positions of fibrils varied from randomly dispersed to fibril bundles reaching micrometers in size.

4.3 Results

4.3.1 SEM/TEM microstructural analysis

The first phase of this investigation involved characterizing the influence of microstructure on the macroscopic optical properties of collagen hydrogels. Electron micrographs showed that all collagen hydrogels were composed of an amorphous network of interconnected fibrils. SEM images showed that ammonia vapor neutralization produced collagen fibrils with relatively uniform spacing, and showed that average fibril diameter was related inversely to collagen concentration. For samples that underwent buffer neutralization, SEM images showed micron sized fibril bundles in the 5 mg/mL gel. However, the 50 and 100 mg/mL gels had average fibril diameters of approximately 30 nm.

For ammonia vapor neutralization, TEM images had good agreement with SEM images for the 5 and 50 mg/mL concentrations. However, TEM images of 100 mg/mL gels, which had fibril diameters smaller than 10 nm, were difficult to resolve (not included in Figure 4.3 for this reason). For buffer neutralization, TEM images showed the same micron-sized fibril bundling as SEM images, but estimated the bundles were significantly lower in size. The 50 mg/mL sample had good agreement between imaging methods, but the 100 mg/mL sample had a completely different structure in TEM vs SEM images. TEM images illustrated a disorganized structure with a disperse fibril diameter distribution (average TEM diameter = 50 nm), compared to the organized structure of fibrils (average SEM diameter = 30nm) present at the surface of the gels in SEM images.

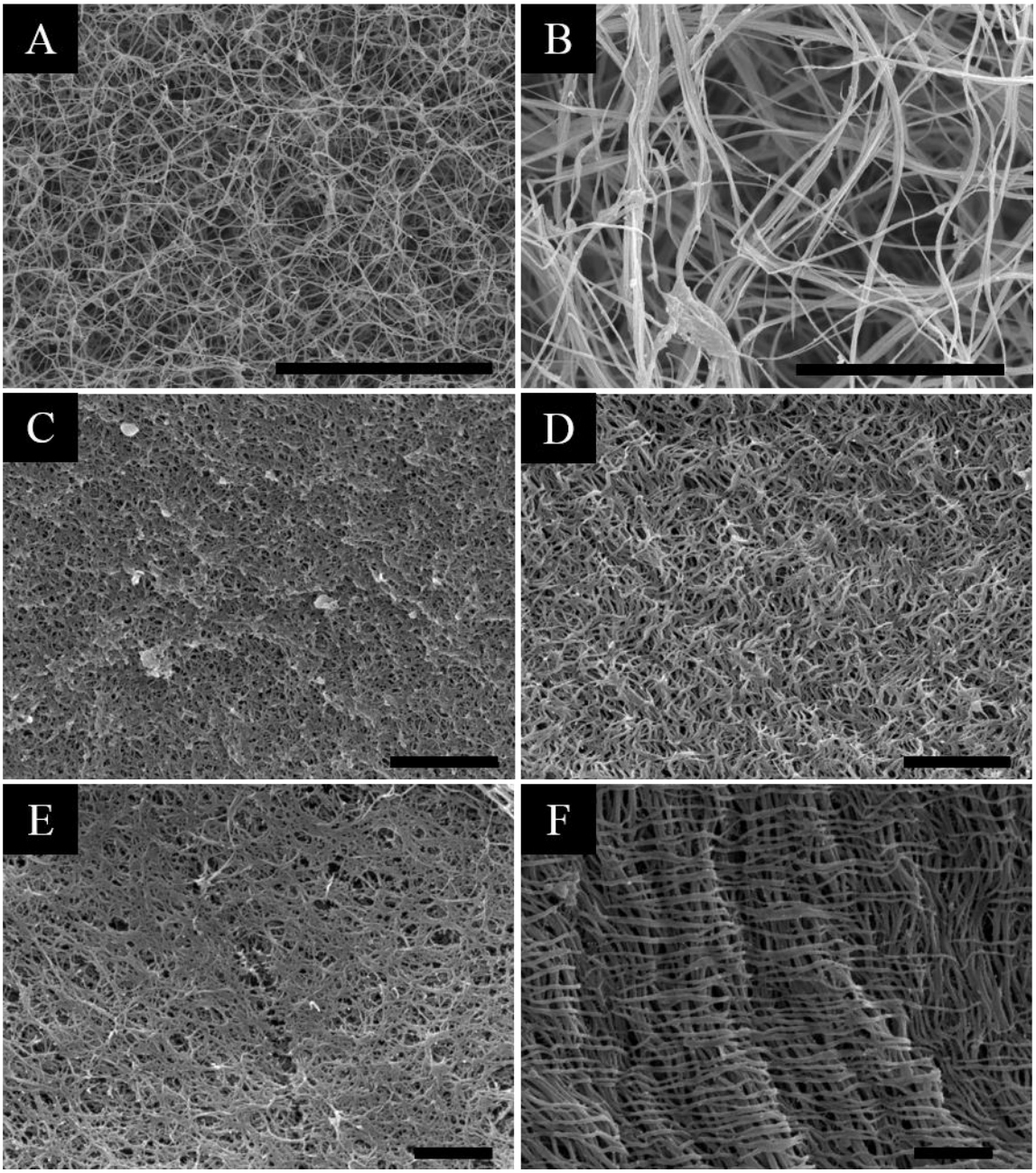

Figure 4.1: SEM images of collagen hydrogel surfaces neutralized using the ammonia vapor method (a,c,e) and the buffer method (b,d,f). The collagen concentration was varied via dialysis before gelation. The concentrations of each gel were: 5 mg/mL (a,b scale bar length = 5 µm), 50 mg/mL (c,d; scale bar length = 1 µm), and 100 mg/mL (c,d; scale bar length = 100 nm).

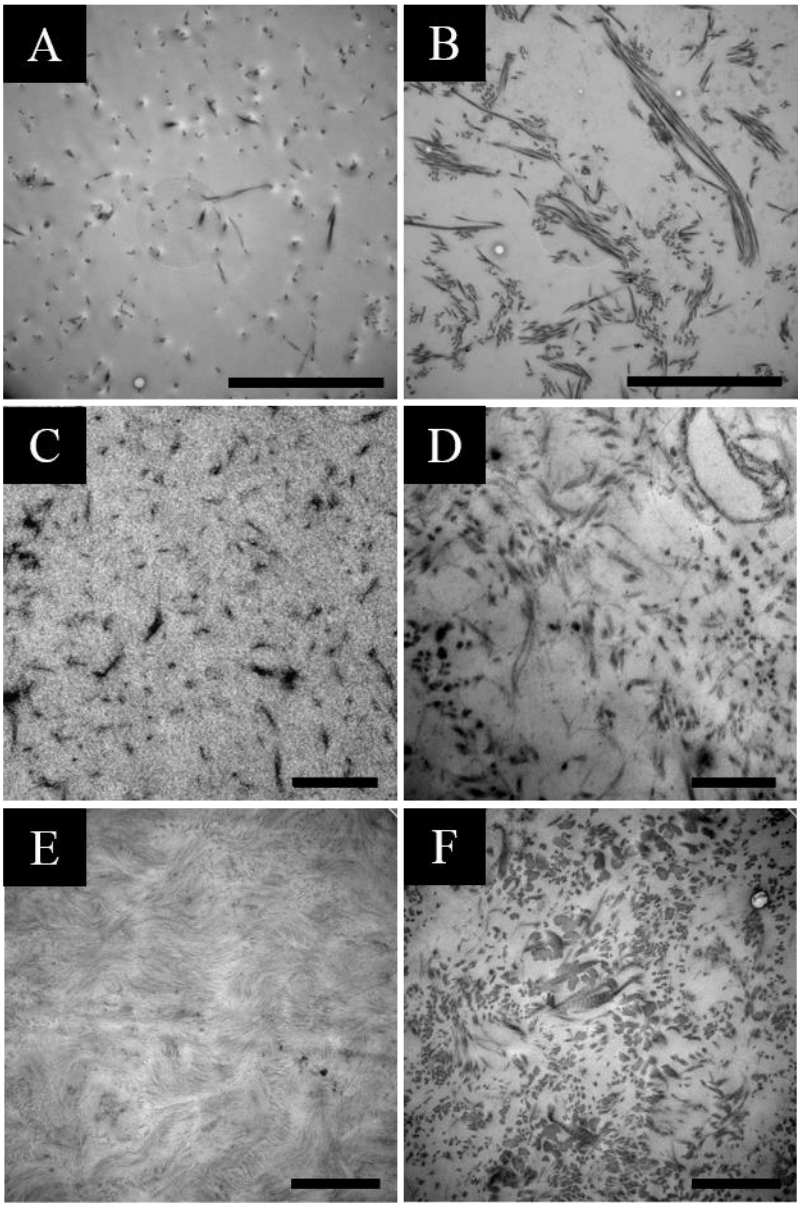

Figure 4.2: TEM images of collagen hydrogel cross-sections that were neutralized using the ammonia vapor method(a,c,e) and the buffer method(b,d,f). The collagen concentration was varied via dialysis before gelation. The concentrations of each gel were: 5 mg/mL (a,b; scale bar length = 5 µm), 50 mg/mL (c,d; scale bar length = 500 µm), and 100 mg/mL (e,f; scale bar length = 1 µm).

Figures 4.1 and 4.2 show differences in the characteristics of the final gel due to variations in collagen concentration and neutralization methods. The type of imaging used also determined what differences were observable. Experimental average fibril diameter measurements from both imaging methods can be found in Table 4.1, and the distribution of fibril diameters are presented as a histogram in Figure 4.3. The experimental and apparent spacing included in Table 4.1 are the result of quantifications of fibril spacing. Briefly, fibrils were counted manually in TEM images with known cross-sectional area, and spacing was calculated using these manual counts and theoretical estimates based on the measured average fibril diameter and collagen concentration, respectively. The formulations of these estimates are derived in the appendix.

Table 4.1: Experimental values of average collagen fibril diameter for two different neutralization and imaging methods. Errors values included are confidence limits (95% confidence).

Collagen Conc. (mg/mL)	Neutralization	Characterization Method	Diameter (nm)	Exp. Spacing (nm)	App. Spacing (nm)
5	Ammonia Vapor	SEM	58±4	-	607±42
5	Ammonia Vapor	TEM	61±3	948±33	644±35
5	Buffer Dialysis	SEM	198±23	-	2080±240
5	Buffer Dialysis	TEM	97±5	1420±160	1020±50
50	Ammonia Vapor	SEM	19±1	-	62±3
50	Ammonia Vapor	TEM	20±2	260±6	66±5
50	Buffer Dialysis	SEM	36±4	-	120±13
50	Buffer Dialysis	TEM	30±2	183±18	99±4
100	Ammonia Vapor	SEM	16±1	-	37±2
100	Ammonia Vapor	TEM	<10	<25	<25
100	Buffer Dialysis	SEM	32±3	-	75±7
100	Buffer Dialysis	TEM	51±6	191±15	120±13

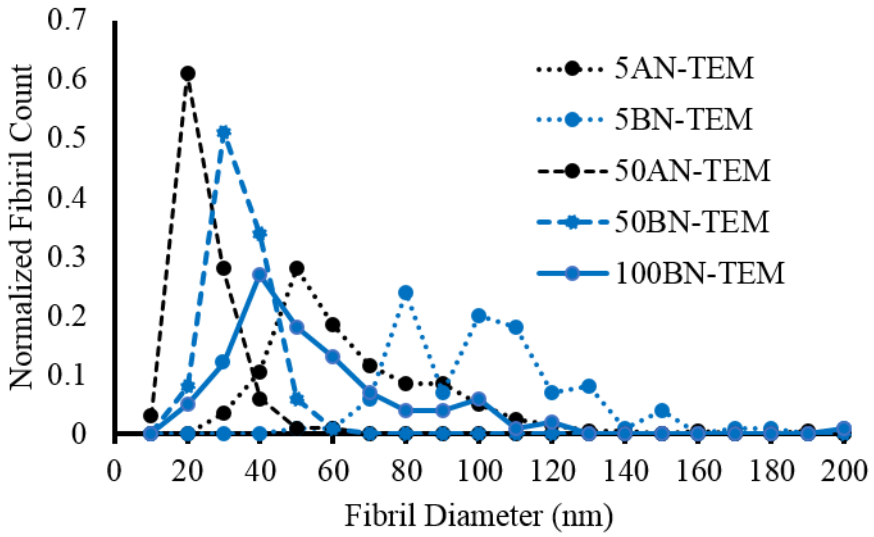

Figure 4.3: Distribution of measured collagen fibril diameters from TEM images. (Legend: AN = ammonia neutralization, BN = buffer neutralization. Number indicates collagen concentration in mg/mL)

4.3.2 UV/VIS transmittance

As expected, transmittance of each hydrogel increased with wavelength (Figure 4.4). For similar collagen concentrations, ammonia neutralization produced hydrogels with higher transparency than hydrogels produced by buffer neutralization. Buffer neutralization samples displayed a trend of increasing transmittance with decreasing collagen concentration. Ammonia vapor samples did not follow this trend, as the 5 and 50 mg/mL samples had high transparency, while the 100 mg/mL samples showed a significant decrease in optical behavior. The differences in transmittance between the low concentration gels and the 100mg/mL gel were significant in the UV range, but became small at wavelengths greater than or equal to 500 nm.

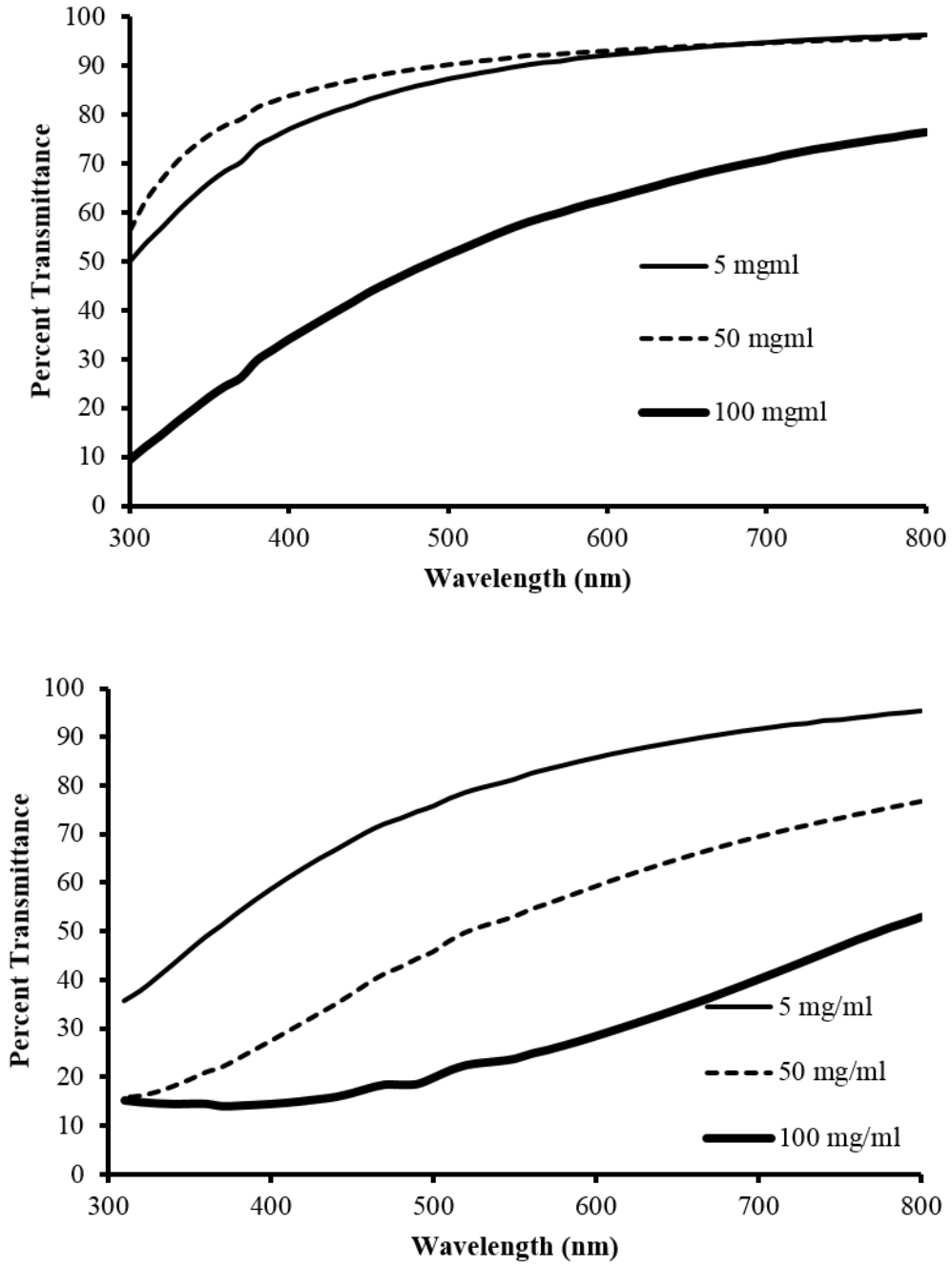

Figure 4.4: Spectral transmittance curves for ammonia vapor (top) and buffer neutralization (bottom).

4.3.3 Rayleigh scattering model: fibril diameter-fibril spacing parametric space

The Rayleigh scattering simulation results presented here were adjusted and validated against experimental data presented by van den Berg and Tan[39]. Figure 4.5 shows close agreement in spectral transmittance curves between the experimental data and simulation results when the parameters in Table 4.2 were used to simulate the cornea. For the remaining simulations, these parameters were held constant unless stated otherwise.

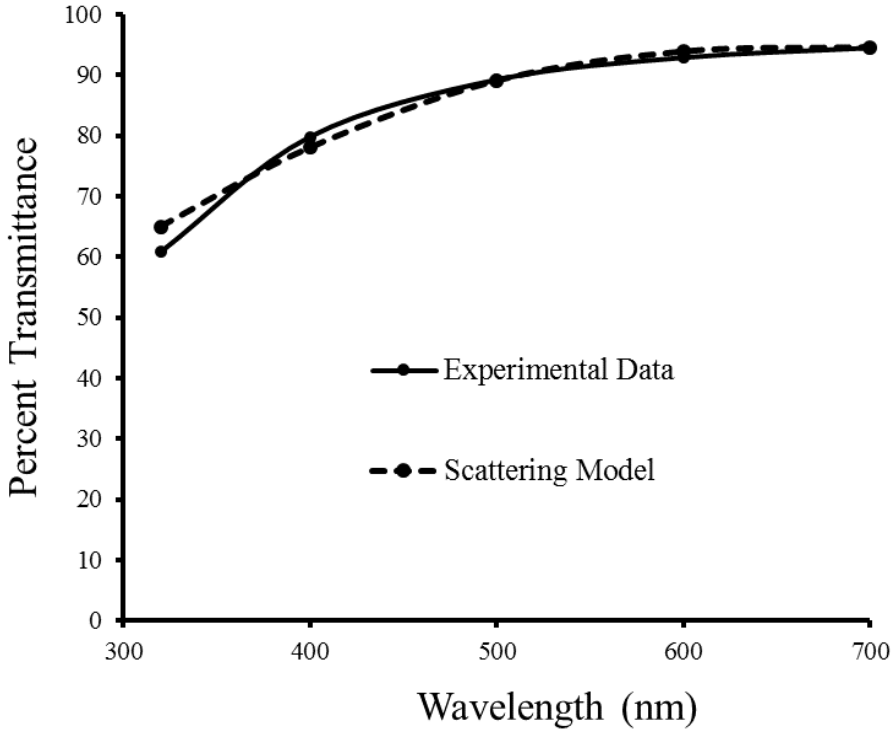

Figure 4.5: Spectral transmittance curves of the cornea based on experimental data and simulation results using the parameters in Table 4.2.

Table 4.2: Model parameters for spectral transmittance simulation of human cornea.

Parameter	Value
Number of fibrils	2000
Height: thickness of simulation plane	5
Fibril refractive index	1.413
Ground substance refractive index	1.335
Fibril diameter	30 nm
Fibril spacing	60 nm
Adjusted total thickness	526 nm

The simulation results over the fibril radius – fibril spacing plane for incident wavelengths 320, 400 500, 600, and 700 nm are shown in Figures 4.6-4.8. The gap in each figure represents arrangements that are not physically possible, i.e. average fibril diameter exceeds average center-to-center fibril spacing. Theoretical lines of constant collagen concentration were added to Figure 4.6 (top) for reference. The color scale corresponds to percent transmittance error, which was defined relative to experimental values for the cornea with the following equation:

$$\%\ Transmittance\ Error = \frac{T_{simulation} - T_{cornea}}{T_{cornea}} * 100 \qquad \text{(Eq. 4.1)}$$

Therefore, a positive transmittance error indicates that the model predicts a higher transmittance for a given fibril spacing and diameter when compared to the cornea, and a negative value indicates a lower transmittance. A white dotted line was added to the following figures to aid in visualizing the boundary between the areas of positive and negative transmittance error.

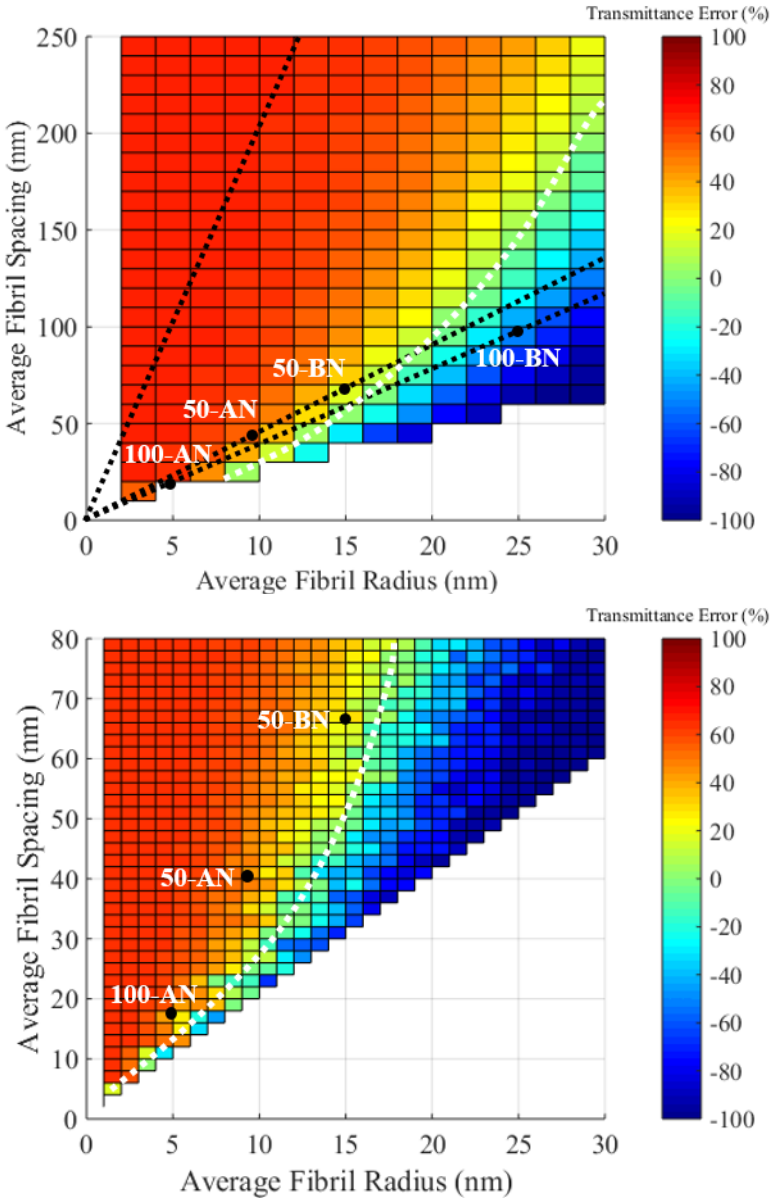

Figure 4.6: Rayleigh scattering model results for an incident wavelength of 320 nm. The bottom image is a finer mesh over a smaller range relative to the top image. The black dotted lines represent theoretical constant concentration lines. The white dashed lines represent the boundary between positive and negative transmittance errors. The black dots represent the microstructures of samples quantified with TEM (number indicates collagen concentration, BN=buffer neutralization, AN=ammonia vapor neutralization).

In Figures 4.6 and 4.7, the optical behavior of the design space was much more sensitive to lower wavelengths, while the majority of the design space for higher incident wavelengths shown in Figure 4.8 had transmittance errors close to zero. Experimental and model results were compared in Table 4.3 for incident light in the UV range. The simulation results in Figures 4.6-4.9 include black dots indicating the average fibril diameter spacing of hydrogel samples measured from TEM images. The range of fibril diameter and spacing did not include either of the 5 mg/mL hydrogel samples. This was because the 5 mg/mL buffer neutralized hydrogel had an average fibril diameter that exceeded 10% of the incident light wavelength by a large margin, and thus did not fit within the limits of the model. The 5 mg/mL ammonia neutralized sample had a smaller average fibril diameter, but the simulation computation time would be prohibitively large if the fibril spacing range was extended to 700 micrometers. However, it was apparent from the results that throughout the entire spectrum, microstructures possessing an average radius of 30 nm and average spacings greater than 200nm scatter less light than the cornea.

Table 4.3: Comparison of experimental and model transmittance results for an incident light wavelength of 320 nm. Values in parenthesis are the transmittance rankings amongst each sample with (1) being the highest transmittance and (6) being the lowest transmittance.

Sample	Avg. Fibril Diameter (nm)	Avg. Fibril Spacing (nm)	Exp. Transmittance Error (%)	Model Transmittance Error (%)
5-BN	97	1060	-38 (3)	43 (3/4)
5-AN	61	668	-6 (2)	56 (1/2)
50-BN	30	103	-74 (4)	42 (3/4)
50-AN	19	64	10 (1)	56 (1/2)
100-BN	51	124	-75 (5/6)	-19 (6)
100-AN	<10	<25	-75 (5/6)	-

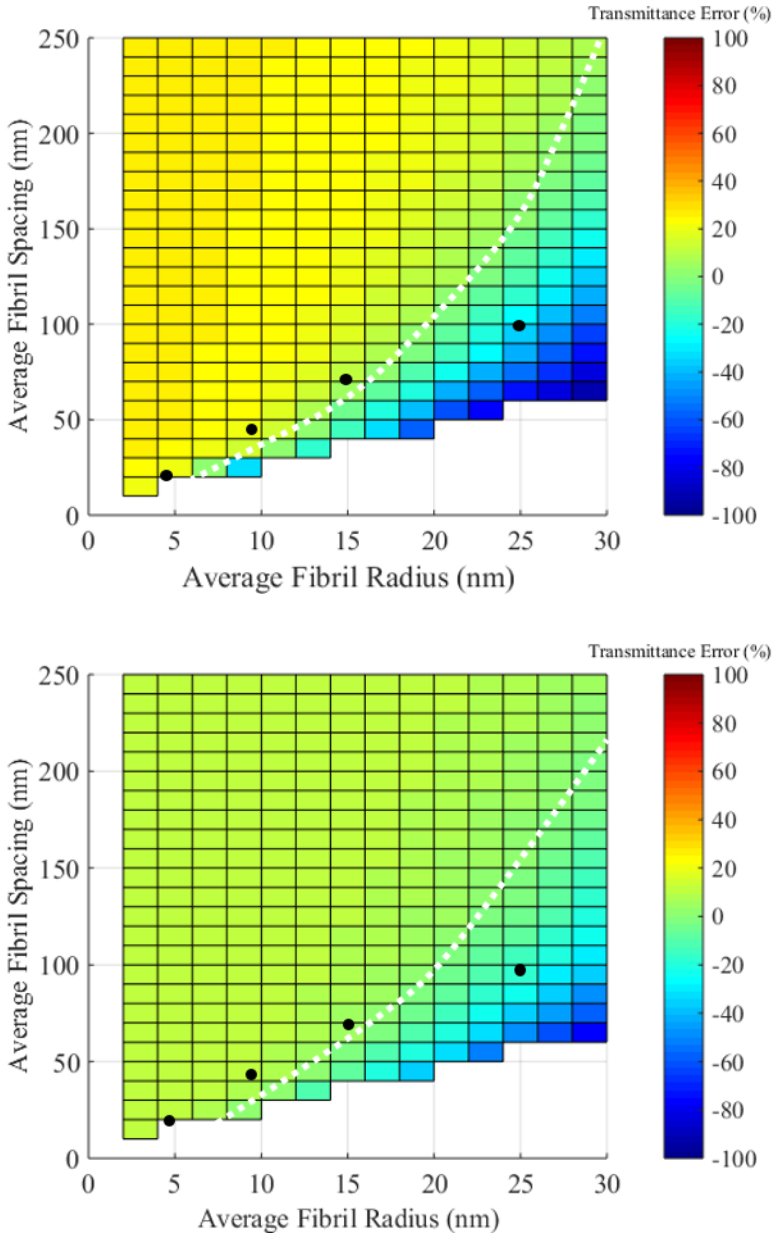

Figure 4.7: Rayleigh scattering model results for incident wavelengths of 400 nm(top) and 500 nm(bottom).

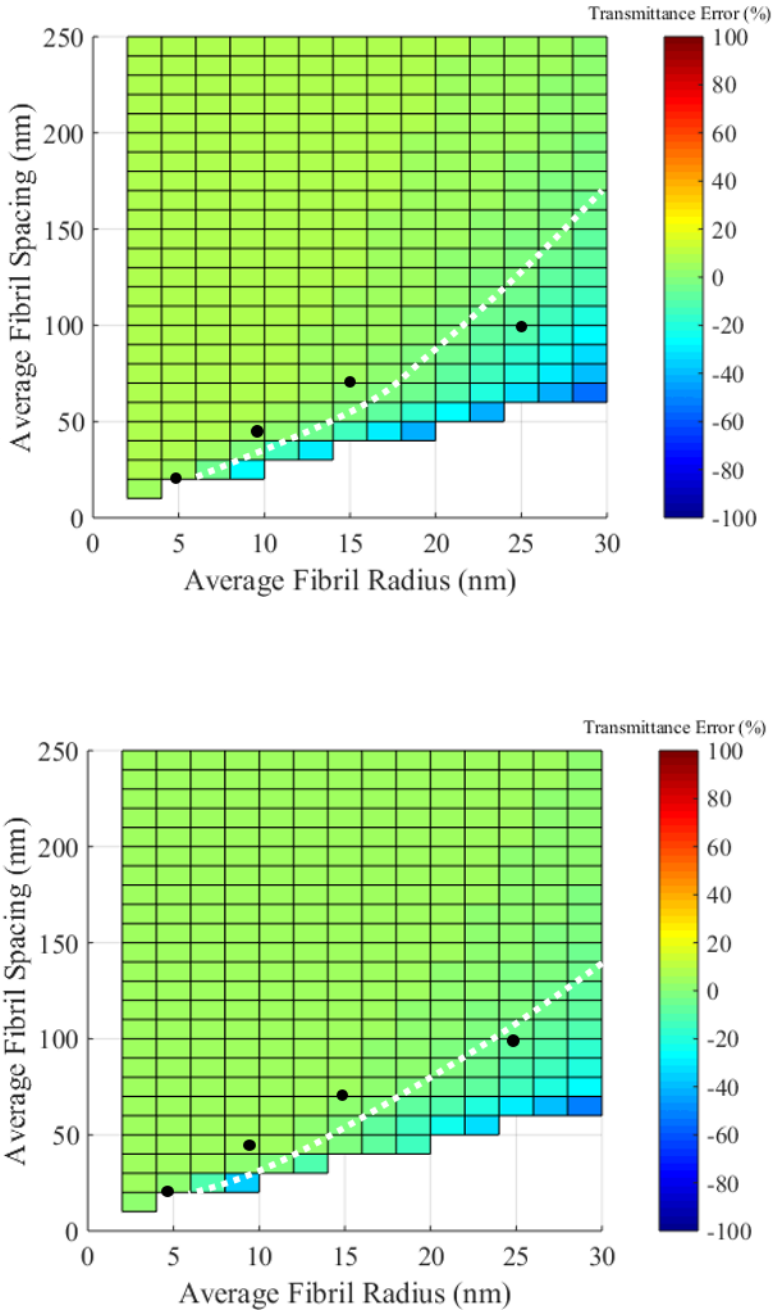

Figure 4.8: Rayleigh scattering model results for incident wavelengths of 600 nm(top) and 700 nm(bottom).

The simulation results for fibril arrays with random positions and monodisperse fibril diameters are shown in Figures 4.6-4.8. Figure 4.9 shows how optical behavior changes between monodisperse and polydisperse samples when fibril diameters have different Gaussian distributions. In Figure 4.9, the solid white line represents the positive/negative transmittance error boundary for the monodisperse case, and the dotted line represents the error boundary for polydisperse cases. There was not a significant change in the scattering results for 10% s.d., but there is a noticeable shift between monodisperse and polydisperse results for the 20% s.d. case.

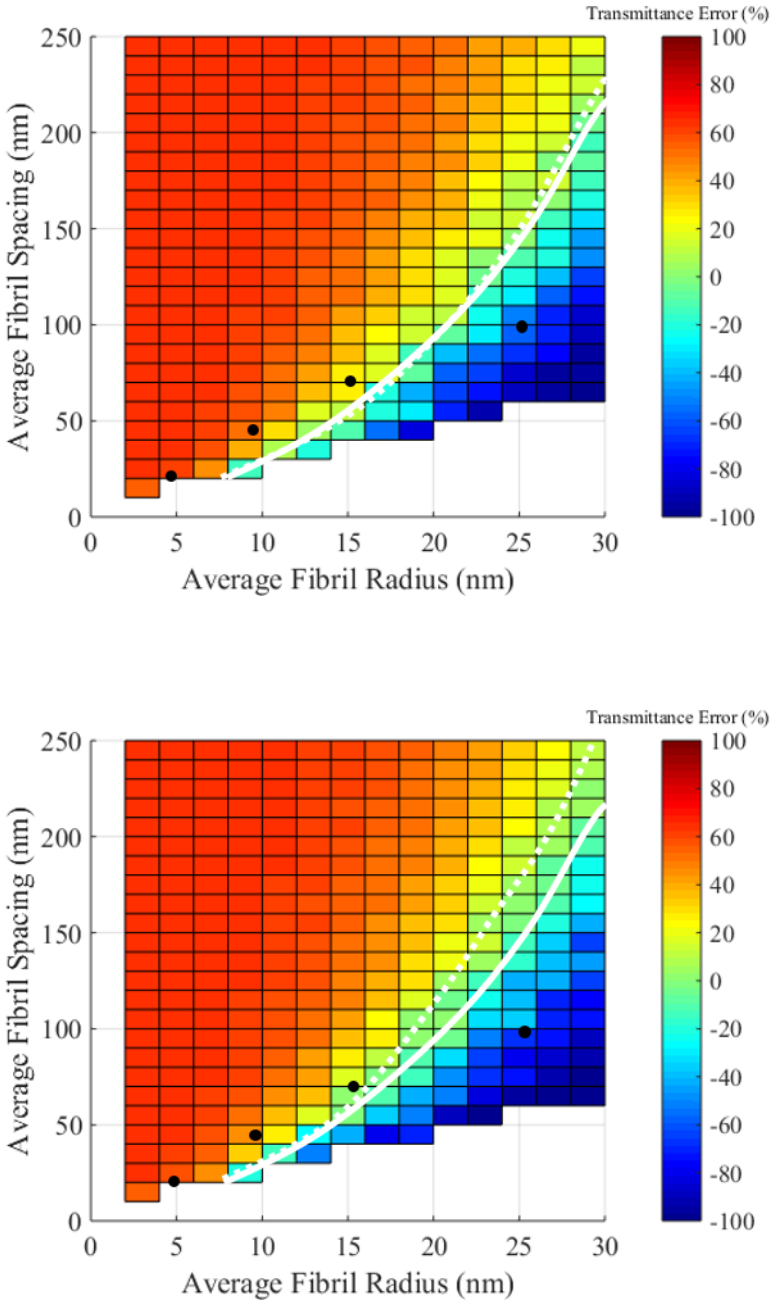

Figure 4.9: Rayleigh scattering model results for incident wavelength 320 nm for polydisperse fibril radii distributions with standard deviations of 10%(top) and 20%(bottom). Solid white lines represent boundary between positive and negative transmittance error for monodisperse case.

4.3.4 Rayleigh scattering model: fibril bundling

In the previous section, the positions of collagen fibrils were randomly placed, which is an accurate simulation of ammonia vapor neutralized hydrogels. However, it is common for fibrils to bundle into larger fibers that can be up to microns in diameter. A Mie scattering model is appropriate for particle sizes that are comparable to the incident wavelength. However, the Rayleigh scattering model can be applied to arrays of small-diameter fibrils if they are distributed so that the density of the array fluctuates spatially with wavelengths that approach the wavelength of incident light.

Figure 4.10 shows different array simulations. For each simulation, the simulation plane area, average fibril diameter, and number of fibrils were held constant. The values estimated for the cornea (fibril diameter = 30 nm, fibril spacing = 60 nm) were used for the control case with no bundling. For the bundling simulations, a random fiber center position was placed within the simulation plane area. Then, random fibril positions were placed within a circular area surrounding each fiber center position. The 'bundle' number, defined as the number of fibrils per randomly chosen fiber position, was varied from 1 to 16 fibrils. Figure 4.11 shows that transmittance of a gel decreases with an increase in number of fibrils per fiber. The transmittance was more sensitive to fibril bundling at lower wavelengths.

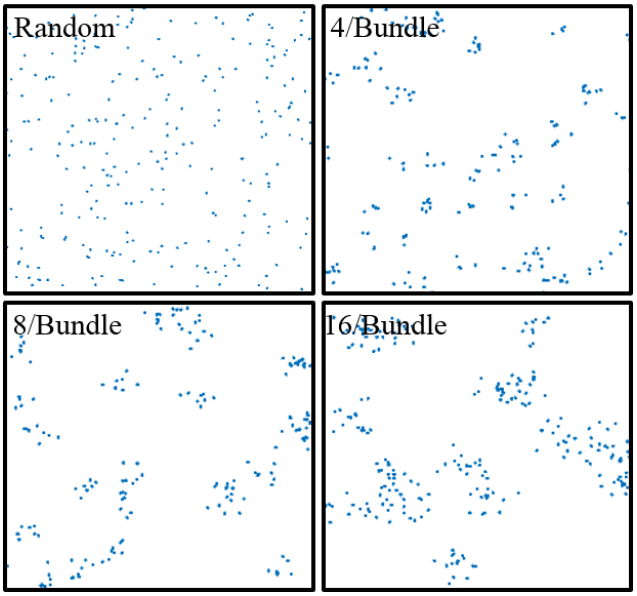

Figure 4.10: Sample of two-dimensional fibril positions different fibril bundle sizes. Number labels represent the number of fibrils per bundle.

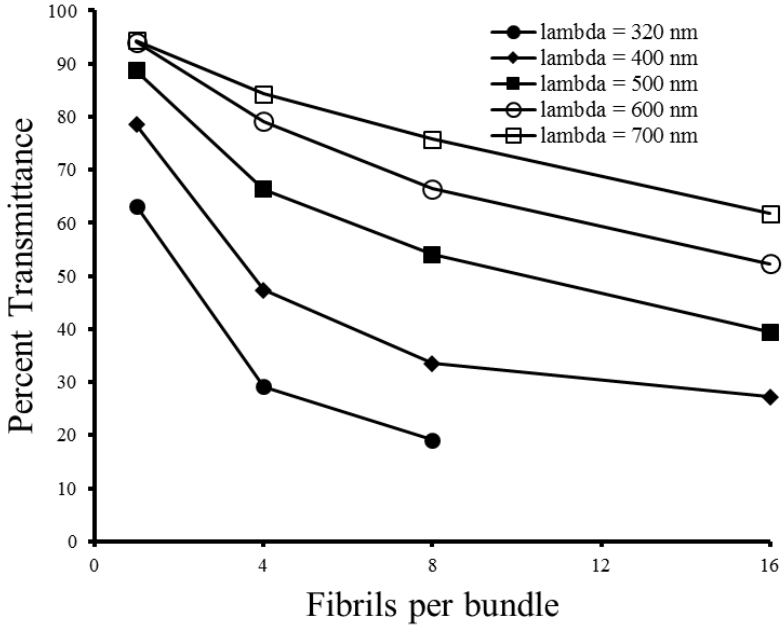

Figure 4.11: Light transmittance of simulated cornea fibril networks (30 nm diameter, 60 nm spacing) as a function of fibril bundling and wavelength of incident light.

Experimentally, it is challenging to differentiate between a large fibril and a bundle of smaller fibrils. However, the density distribution of gels can be illustrated by inverting the TEM images shown in Figure 4.2 and performing line scans in ImageJ. By plotting the intensity at each point against line scan position, spatial fluctuations can be observed. Figure 4.12 shows density fluctuations for different collagen concentrations and neutralization methods. The 5 and 50 mg/mL ammonia vapor samples had sharp peaks that were relatively evenly spaced. The 100 mg/mL ammonia vapor sample had broader, less narrow peaks that stretched anywhere from 200-500 nm. In general, buffer neutralized samples have more definitive peaks. There are broader peaks with distinct boundaries that represent fibril diameters in the range of 100-300 nm, as well as clusters of sharp peaks, which represent fibril bundles.

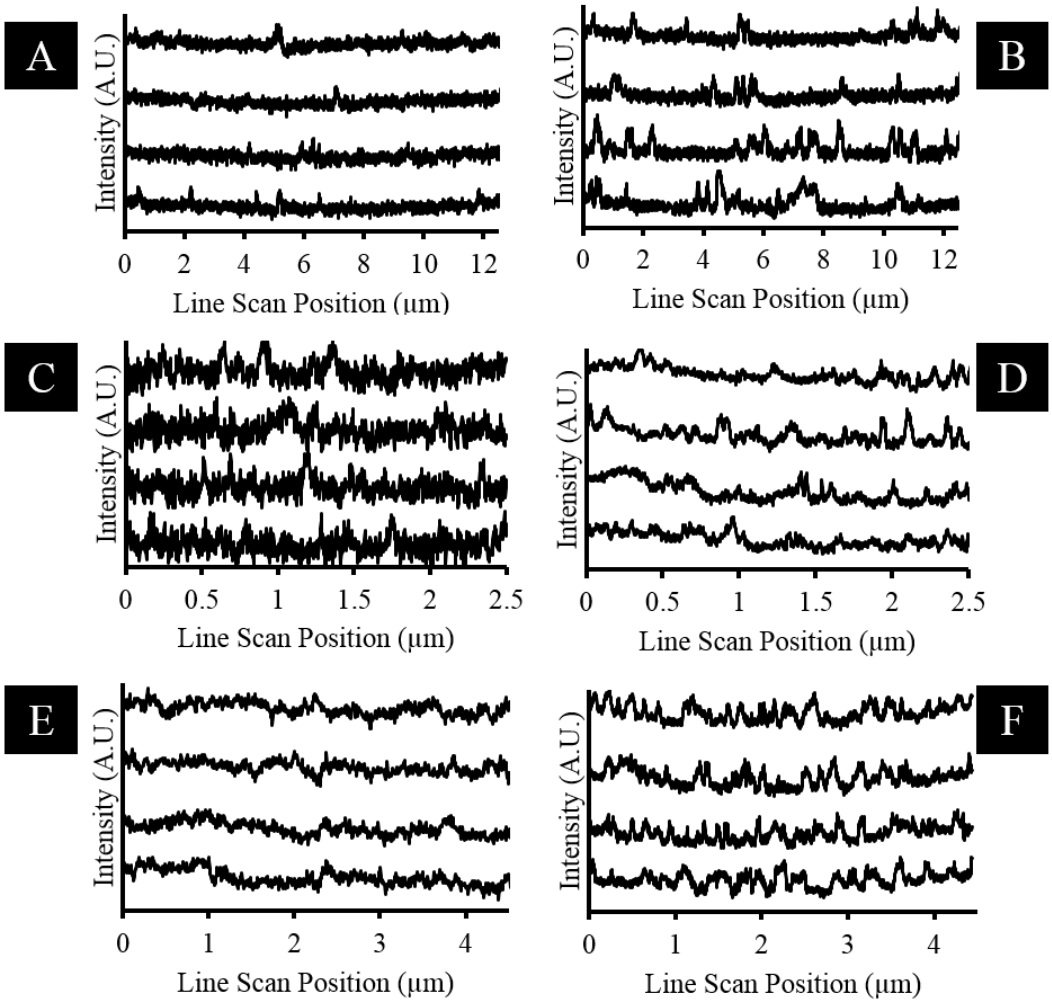

Figure 4.12: Density fluctuations represented by light intensity vs. line scan position for inverted TEM images of collagen hydrogels with concentrations of 5 (a,b), 50 (c,d) and 100 mg/mL (e,f) which were neutralized using ammonia vapor (a,c,e) and buffer solution(b,d,f).

4.4 Discussion

4.4.1 Method of microstructural characterization

The comparisons made between SEM and TEM show that SEM is an appropriate tool to characterize the surface of a gel with the caveat that topological artifacts (which do not represent

the bulk of the sample) may be present. A specific example of this type of surface abnormality is present in the SEM image of a buffer neutralized 100 mg/mL gel (Figure 4.1(f)), which shows an ordered structure with fibril diameters on the order of 30 nm. TEM images of buffer neutralized 100 mg/mL gels showed a significantly different structure that was composed of polydisperse fibril bundles with an average size of 50 nm. The cellulose membrane used for dialysis may be responsible for inducing this local ordering.

SEM preparation involves critically point drying the sample, which results in a significant reduction in volume (20-30%)[113]. Therefore, this method of characterization should not be used to quantify fibril spacing. Fullwood and Meek[114] showed the intermolecular spacing of collagen in corneal fibrils decreased by about 15% after critical point drying. A combination of these drying artifacts could account for the significant differences in fibril diameter measurements made with SEM vs. TEM. TEM preparation does not require critical point drying, and two methods of quantifying fibril spacing can be used when cross-sectional images are obtained. If the number of fibrils (or occurrences) is counted within in a known cross-section area, the average spacing can be calculated from this. One difficulty associated with TEM arose in structures composed of fibrils smaller than 10 nm in diameter, as these diameters are too small to be resolved using TEM. Additionally, it was difficult to differentiate groups of fibrils that should be treated as individual fibrils or treated as one fibril bundle using TEM.

Table 4.1 shows that the fibril spacings estimated using experimental measurements were often higher than what was predicted by the Rayleigh scattering model for given diameters and concentrations. The derivation of the equation used to relate collagen concentration, fibril spacing and diameter is shown in the appendix. The calculation uses geometrical arguments that are based on experimental data for the cornea and type I collagen. Beyond the errors associated with assumptions made in this calculation, there are many potential experimental sources of error. The fibril detecting method described above, as well as the structural changes the sample

undergoes during the sample preparation can both introduce error to experimental measurements. Fullwood and Meek[114] performed x-ray diffraction experiments which showed that intermolecular spacings of the collagen in corneal fibrils increased after gluaraldehyde fixing and ethanol drying. This would result in an overestimate of fibril diameter, and therefore an overestimate in fibril spacing. Additionally, if the estimate for collagen concentration is higher than the actual concentration, the measured spacing will be lower than what is estimated. For future experiments, a method for verifying collagen concentration experimentally such as a hydroxyproline assay should be used.

4.4.2 Neutralization and concentration of hydrogels

There are many proposed models for collagen fibril formation *in vitro*. In general, most believe that the process consists of an initial nucleation, followed by linear and lateral growth steps[73,78,79,90,115–118]. The specific regions of the collagen molecule that are involved in each step are still debated, however it is commonly accepted that hydrophobic and electrostatic interactions both have a role in fibrillogenesis, and therefore the resulting microstructure. Figures 4.1-4.2 show that the buffer neutralization of collagen solutions results in larger fibrils/fibril bundling when compared to ammonia vapor neutralization, and therefore more opaque gels. Buffer neutralized samples had a much higher ionic strength than ammonia vapor neutralized samples (0.6 M vs 1 mM). Many groups have reported that increased ionic strength results in longer reaction times, larger fibrils, and an increase in opacity[73,75,90,119–123]. It has been proposed that electrostatic interactions play a significant role in nucleation and linear growth during fibril formation[78,80,83,115,124–129]. Therefore, samples with high ionic strength would limit the number of collagen molecules involved in nucleation and linear growth, allowing more lateral growth to occur. This preference for lateral vs. linear growth would result in larger fibrils and an increase

in light scattering. It is important to note that hydrophobic interactions have also been shown to play a significant role in collagen molecule fibril formation[78,115,124,128–131], but these interactions are more significant at close ranges than electrostatic interactions.

Another parameter to consider that may have influenced fibril formation was the neutralization temperature. Buffer neutralization was performed at 37 °C and at this temperature, samples gelled after approximately 30 min. This was rapid compared to the 3 h gelation time for samples incubated at room temperature. The buffer/room temperature samples were more opaque than the samples neutralized at 37 °C, and therefore were not included in the results. Some groups have shown the same decrease in opacity when incubation temperature is increased[122,129]. However, in some cases (especially at higher pH values), room temperature neutralization has produced smaller fibril diameters than neutralizations performed at 37 °C[74].

In comparison, ammonia vapor neutralization was performed at room temperature. Fibril formation did not occur after multiple hours at 4 °C, and raising the temperature past ambient conditions did not change the microstructure for ammonia vapor neutralization. This temperature independence beyond ambient temperatures could be due to the elevated pH of 11, compared to a pH of 8 in buffer neutralized samples. Previously, research groups have shown that higher pH values produce smaller fibrils[74,122,132]. It has been suggested that this is due to the deprotonation of histidine and ionization of other residues which increases electrostatic interaction[128]. Once again, by assuming nucleation and linear growth kinetics are heavily dependent on electrostatic interactions, this would explain an increase the number of fibrils formed, fibril length, and and a reduction in the average fibril diameter. Therefore, an increase in pH may be another contributing factor that reduces fibril diameter when comparing ammonia vapor neutralization to buffer neutralization for samples with the same collagen concentration.

For buffer neutralized samples, the dilute concentration (5 mg/mL) yielded the largest fibril diameters, while the higher concentrations had significantly reduced fibril diameters. An

increase in fibril diameter occurred when the collagen concentration was increased from 50 to 100 mg/mL. This is similar to previous findings from other groups[90,115,121]. However, the ammonia neutralized samples displayed different behavior with an inverse relationship between fibril diameter and collagen concentration. It has been suggested that lateral growth of fibrils depends on the number of collagen molecules available and their ability to move within the gel. This indicates that nucleation and linear growth of fibrils occurs much faster than the process of lateral fusing of molecules and other aggregates.

Ammonia vapor neutralization poses the advantages of raising the pH of a solution without changing the volume/concentration, and does not require mixing or dialysis. However, even with rapid ammonia vapor neutralization, the 100 mg/mL concentration had significantly reduced spectral transmittance when compared to the native cornea. Therefore, this method should be altered to maximize the collagen concentration used to make transparent gels, which will result in an optimal material with desired optical and mechanical behavior. After discussing the dominating microstructural features for light scattering, methods for achieving an optimal structure will be proposed in the following discussion.

4.4.3 Rayleigh scattering model: limitations

Before discussing the results obtained from numerical simulations, it is important to mention the assumptions and limitations of the Rayleigh scattering model used. As mentioned previously, the equations used are for infinitely long cylinders that possess the same parallel direction normal to incident light. The hydrogels synthesized in this work are obviously composed of amorphous cylindrical fibrils with finite length. Therefore, the model does not account for light scattering outside of the two-dimensional plane considered. The model also assumes that fibril diameters are significantly smaller than the incident wavelength. A good rule

of thumb for Rayleigh scattering is that fibrils diameters should be uniformly programmed with a maximum diameter equal to 10% of the incident light wavelength. The results presented here include fibril diameters up to 30 nm, therefore caution should be taken when making conclusions regarding large fibril diameters at lower wavelengths.

The last source of error worth mentioning is the method used to scale up from the micro to millimeter scale. The direct summation method treats every fibril with the same incident electric field. This assumption is valid for small simulated thicknesses, but the difference in incident light on an anterior fibril compared to a posterior fibril becomes significant as the number of scattering events that occur between them increases. Therefore, the average number of fibrils that were present with respect to the simulated thickness was minimized, and the Beer-Lambert law (Eq. 3.1) was utilized to scale this micron-sized response up to the thickness of a cornea. The value of 2000 fibrils per simulation yielded good agreement with experimental data, and indicated an optimal balance between simulating a minimal thickness and simulating enough fibrils to produce a repeatable average response.

4.4.4 Rayleigh scattering model: fibril diameter-spacing

Considering the assumptions and potential sources of error from the simulation model and experimental quantification, it is unreasonable to use this model as an accurate predictor of collagen hydrogel optical behavior. However, using this model to test hypotheses and simulate general trends of materials can be very useful. For instance, the model predicts that there is not a significant difference in light transmittance between crystalline and random two dimensional fibril spacing arrangements[110]. However, the size of the fibrils seems to be very important for mimicking transmittance of the cornea in the UV and near UV spectral range.

By considering Figure 4.8, one can see that most of the simulated design space is similar to the cornea for incident wavelengths of 600 and 700 nm. However, when considering UV wavelengths that can damage anterior parts of the eye, the simulations show only limited areas of the design space mimic the cornea's function. Table 4.3 shows a comparison between experimental transmittance data, and transmittance values predicted by the model for an incident wavelength of 320 nm. The model was able to predict the order of transmittance values observed experimentally, but overestimated bias of transmittance for all samples. In order to explain this discrepancy, one needs to look at the microstructural features found experimentally which deviate from the assumed ideal (unidirectional, monodisperse) microstructure assumed by the model.

Collagen fibrils formed *in vitro* usually have a polydisperse fibril diameter distribution and assemble in fibril bundle structures. Polydispersity was simulated for 10% and 20% Gaussian distribution conditions with 320 nm incident wavelength. Both cases yielded shifts in the positive/negative percent transmittance error line that divides the microstructural space. As expected, this shift is more apparent for the 20% case. The 50 and 100 mg/mL buffer neutralized samples are located in a region sensitive to polydispersity effects, and both samples possess fibril diameter distributions with standard deviations over 20%. Therefore, a significant reduction in fibril size variance of these hydrogels would improve their optical behavior. On the other hand, the 5 and 50 mg/mL ammonia vapor neutralized hydrogels have a narrow size distribution and are in areas of the design space that do not change significantly with polydispersity. For these cases, other features must be investigated to explain the overestimates of transmittance present in the model.

4.4.5 Rayleigh scattering model: bundling

According to Benedek[107], the optics of the cornea are dependent upon its refractive index distribution in space. This means that average fibril spacing is only one component of the more significant spatial density distribution. The bundling simulation results shown in Figure 4.11 indicate this is true as light transmittance decreases when fibrils assume bundle arrangements (whose densities fluctuate over length scales comparable to the incident wavelength). This was supported with experimental observations for the 5 mg/mL hydrogels. Even though the concentration of collagen remained constant, the transmittance of the buffer neutralized sample was significantly reduced compared to the ammonia vapor neutralized sample due to the bundling of smaller fibrils.

Line scans of inverted TEM images in Figure 4.12 show fluctuations in density (and therefore refractive index) in two dimensional space. These images show that fluctuations in buffer neutralized samples occur over larger distances when compared to ammonia neutralized samples. A more quantitative characterization of spatial density distribution can be performed using Fourier analysis on the same TEM images. This method was attempted for TEM images in Figure 4.2, but the amorphous nature of the fibril networks caused a noisy spectrum that made it difficult to compare frequency components between different gels. For future experiments, more images with sharp contrast between fibrils and surrounding space must to be collected. The bounds in these images must also be significantly larger than the periodicity of the structure being measured. Once a balance between resolution and sample area size is struck, FFT analysis can be performed on multiple images and averaged to reduce noise, and Fourier magnitude and frequency components of different microstructures can be compared.

4.4.6 Fibril nodes in hydrogels

The simulation results for bundle features described above explain why 5 mg/mL buffer neutralized samples had such poor optical behavior. However, the model overestimated the transmittance of ammonia-neutralized samples that do not contain bundled structures (Table 4.3). This indicates that microstructural features not represented in the model affect the optics significantly for these samples. From SEM images, the intersections between collagen fibrils, defined as 'nodes', may be a key characteristic feature that reduces the optical transparency of hydrogels.

Node formation is inevitable for amorphous collagen hydrogels synthesized *in vitro*. While increasing the collagen concentration results in smaller fibril diameters in the ammonia neutralization method, the number of nodes and fibrils per node is likely to increase due the increase in fibril density. The size of each node is a function of number of fibrils per node and fibril diameter, and the nodal contribution to optical behavior depends on the nodal size and frequency of occurrence. Additional SEM images in Figure 4.13 show nodes, but some of these may have formed during the drying process. It is reasonable to suspect these nodes contribute significantly to light scattering considering that the size of the nodes varies from 100 nm to micrometers in size. Future work should include further characterization to detect these nodes, their size, and their distribution. Confocal microscopy seems a feasible experimental technique for this purpose, and has been used in the past to quantify the corneal microstructure [133,134] as well as collagen hydrogels[135,136].

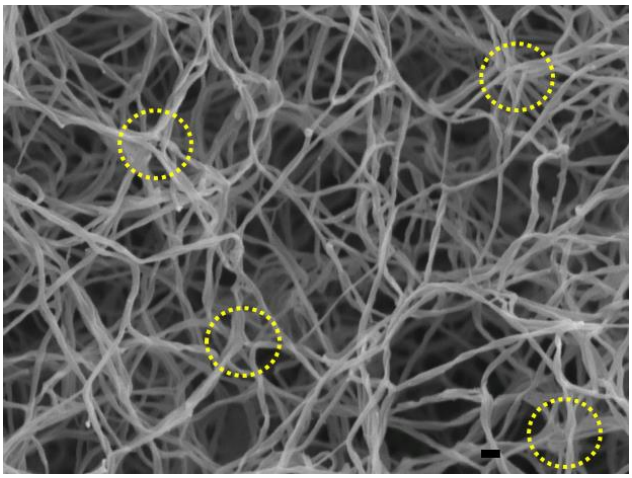

Figure 4.13: SEM image of 5 mg/mL hydrogel (ammonia vapor neutralized). There are many nodes present (yellow dashed circles) which are hundreds of nm in size. (scale bar length = 100 nm)

It is interesting to note that as mentioned in section 4.1, the dependence of corneal optics on crystalline microstructure was questioned by Benedek and Goldman[111] due to the transparent nature of shark cornea containing amorphous fibril arrangement with the same collagen concentrations and fibril diameters as the human cornea. This disorganized matrix is called the Bowman's layer and is embedded in a proteoglycan matrix[137]. TEM images of this layer show fibrils that are oriented in different directions without nodes due to the proteoglycans' spacing function. Therefore, to fabricate highly concentrated transparent collagen hydrogels *in vitro*, large-scale alignment of fibrils with reduced nodal contributions is necessary, and this likely requires an additional component present to maintain fibril spacing during fibrillogenesis

4.5 Conclusion

In this chapter, collagen hydrogels' optical and microstructural properties were characterized using UV/VIS spectrophotometry and electron microscopy. Ammonia vapor neutralization was shown to be superior for collagen hydrogel synthesis due to the resulting array

of small fibrils and optical transmittance similar to the cornea in the gels it produces. However, the optical transmittance of ammonia neutralized gels is reduced significantly if the collagen concentration exceeds 50 mg/mL. When compared with ammonia vapor neutralization, buffer neutralization resulted in fibril radius distributions with higher deviations and mean values. The transmittance for samples gelled using buffer neutralization was also significantly lower than the native cornea, even at low concentrations.

Simulation results indicated that hydrogels with low collagen concentration mimic the spectral response of the cornea at higher wavelengths, but have the potential to transmit more UV light than the cornea. Higher concentrations of collagen (≥ 100 mg/mL) have a higher sensitivity to changes in the fibril size distribution, and an increase in dispersity of fibril sizes can significantly reduce light transmission. Additionally, fibril bundling simulations show how the distribution of fibril positions can increase light scattering, even when fibril density and size are held constant.

In order for collagen hydrogels to mimic the function of the cornea, the mechanical properties must be enhanced while maintaining the cornea's characteristic spectral transmittance. This can be accomplished by improving the optical transmittance of hydrogels with collagen concentrations in the 100 mg/mL range. The results in this chapter suggest that the best way to accomplish this is to minimize the number of large size (>10% of incident light wavelength) 'bundles' and 'nodes' that occur throughout the gel, as well as narrow the distribution of fibril diameter sizes to 10% standard deviation or below. Combining ammonia vapor neutralization with fibril alignment techniques should result in mechanically sound hydrogels with improved optical transmittance. The next two chapters focus on two different techniques to reduce dispersity of fibril sizes as well as induce fibril alignment.

Chapter 5

In vitro alignment of collagen fibrils using magnetic nanowires

5.1 Introduction

This chapter describes the use of magnetic nanowires to induce alignment of collagen hydrogels. It was hypothesized in Chapter 4 that alignment improves the optical transparency of collagen hydrogels. Many groups have been successful in inducing alignment of collagen fibrils, and a brief review of these current methods is prudent for understanding the motivation for a new alignment method.

Many groups have induced fibril alignment of collagen hydrogels by applying a compressive plastic strain to pre-formed collagen gels[138–142]. This process results in a densification and orthogonal anisotropy that improves the mechanical properties of hydrogels. This method has been proposed for tissue engineering applications that do not require optical clarity such as skin, bone, and other connective tissue, and results in fibril aggregation causing an increase in light scattering. Directional freezing of collagen solutions also induces alignment of a collagen fibril structures for tendon tissue replacement[143], but contains micron sized pores not favorable for light transmission. Therefore, these methods are not suitable for collagen hydrogels used in cornea replacement.

Electrospinning has been shown to produce aligned collagen fibril structures[144,145]. Wray and Orwin proposed a highly aligned structure with small fibril diameters for corneal replacement, which backscatters less light than unaligned hydrogels[146,147]. However, electrospinning collagen hydrogels for corneal replacement would make it difficult to incorporate

cells throughout the bulk of the structure and the required deposition setup presents problems for manufacturing unique geometries such as the hemispherical shape of the cornea.

Other various methods have induced unidirectional fibril alignment by application of shear forces on the micro[148,149] and bulk scale[150,151], and the electrochemical field[152], and strong magnetic fields[153,154]. However, these methods produce alignment in only one direction and therefore the mechanical properties in the unaligned directions are reduced. Torbet et al. combatted this by varying the magnetic field direction during the fibril formation process[154]. Giraud-Guille et al. showed that ordered collagen structures similar to the cornea can be achieved with collagen concentrations above 40 mg/mL using a slow evaporation process[93,94,154]. Saeidi et al. showed the same molecular crowding effects for collagen concentrations above 100 mg/mL using dialysis[92]. TEM images showed the gels possessed a stacked aligned lamellar structure similar to the cornea. Using the same methods, recent results have shown that collagen hydrogels with concentrations of 90 mg/mL possess transmittance values of 87% in the 380-780 nm wavelength range[155].

The magnetic nanowire alignment method proposed here offers the advantage of producing a bimodal fibril orientation at low collagen concentrations using a simplistic procedure that can be easily replicated in a common lab setting. Magnetic nanowires were chosen because they can be aligned easily with a weak magnetic field, and they can be fabricated with an arrangement of diameters, lengths, and surface chemistries. It was hypothesized that nanowires with high aspect ratios will induce fibril alignment at the bulk scale resulting in transparent gels. The following sections characterize the alignment of the fibril matrix, the resulting optical transmittance, and an example of contact alignment between synthesized nanowire-collagen matrices and arachnoid cells.

5.2 Methods

Figure 5.1 shows a schematic of the interaction between nanowires and collagen molecules. The specific methodology for this process is described in section 3.4. Briefly, the nanowire surfaces were functionalized with a PEG molecule that had amine groups exposed at their terminal surfaces. A cross-linking agent (CDI) was used to link the amine groups of the nanowires to the hydroxyl groups on the surface of collagen molecules. The nanowire concentration with respect to the collagen solution volume was varied from low (10^4 wires/mL), medium (10^5 wires/mL), to high concentrations (10^6 wires/mL). The sample was then aligned with an applied magnetic field, and collagen fibril formation was induced with ammonia vapor.

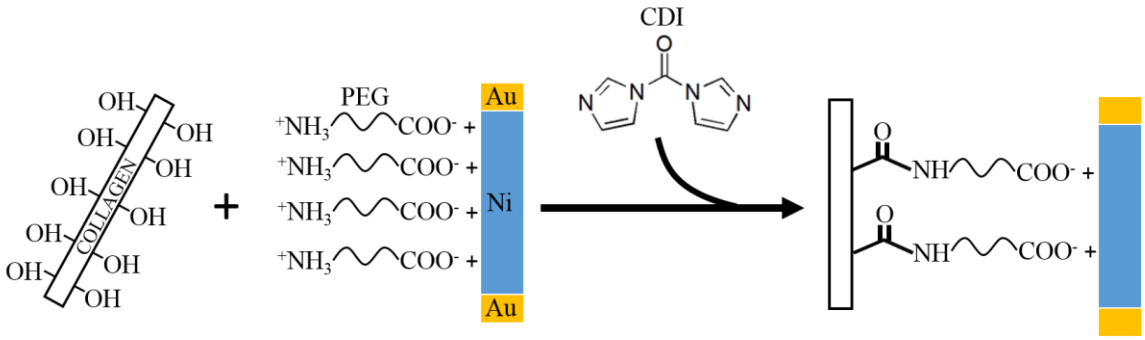

Figure 5.1: Covalent linking mediated by CDI between available hydroxyl and amine groups of collagen molecules and nanowires, respectively.

The aligned structures produced using this method were characterized with SEM (section 3.13), polarized light transmission measurements (section 3.9), and DIC microscopy (section 3.10). Spectral transmittance was measured to quantify the optical behavior of the aligned gels compared to control structures. In order to observe any contact guidance the synthesized matrix imparted on cells, DIC/fluorescent microscopy was used to image arachnoid cells seeded on top of aligned structures *in vitro* (section 3.10).

5.3 Results

5.3.1 DIC and SEM microstructural characterization

In order to characterize the alignment response of collagen fibrils in the presence of nanowires, DIC microscopy was used in conjunction with two cross-polarizers. Figure 5.2 and 5.3 show synthesized matrices of varying nanowire concentrations and constant CDI and collagen concentration. There was an apparent 'zig-zag' pattern present for the high nanowire concentration samples that was only vaguely present at the edge of medium nanowire concentration samples, and not visible in samples with concentrations of CDI lowered to 2 mM. This zig-zag pattern indicated that there was alignment of collagen fibrils in two orthogonal directions. From the DIC Figure 5.2(a), the average angle between the fibrils is 95.7° and s.d. = 8.0°, and from the DIC Figure 2(b), the average inter-fibril angle from 100 pairs was 88.3° and s.d. = 14.6°. Additionally, the average angle between the nanowire (applied field) direction and the fibrils is 41.58° and s.d. = 6.48°, both of which make an approximate 45° angle with the applied magnetic field/magnetic nanowire direction.

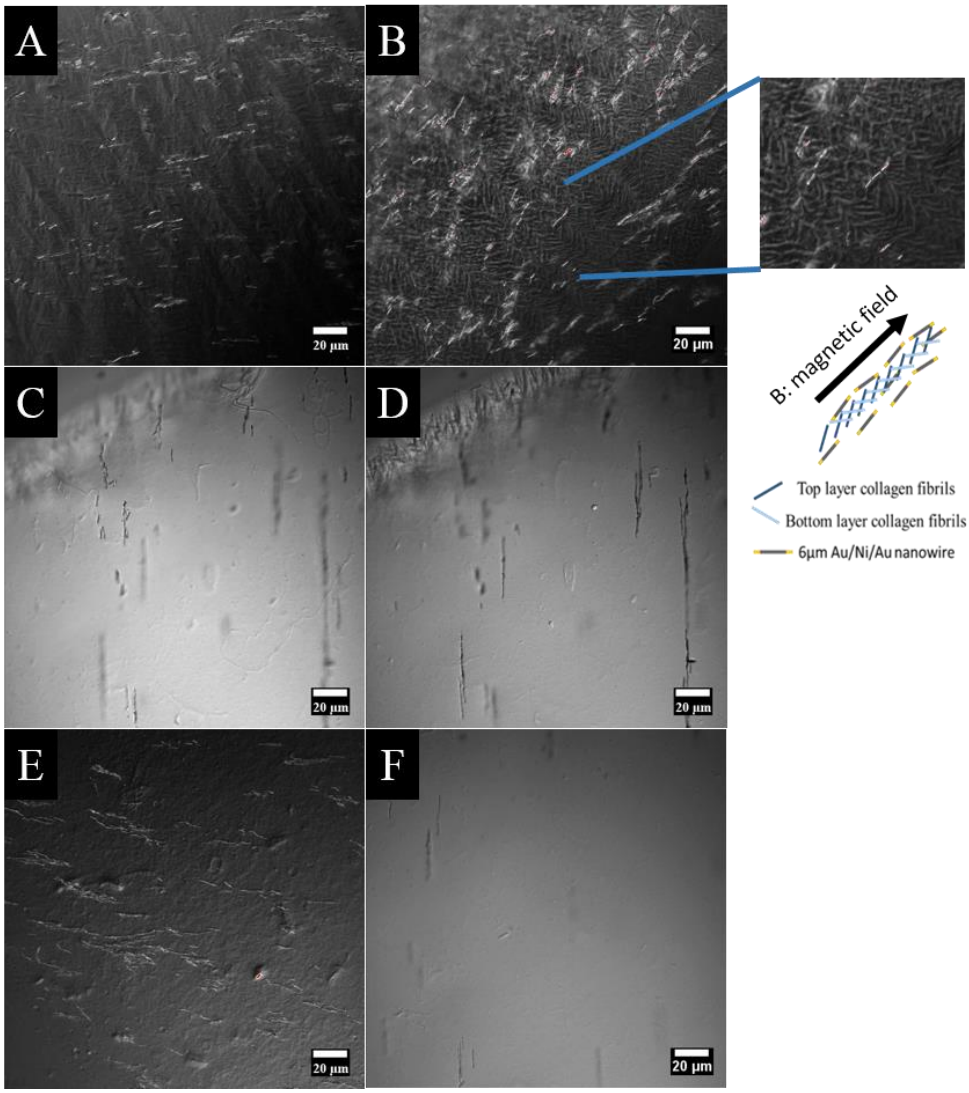

Figure 5.2: DIC images of nanowire loaded (160 nm diameter, 6 µm length) collagen hydrogels aligned with an applied magnetic field. (a,b) 200mM CDI concentration with 'high' concentrations of nanowires. Nanowires align in the direction of the magnetic field, and collagen fibrils form a 'zig-zag' pattern that is present throughout the entire sample. (c,d) 200 mM CDI concentration with 'medium' concentration of nanowires. Two different z-planes show a 'zig-zag' pattern at the edge of the sample, but this pattern is not present in the middle of the sample (f). No collagen fibril alignment is observed for low 2mM CDI concentrations, even with high nanowire concentrations (e).

In order to resolve the finer features of the aligned matrices, SEM imaging was performed. Clear alignment of collagen fibers was observed in images of hydrogels aligned with 50 nm (Figure 5.3 (a,b)) and 160 nm diameter nanowires (Figure 5.3 (c,d)). Figure 5.3 (b) and (d) include inset images of the 50 nm and 160 nm diameter nanowires. There was no fibrillar alignment observed for gels that did not use CDI to cross-link nanowires to collagen molecules (Figure 5.3 (e,f)). As it is difficult to distinguish between nanowires and collagen fibers at the magnifications shown in Figures 5.3, higher magnification images were taken and EDX analysis was performed. This was done to ensure that the observed alignment was indeed due to cross-linking between nanowires and collagen fibers (Figure 5.4).

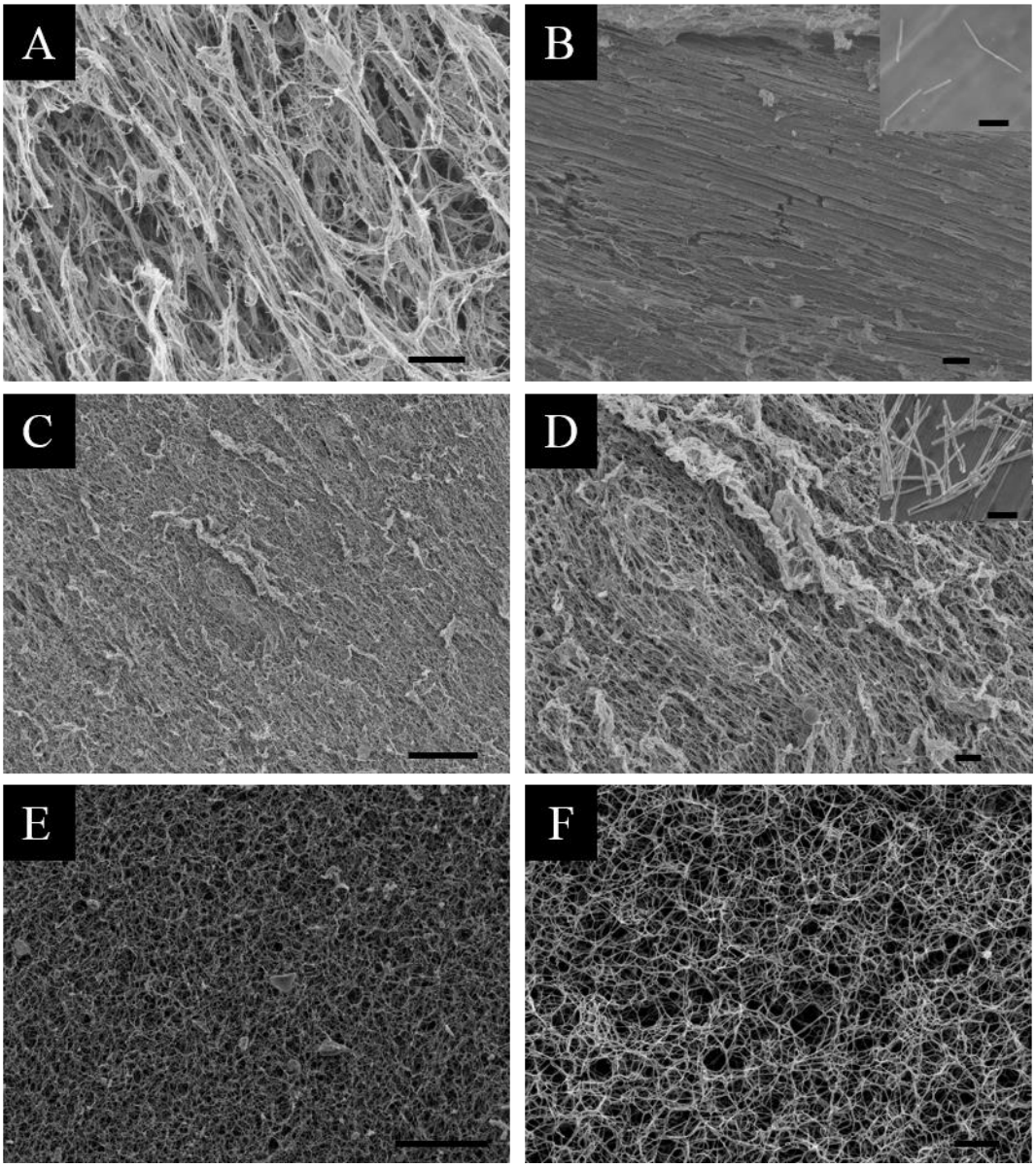

Figure 5.3: SEM micrographs of aligned collagen-nanowire matrices (high nanowire concentrations). (a,b) collagen-nanowire hydrogels aligned with 50 nm diameter nanowires (5.3(b) inset: 50 nm diameter bare nanowires). (c,d) collagen-nanowire hydrogels aligned with 160 nm diameter nanowires (5.3(d) inset: 50 nm diameter bare nanowires). (e,f) collagen-nanowire hydrogels do not experience alignment with 160 nm diameter nanowires when CDI is not present as a crosslinker. (all scale bar lengths are 1 µm)

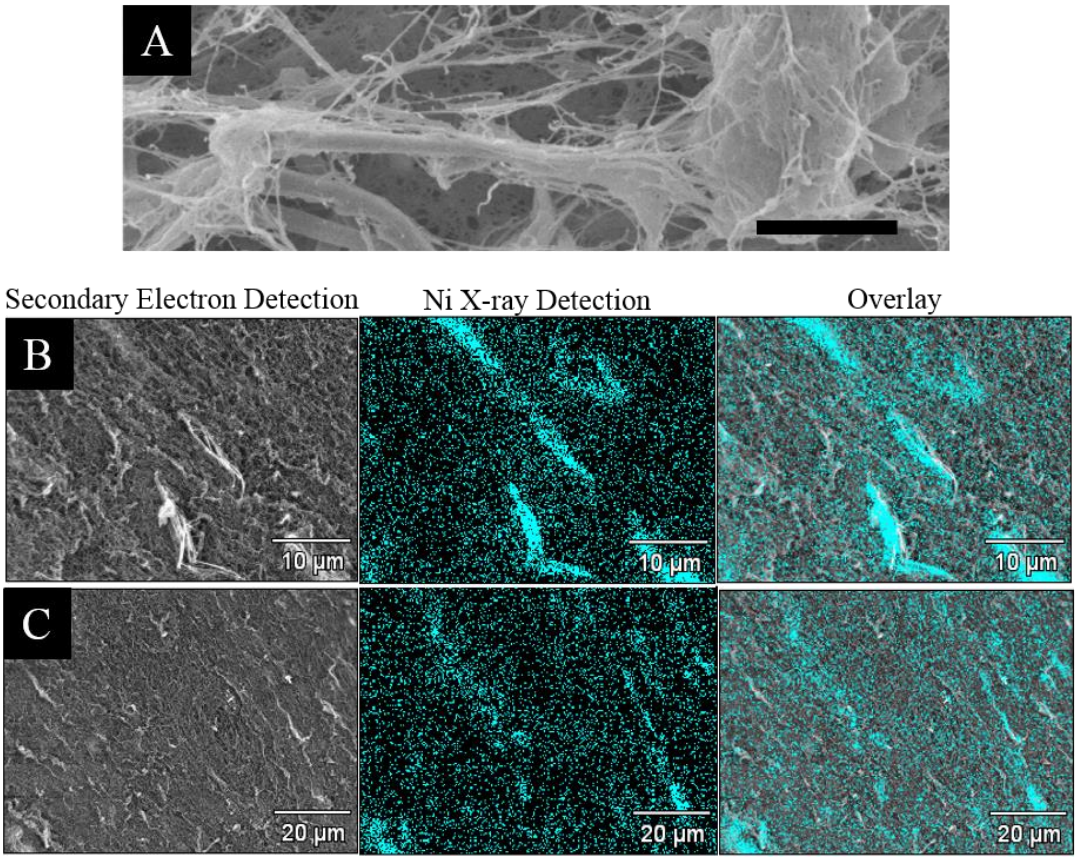

Figure 5.4: High magnification SEM and EDX analysis show alignment of nickel nanowires (and therefore, applied field direction) and interactions between nanowires and collagen fibers. (a) SEM micrograph showing collagen fibers attached to the Ni surface of Au/Ni/Au nanowire (scale bar length is 1 µm). (b,c) EDX analysis of the nanowire-collagen cross-linked matrix formed under uniform magnetic field shows spatial X-ray mapping of Ni (cyan color).

5.3.2 Polarized and UV/VIS light transmittance

To further characterize the anistropy of the aligned nanowire-collagen matrices, transmittance of polarized light was measured through the matrix as the polarization of light was rotated by 360°. The magnetically aligned nanowire-collagen matrix had an associated sinusoidal

waveform (Figure 5.5). This behavior was unique to the aligned matrix, as neither the blank control nor the unaligned matrices exhibited this characteristic sinusoidal response.

The transmittance waveform from the magnetically aligned matrices shows four peaks in transmittance as the polarization of light is rotated by 360 degrees. This is consistent with the structure suggested by the DIC images from Figure 5.2 (a,b). There are two main directions along which the fibers are oriented. Therefore, when the incident light direction is parallel to one of these directions, a maxima in transmittance will be observed. From the proposed zig-zag structure from Figure 5.2 (a,b), four peaks in transmittance are predicted. This prediction is verified here using polarized-light transmisttance measurement.

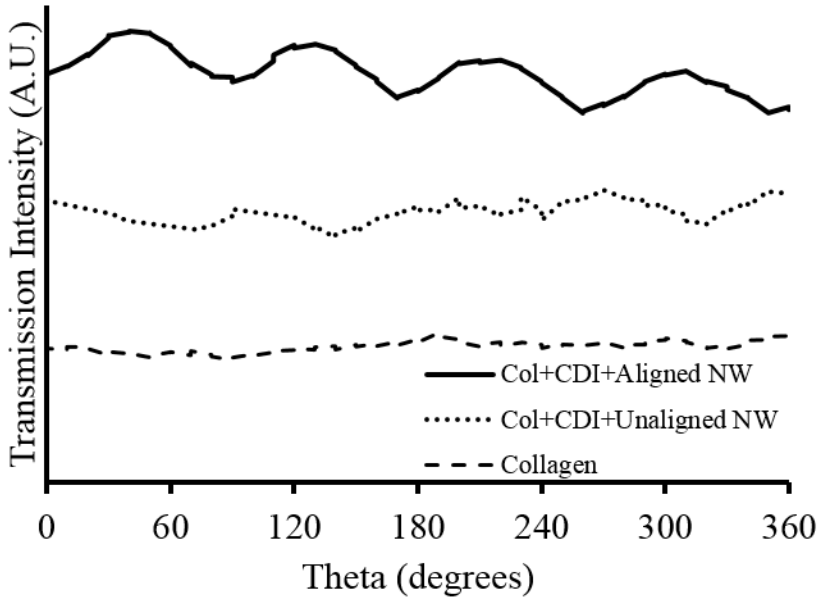

Figure 5.5: Polarized light transmittance vs orientation of polarization of incident light with respect to the fixed sample. The sinusoidal nature of the waveform measured in the aligned nanowire case corresponds to anisotropy of the matrix suggesting nanowire-collagen alignment. (Placement of all three curves on the y-axis is arbitrary).

Figure 5.6 shows the spectral transmittance of aligned and unaligned samples (50 nm diameter wires). The aligned samples were more tranparent than the unaligned samples, and this difference was largest at lower wavelengths. The 160 nm diameter nanowires produced a similar result (Figure 5.7), but it appeared that the larger wires contributed to light scattering as well, indicating that there are favorable (and possibly optimal) nanowire dimensions with respect to optical transmittance.

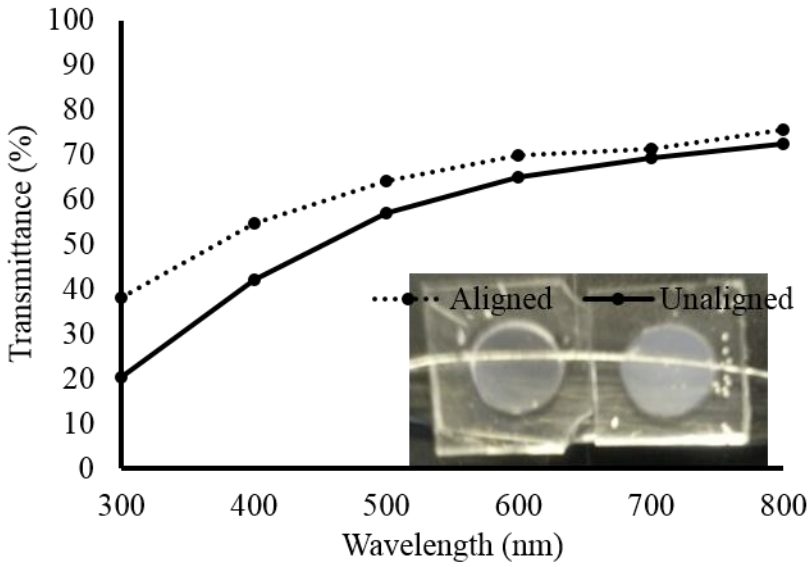

Figure 5.6: Spectral transmittance of collagen-nanwire samples. Both samples have the same composition (5 mg/ml of collagen, 10^6 wires/mL (50 nm wire diameter)), but the hazy unaligned sample has a random fibril orientation, whereas the more tranparent sample has an aligned structure (samples are 5 mm in diameter).

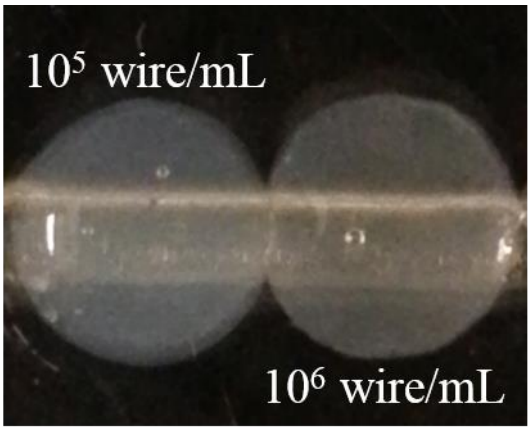

Figure 5.7: Photomicrograph of aligned samples (5 mm diameter) with two different concentrations of 160 nm diameter wires. This image shows that 160nm diameter nanowires produce semi-transparent gels similar to those produced with 50nm diameter wires.

5.3.3 Contact Alignment of Arachnoid Cells

Arachnoid cells were used to assess the ability of an aligned matrix to induce cell alignment as these cells are sensitive to topographical cues from the extracellular matrix[156]. Arachnoid cells were plated on magnetically-aligned matrices and incubated until they reached 75-80% confluence (~ 3 days) under controlled environmental conditions (37 °C, 5% CO_2). The cells were fixed and stained with a blue nuclear stain (DAPI) and a green actin filament stain following incubation. The hypothesis here was that actin stress fibers (green), which control the cytoskeletal shape of the cells, would exhibit an aligned geometry in related to the alignment direction of the collagen matrix. This, in turn, would influence the spreading of cells on this substrate, imparting them with a definite anisotropy.

As shown in Figure 5.8 (a-c), an anisotropy is indeed observed in the actin stress fibers (green) of arachnoid cells in relation to the underlying aligned matrix. In contrast, the same cells

do not exhibit this behavior when plated on control collagen gels (without nanowires) as shown in Figure 5.8 (e).

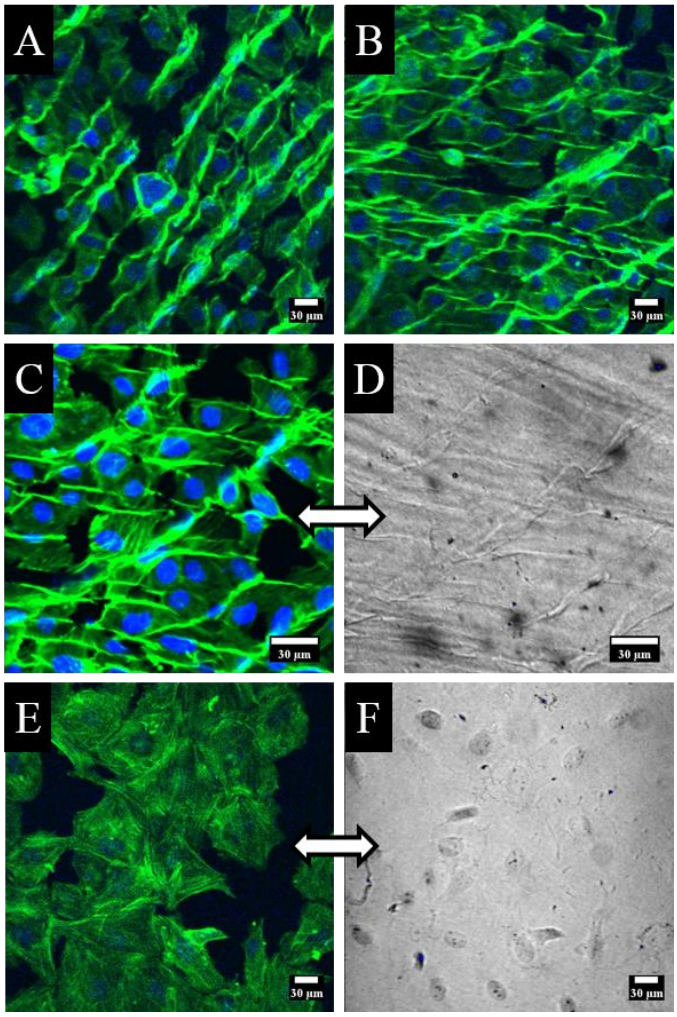

Figure 5.8: Contact alignment of arachnoid cells in response to magnetically aligned nanowire-loaded collagen synthetic matrices. (a,b) Cellular actin stress filaments (green) are observed to accumulate and stretch in nanowire aligned directions using confocal fluorescence microscopy (10x magnification). Nuclei are stained blue. Throughout the sample, actin filaments were aligned along two directions according to the zig-zag pattern of nanowire alignment proposed in figure 2. (c,d) Fluorescence and corresponding DIC images taken at 20x magnification. (e,f) Fluorescence and corresponding DIC images of control (unaligned, no wires) hydrogel.

5.4 Discussion

5.4.1 Mechanism of alignment

Figure 5.2 (a,b) shows that nanowire concentrations on the order of 10^6 wires/mL were required to achieve alignment throughout the bulk of gels. When the concentration was lowered to 10^5 wires/mL, the 'zig-zag' pattern was only present at the edge of samples (Figure 5.2 (c,d)). This was most likely due to surface tension forces, which caused the nanowires to aggregate at the edges of the sample inducing localized alignment. This did not occur for the 'low' nanowire concentration of 10^4 wires/mL (not pictured).

The other parameter critical in inducing fibril alignment was CDI concentration. For the same 'high' nanowire concentration (10^6 wires/mL), lowering the CDI concentration from 200mM to 2 mM was the only variable changed and resulted in aligned and unaligned fibrils respectively (Figure 5.2 (e)). This CDI dependence eliminated the possibility that these structures are aligned due to the applied or local nanowire magnetic field alone. Additionally, Figure 5.3 agreed with this result, indicating amine groups on the nanowires alone were not enough to induce alignment, and that the degree of covalent bonding between the hydroxyl groups of the collagen and amine groups of the nanowires dominated the interaction.

Polarized light transmission studies were performed to validate DIC microscopy results. Collagen fibrils are known to display birefringent behavior, i.e. refractive index is dependent on polarization and direction of incident light. Therefore, if one preferred direction of fibril orientation exists in a plane perpendicular to incident light, there will be two maxima spaced by 180°. The polarized light transmission study showed four peaks when the light polarization angle was rotated a full 360°, suggesting the 'zig-zag' pattern present in DIC images represents two dominant fibril orientations. The same transmission pattern exists in areas of the cornea that assume a predominantly orthogonal fibril arrangement[157]. This arrangement was also quantified

by measuring fibril directions seen in Figure 5.2 using ImageJ. From the DIC Figures 5.2(a) and (b), the average angle between the fibrils is 95.7°±8.0° and 88.3°±14.6°, respectively. These averages were based off of 100 measurements. While the bimodal arrangement was present throughout the entire sample, these measurements showed the angle between the two dominant fibril directions varied throughout the sample.

An explanation for this bimodal orientation is still unknown. A method using spherical magnetic particles to align collagen gels appeared to utilize small scale shear forces from particles flowing through the collagen solution prior to fibril formation[148]. However, this only induced unidirectional fibril arrays and particles were observed to collect at the surface nearest to the applied magnet. For the present study, samples were placed in the center of a uniform magnetic field and nanowires did not appear to move through solution prior to or during fibril formation.

Collagen molecules have been shown to orient themselves perpendicular to strong applied magnetic fields[154]. Once again, if magnetic forces were dominating fibril orientation, one would expect the fibrils to align in one direction perpendicular to the applied field and to the nanowire orientation direction.

One possible explanation of bimodal arrangement is that the helicity of collagen molecules dictates their orientation with respect to the nanowire longitudinal axis as cross-links form. This helicity defines the pitch of twisting that is observed in liquid crystalline collagen solutions[93]. An imaging technique capable of resolving the collagen molecule arrangement upon cross-linking to a nanowire surface, such as atomic force microscopy, could be used to test this theory. More experiments are required to understand how nanowire aspect ratio, length, concentration, and surface modifications effect collagen alignment.

5.4.2 Optical properties

Figure 5.6 shows that the alignment induced by 50 nm diameter nanowires resulted in an increase of transmittance across the UV/VIS spectrum. This was hypothesized to occur in the results and conclusion of Chapter 4. As mentioned, the assumed explanation for this change in optical behavior is due to the reduction in interfibril junctions (nodes) relative to an amorphous hydrogel of the same collagen concentration. In order to strengthen this theory, further microstructural characterization, such as TEM or confocal microscopy, should be performed on amorphous and aligned gels in order to compare the frequency of nodal occurrences.

It was shown in Figures 5.2 (a,b) and 5.7 that 160 nm diameter wires were capable of aligning collagen fibrils, which resulted in an increase in transmittance. However, the increase in transmittance with 160nm wires was not as great as with 50 nm diameter nanowires. This is due to the larger spatial fluctuation in refractive index for the larger diameter resulting in a higher nanowire scattering contribution. The scattering model described in Chapter 3 could be used to estimate the scattering contributions due to the nanowires, and these simulation results can provide an estimate for the maximum nanowire concentrations that should be used for a given nanowire diameter.

5.4.3 Contact alignment of arachnoid cells

Many groups have already aligned collagen matrices and observed contact alignment with various cells[148,154,158–161]. Guo et al. aligned glioma cells in unidirectionally aligned collagen scaffolds[148]. Huang et al. used shear force to align concentrated collagen gels, and observed endothelial cell actin filament alignment in same the direction as the collagen scaffold[159]. They also showed that cell viability was improved for endothelial cells seeded onto aligned substrates vs. unaligned controls. Kirkwood et al. aligned concentrated collagen gels with flow induced shear forces, and showed fibroblast actin filaments grow parallel to the aligned substrate[158].

However, no group to our knowledge has shown collagen gels induce orthogonal contact alignment of actin filaments. In this study, arachnoid cells were able to attach and proliferate on aligned collagen-nanowire matrices. Fluorescent staining of actin filaments within the cells showed that the cytoskeleton of the cells adopted the same biomodal anisotropy as the underlying synthetic matrix. Arachnoid granulations act as a barrier to keep large molecules out of cerebrospinal fluid[162]. Additional experiments to study how cytoskeletal alignment affects arachnoid cell permeability are currently being performed.

These same contact alignment experiments can be performed with different types of adherent cells. Additionally, the method presented here can be modified to seed cells throughout the bulk of the gel by neutralizing the collagen-nanowire solution at low temperatures, and spiking in cells prior to fibril formation. Due to the orthogonal microstructure, this method may be a good alternative to present protocols for forming artificial bone, arterial, and corneal scaffolds. To further explore tissue-engineering applications, this method must be optimized for higher concentrations of collagen, and relevant mechanical, optical, and transport properties must be characterized.

5.5 Conclusion

A method for synthesizing collagen hydrogels with specific structural and topographical properties was described. Collagen fibril networks with a bimodal orientation distribution were obtained upon cross-linking collagen molecules with functionalized magnetic nanowires and inducing formation of fibrils in a uniform magnetic field. SEM, DIC imaging and polarized light transmittance studies were performed to characterize these aligned artificial matrices. Additionally, contact alignment experiments with arachnoid cells were carried out to prove that

the gels are capable of inducing bimodal alignment in cells. Finally, it was shown that this type of alignment resulted in an increase in spectral transmittance.

Future work should include the quantification microstructural features such as fibril diameter, nodal concentration/size, and spatial density distribution with TEM and/or confocal microscopy in order to explain the increase in transmittance for aligned gels. Using this method to improve the optics of 100 mg/mL collagen gels is an obvious next step. At a first glance, this will require nanowires with significantly smaller diameters than the ones used in this study, and a design of experiments approach should be used to optimize the length, diameter, and concentration of nanowires with respect to light transmittance.

Additionally, characterization of the mechanical properties of these aligned hydrogels must be carried out to understand how the anisotropic microstructure responds to mechanical loads applied in different directions. It has been shown that lamellae in the posterior two thirds of the cornea have two preferred orthogonal directions[163]. This can explain the improved strength of the cornea when a load is applied in these two orthogonal directions compared to intermediate directions[164]. Comparisons in mechanical behavior of these aligned hydrogels to that of the cornea will dictate whether or not a bimodal fibril arrangement has sufficient mechanical strength for corneal replacement. Variations of the procedure presented can be used to introduce multiple layers of bimodal arrangement that are offset by a given rotational angle. For instance, a varying magnetic field can be applied that induces a twisting arrangement of the magnetic nanowires with respect to the thickness of the sample. Alternatively, a layer-by-layer manufacturing process similar to the one used by Torbet et al.[154], can produce thin layers polymerized on top of one another with a different magnetic field orientation in every layer. This would be different than the techniques used previously in that it would not require high magnetic fields.

Chapter 6

In vitro alignment of collagen fibrils – nanocrystalline cellulose

6.1 Introduction

This chapter describes an alternative method to improve the optical behavior of collagen hydrogels with collagen concentrations above 100 mg/mL. The cornea has an estimated collagen concentration of 130 mg/mL. Therefore, producing a transparent material in this concentration range is important for mimicking the optical and mechanical behavior of the cornea. The method described in Chapter 5 shows potential for aligning collagen hydrogels, but future studies must be performed to apply this method to high collagen concentrations. The present chapter uses the crystalline surface moieties of cellulose to regulate the microstructural properties hypothesized in Chapter 4 to increase spectral transmittance of collagen hydrogels with 150 mg/mL collagen concentrations.

As mentioned in the background (Chapter 2), the collagen fibril formation process is dominated by electrostatic and hydrophobic/hydrophilic interactions between available amino acid side chains. It has been observed that fibril diameter is regulated with type V collagen molecules[97,165] and proteoglycans[166–168] *in vitro* and *in vivo*. The type V collagen molecules sterically hinder lateral growth of fibrils, while proteoglycans prevent bundling of fibers by bonding to neighboring collagen fibril surfaces and creating an electrostatic force balance which maintains uniform spacing between fibrils.

Cellulose (Figure 6.1) is the most abundant polymeric material found on earth. It has numerous applications such as paper, food and pharmaceuticals. Cellulose has been used to enhance mechanical properties of composite materials while being non-toxic and

biocompatible[169,170]. There are many techniques to reduce microcrystalline cellulose (MCC) to nanocrystals (NCC)[171–178]. The present study used an ultra-sonication technique to produce NCC particles. These particles were mixed with highly concentrated collagen solutions and neutralized to form anisoptropic collagen hydrogels with improved optical properties when compared to amorphous control hydrogels. Fibril diameters and alignment were characterized with electron microscopy, while spectral transmittance was measured with a spectrophotometer, and the chemical interactions between NCC and collagen were examined with FT-IR spectroscopy. When the surface chemistry of NCC particles are altered, the results support the hypothesis that polar groups of NCC particles are vital for fibril alignment and diameter regulation.

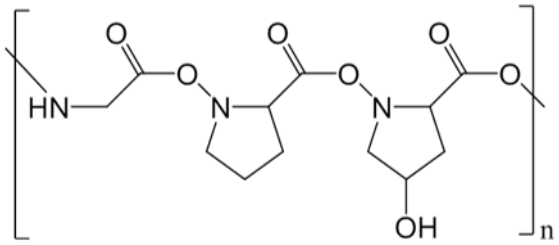

Figure 6.1: Cellulose molecule

6.2 Methods

The methods described in detail in section 3.3 were used to prepare the NCC suspensions (in water) from microcrystalline cellulose and methylcellulose powder. The samples are abbreviated NCX, where x refers to the NCC weight percentage relative to the weight of collagen (e.g. NC2 has a weight percentage 2% with respect to the weight of collagen). These suspensions were mixed manually with viscous collagen solutions (150 mg/mL) and the ammonia vapor neutralization method described in section 3.2 was used to induce fibril formation. Samples were also made with a collagen concentration of 5 mg/mL, but only tensile tests were performed to

quantify mechanical properties of these gels. SEM (section 3.13) was used to characterize collagen hydrogel microstructures. The chemical interactions between collagen and cellulose particles were characterized with FTIR spectroscopy (section 3.7), and the biocompatibility of NCC-collagen hydrogels was characterized using fluorescent microscopy to assess the viability of HFF cells seeded on the surface.

6.3 Results

6.3.1 Mechanical properties (5 mg/mL)

Prior to making high concentration gels, the mechanical properties of NCC-collagen hydrogels with 5 mg/mL collagen concentration were measured. There was not a significant increase in ultimate tensile strength when NCC was added to collagen, but the NC2 (2% NCC) showed an increase in elastic modulus (Figure 6.2). However, more experiments need to be performed to assess the statistical significance of these results.

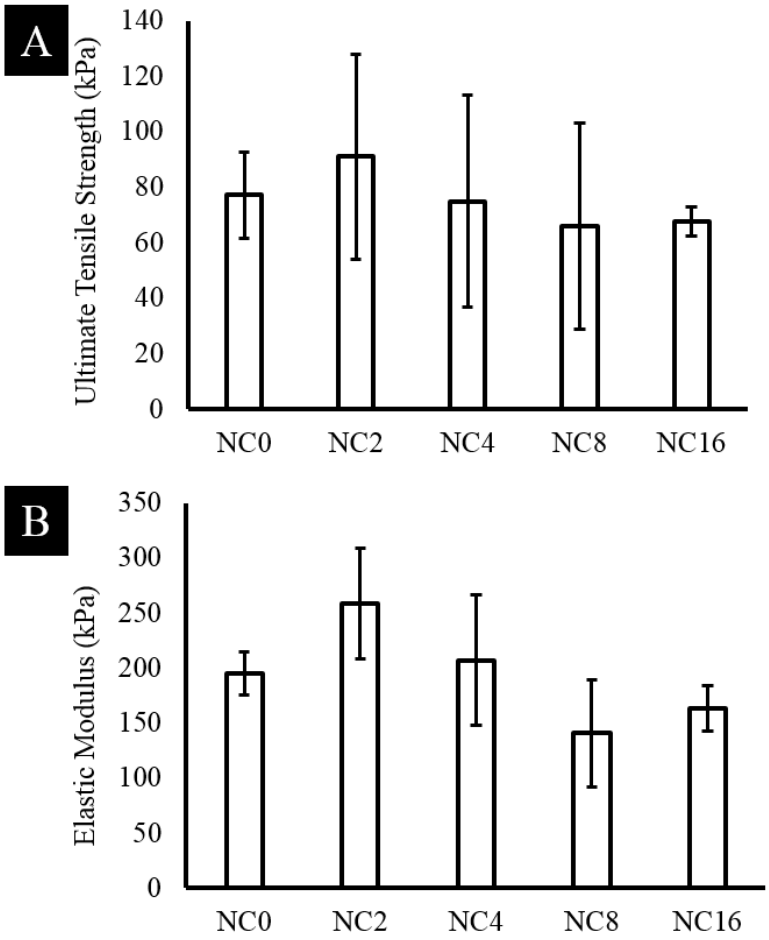

Figure 6.2: Mechanical properties of 5 mg/mL collagen hydrogels. (a) Ultimate tensile strength and (b) elastic modulus values for hydrogels of varying NCC composition. The error bars represent confidence interval (N > 4).

6.3.2 Microstructural characterization

SEM images in Figure 6.3 show collagen fibrils with unidirectional orientation and uniform diameters formed in the presence of NCC, while control hydrogels had less ordered fibrils that formed bundled structures. The control seemed to have some directionality, but this orientation was limited to length scales much smaller than a micrometer. Figure 6.3 shows a cross-section of an unaligned and an NC16 sample to show alignment occurs throughout the thickness of the sample. NCC particles ranging in size from 50-300 nm are pictured in Figure 6.3 (c-f). The larger particles are likely aggregated from smaller particles during the drying process, which has been observed in previous NCC suspension studies.

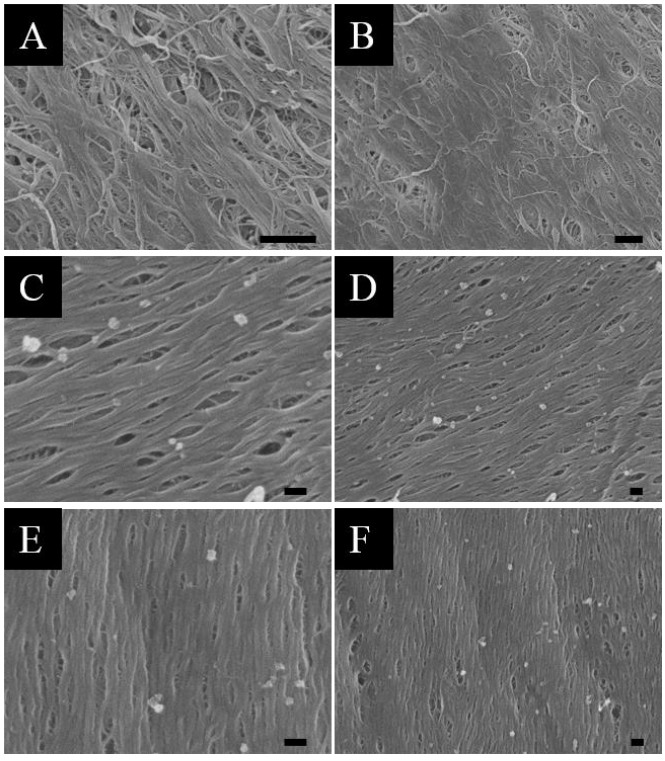

Figure 6.3: SEM micrographs of NC0 (a,b), NC2 (c,d), and NC16 (e,f) with collagen concentrations of 150 mg/mL. Collagen fibril alignment is obvious in samples containing NCC. ((a,b) scale bar length = 1 µm, (c-f), scale bar length = 100 nm).

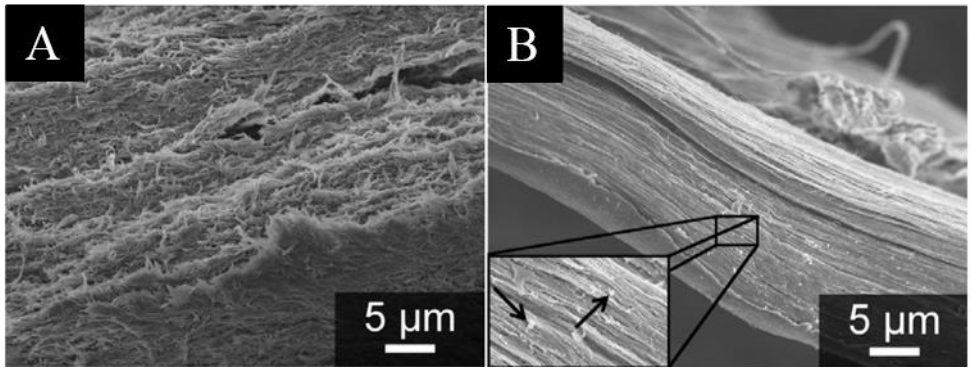

Figure 6.4: SEM micrograph of NC0 (a) and NC16 (b) cross-sections. The same structures observed in Figure 6.3 occur throughout the thickness of both unaligned and aligned hydrogels.

The fibril diameter and orientation distribution were quantified in ImageJ, and a histogram of these measurements is shown in Figure 6.5. The histogram showed that NC0, NC2, and NC16 samples had average fibril diameters of 52.4 ± 28.2 nm, 36.4 ± 7.9 nm, and 37.3 ± 10.2 nm respectively. The addition of NCC resulted in a reduction of fibril diameter and produced a narrow size distribution with an apparent preferred fibril orientation. There was one sharp peak in the angle distribution for both samples containing NCC, but not for the NC0 sample. The NC2 and NC16 had similar full-width half-maximum values for their angle distributions (15.4° and 16.7° respectively) and their fibril diameter distribution, which indicated that the additional loading of NCC from NC2 to NC16 did not result in any microstructural changes.

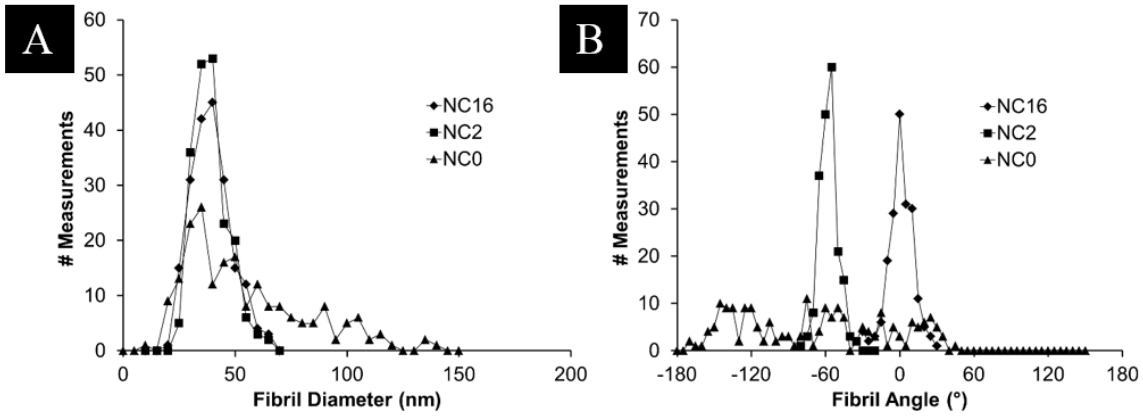

Figure 6.5: Histograms quantifying fibril diameter (a) and fibril orientation (b) of 150 mg/mL collagen hydrogels. The average fibril diameter appears to be equal for NC0, NC2, and NC16 samples, but the NC2 and NC16 samples display a unidirectional alignment and a lower degree of polydispersity when compared to the collagen control.

6.3.3 Spectral transmittance

The optical behavior of the hydrogels was quantified with a spectrophotometer. The NC2 sample displayed an increase in transmittance across the incident light spectrum range (300-800 nm), and the macroscopic difference between the NC2 and NC16 samples can be seen in the inset of Figure 6.6. The NC16 sample scattered more light than the control, which is likely due to the scattering contribution of the NCC particle aggregates.

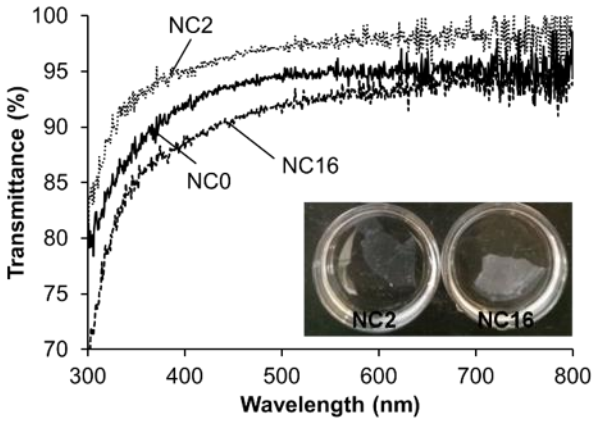

Figure 6.6: Spectral transmittance of NC0, NC2 and NC16 150 mg/mL collagen hydrogels. NC2 displays the highest transmittance across the entire wavelength spectrum. The transparency of the NC2 sample compared to the NC16 sample is shown in the inset.

6.3.4 NCC-collagen chemical interactions

In order to understand the mechanism of alignment induced due to the chemistry of the NCC particles, gels with methyl cellulose were made using the same procedure described above. NCC particles have a hydroxylated (and thus polar) surface, which is likely to act as energetically preferred site of adhesion for hydroxyl groups present on the collagen peptide surface. If this is the main interaction for alignment, methylcellulose particles that possess nonpolar methyl groups (as opposed to the hydroxylated surface of NCC) will not have the same regulating influence on the microstructure that was shown in the previous sections. Figure 6.7 shows that this hypothesis was correct for 2% methylcellose samples, which did not show any degree of fibril alignment.

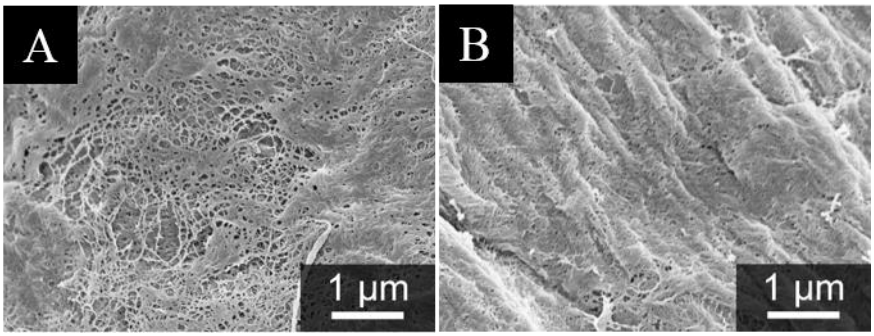

Figure 6.7: SEM micrographs of methyl-cellulose (2%) and collagen hydrogel (150 mg/mL). There is no apparent alignment of collagen fibrils, indicating hydrogen bonding between hydroxyl groups of NCC and collagen plays a significant role in alignment.

Figure 6.8 shows the FTIR spectrum of NCC particles, NC0, and NC16 samples. The 3200-3600 cm^{-1} range contains the peak associated with –OH stretching vibrations. The shape of the peak changes with different possible conformations and bonding environments. If there were no interactions between NCC and collagen, one would expect the NC16 spectra to be the weighted sum of the NC0 and NCC spectra. However, there was a distinct narrowing of the –OH peak, and a shift in the opposite direction (left on the spectra) of the NC0 and NCC peak locations. This indicates additional hydrogen bonding interactions were present between collagen and NCC.

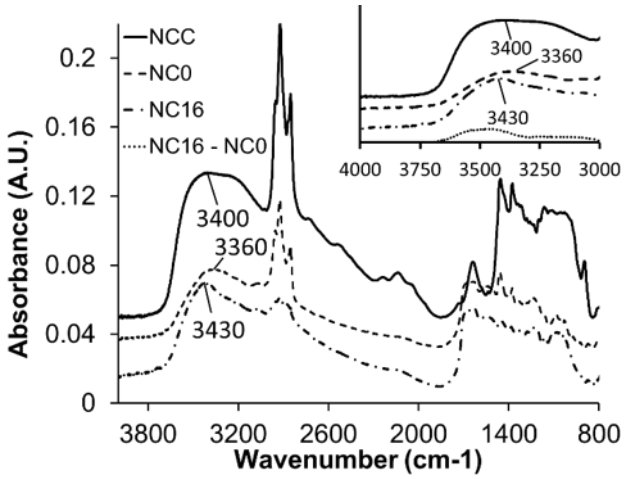

Figure 6.8: FTIR spectrum of NCC and NCC-Collagen gels

6.3.5 Biocompatibility

The fluorescence images in Figure 6.9 show HFF cells attached and began to spread out on the composite gel surface after 1 h of incubation. Greater than 99% of the cells attached were viable based on fluorescent staining. After 24 h, no dead cells were present, and the morphology of the cells became more typical of fibroblasts (elongated with pseudopodia extended over greater distances), indicating good attachment on the composite. By 72 h, the cells proliferated to form a more confluent layer of cells on the gel surface with no indication of detachment or cell death.

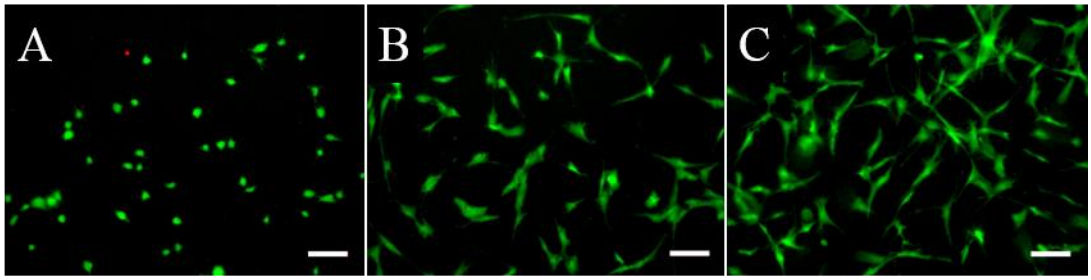

Figure 6.9: Biocompatibility test of NC2 hydrogels with 5 mg/mL collagen concentrations. Live (green) /dead (red) fluorescent imaging of HFF cells at 30 min (a), 24 h (b), and 72 h (c) after seeding. Cells were able to attach and proliferate to NCC-collagen hydrogels over a 72 h period. (Scale bar length = 10 µm).

6.4 Discussion

6.4.1 Microstructural properties, optical behavior, and biocompatibility

Unidirectional alignment of NCC-collagen composites was present in samples with nanocrystalline cellulose weight percentages of 2% and higher. The 2% composition was biocompatible as HFF cells were able to successfully attach and proliferate at the hydrogel surface. Histograms of alignment and fibril diameter were based on the SEM images in Figure 6.3. As suggested in Chapter 4, the optical behavior of samples with higher collagen concentrations was more sensitive to fibril diameter and dispersity of fibril diameters. Experimental results presented in this chapter showed that smaller fibril diameters with a narrower distribution resulted in more transparent gels. Therefore, the optical improvements may be due in part to smaller fibril diameters, narrower diameter distributions, as well as size and frequency of fibril intersections (nodes). SEM required the CPD of samples, which results in typical volume reductions of 20-30%[113]. Figure 6.3 showed inter-fibrillar intersections occurring almost every 100 nm, which was a result of small inter-fibrillar spaces and the CPD shrinkage.

Similar to Chapter 5, further microstructural characterization that does not require CPD (TEM, CRM) should be performed to estimate the Fourier components of spatial density fluctuations.

The scattering contributions from NCC particles needs to be considered when analyzing spectral transmittance results (Figure 6.6), especially at higher weight percentages. The NCC particles appeared to form large aggregates, which increase the amount of light scattering from the cellulose phase. When this phenomenon is considered, the NCC-collagen composite preparation should limit NCC aggregation, and NCC suspensions should be used immediately after ultrasonication. Additionally, weight percentages below 2% should be investigated to find the minimum percentage of NCC required for alignment in order to maximize spectral light transmittance. It is interesting to note that Chapter 4 showed surface alignment in a 100 mg/mL hydrogel that was in contact with a cellulose dialysis membrane during fibril formation. NCC could be used as a nano-templated surface to eliminate mixing of particles within the bulk of the gel, eliminating extra scattering events due to NCC aggregation. An effective length scale for this template alignment would need to be established. NCC nano-templating could be adapted and used with 3D printing (layer by layer) methods to manufacture aligned collagen hydrogels.

6.4.2 Mechanism of collagen alignment

For the same weight percentage and methodology, methylcellulose did not reproduce a similar aligned microstructure or improved spectral transmittance when compared to NCC samples. The only difference between NCC and methylcellulose is their surface chemistry: methylcellulose moieties are methylated (nonpolar) while NCC moieties are non-methylated (polar). According to Greminger and Savage, the geometry and structure of methylcellulose is the same as hydroxylated cellulose in aqueous conditions[179]. Considering this and the FTIR results from section 6.3.4, the collagen fibril alignment seems to be dependent on the hydrogen

bonding between hydroxyl groups of the collagen amino acid side chains and the hydroxyl groups on the NCC surface. This interaction may have occurred prior to the ammonia vapor exposure.

More experiments need to be performed to gain further understanding of the property dependence of this mechanism. For instance, this method reduced MCC to NCC using ultrasonication to break micrometer sized particles (~20 μm) into smaller particles. However, the distribution of particle sizes was not controlled, making it unclear whether alignment is dependent on size. For future experiments, other methods of reducing MCC to NCC should be explored. For example, a sulfuric acid hydrolysis method has been used to produce rods with diameters as small as 10 nm and aspect ratios on the order of 100[169]. Preliminary work has already been performed to produce these rod shaped particles, but lateral aggregation of particles during dehydration makes it difficult to obtain true particle dimensions (Figure 6.10).

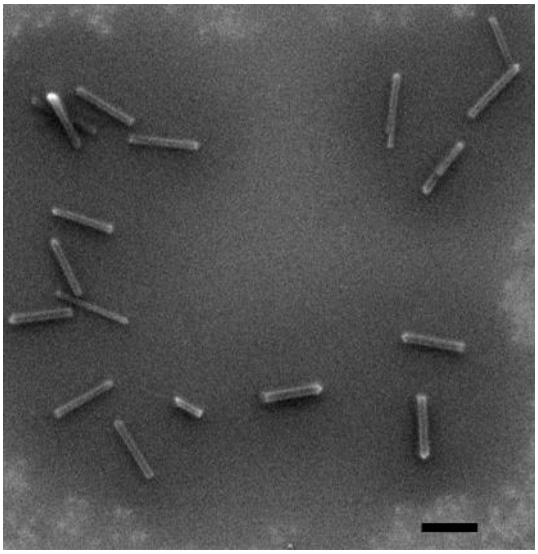

Figure 6.10: SEM images of NCC rods after sulfuric acid hydrolysis of MCC. (scale bar length equals 1 μm)

Elazzouzi-Hafraoui et al. quantified particle sizes of NCC by embedding NCC in ice and performing cryo-TEM[178], while other groups have freeze-dried suspensions to reduce particle aggregation[172,173,176]. Once a sample preparation technique is established, a thorough study should be performed to find the optically optimal concentrations and sizes of NCC particles for alignment and diameter regulation.

Additionally, acid hydrolysis in conjunction with centrifugation washing increases the degree of crystallinity of the NCC suspension[172], where NCC particles from the ultrasonication method used in this work maintain the same amount of amorphous cellulose that is present in MCC. The effect crystallinity has on the alignment mechanism can be investigated with this acid hydrolysis method.

6.5 Conclusion

This chapter introduced a new methodology capable of aligning highly concentrated collagen hydrogels and results in an improved spectral transmittance curve. As mentioned in the discussion, future work is required to further the understanding of the mechanism of alignment, which proposes that the process is dominated by hydrogen bonding between NCC and collagen molecules. Methods that produce different sizes, geometries, and crystallinity of NCC particles should be used to make optical improvements additional to those presented in this work. Finally, using NCC as a nano-templated surface for collagen fibril alignment could be used in conjunction with 3D printing.

Chapter 7

Silica-collagen nanocomposite via copolymerization method

7.1 Introduction

This chapter describes the synthesis and characterization of silica-collagen constructs made using a simple copolymerization process. It was hypothesized that silica can be used to improve the mechanical properties of collagen hydrogels without sacrificing biocompatibility and optical function required for cornea replacement.

Current artificial corneas (keratoprostheses) available for clinical use do not truly bio-integrate with surrounding tissues, nor do they allow for epithelialization of their surface, which can result in complications[9,10]. As a result, there is significant effort being directed towards the development of biocompatible corneal substitutes that support tissue regeneration[11]. Regeneration of the cornea requires materials that can mimic the optical and mechanical properties of the native cornea, and that can be easily stored for use as needed, effectively eliminating the need for human donor tissue. Type I collagen-based structures have shown potential in meeting these design requirements and have increased biomechanical strength due to chemical cross-linking[180–183]. Cross-linked collagen constructs have been used for tissue regeneration, and have been piloted in human trials *in vivo* with moderate success[11,184,185].

As an alternative to cross-linked collagen constructs, here we investigated different compositions of silica-collagen bio-hybrid materials, which are known to exhibit favorable optical and mechanical properties for corneal replacement[15,186]. Silica-collagen hydrogels have also been successful in hosting various fibroblast cell types[16,187]. In this study, silica precursor 3-aminopropyltriethoxsilane (APTES) and soluble type I bovine collagen were combined to create a

hybrid material. We determined the mechanical and optical properties for two different silica-compositions in hydrogel and xerogel states, and developed a manufacturing process to construct implants with appropriate size and geometry for corneal applications. We report the microstructure, biomechanical, and optical properties of these implants, as well as initial biocompatibility studies in a cultured rabbit cornea model.

7.2 Methods

The silica-collagen composites were made according to the methodology in section 3.5. Two different silica-collagen compositions (3:1 and 9:1) were synthesized. These ratios describe the weight ratio of silica precursor to collagen. Additionally, two different hydration states were characterized are referred to as hydrogels and xerogels. Hydrogels were samples that remained hydrated throughout synthesis and characterization. Xerogels were defined as constructs that were dehydrated and rehydrated with PBS. Microstructural characterization was performed using standard SEM prep and the imaging procedure described in section 3.13. Suture pullout tests were performed on a limited number of samples, but most composites were too fragile for this method of mechanical characterization. Therefore, relaxed moduli and UTS were quantified with uniaxial tensile testing (section 3.8). The spectral light transmittance of each sample was measured using a spectrophotometer, and the index of refraction of composites was measured using an Abbe refractometer (section 3.9).

Dr. Sanjay Patel at the Mayo Clinic in Rochester, MN performed all ex-vivo biocompatibility experiments. Multiple 3:1 hydrogel lenses were prepared in a sterile environment and placed in circular lamellar pockets made on the anterior surface of explant rabbit corneas. Figure 7.1 shows the tissue culture apparatus used. The epithelial layer formed over the

implant was characterized using fluorescent staining and TEM protocols described in section 3.11.

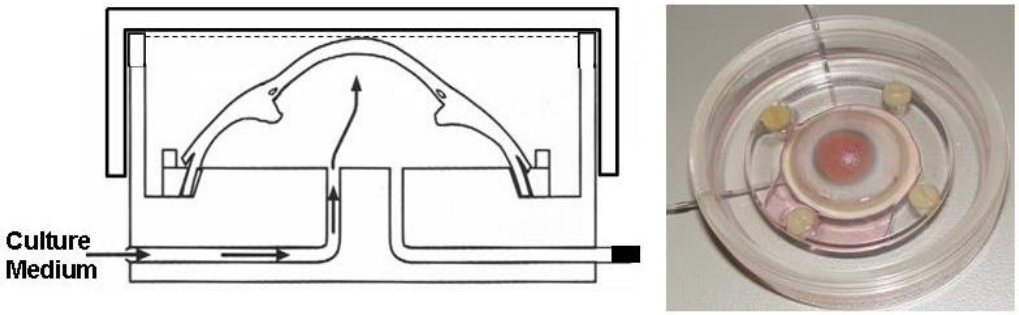

Figure 7.1: Anterior segment organ culture system. Left: Schematic, and Right: photograph of modified Petri dish with mounted anterior segment. Culture medium can be perfused into the artificial anterior chamber for medium exchange, and medium was filled external to the anterior segment to just cover the vertex of the cornea (dashed line).

7.3 Results

7.3.1 Microstructural characterization

Cross-sectional SEM showed that 3:1 and 9:1 compositions in both the hydrogel and xerogel state consisted of a network of evenly sized fibrils (Figure 7.2(a)). Nonfibrillar structures observed in the fibrillar network (Figure 7.2(b)) were assumed to be silica aggregates. A denser structure was seen at the surface, with some thicker fibrils (Figure 7.2(c)); however, on closer examination (Figure 7.2(d)) these fibrils appeared to consist of several smaller, intertwined fibers. It should be noted that the structures observed have been reduced in size by 20-30% due to ethanol dehydration and the critical point drying procedure[113]. However, this shrinkage is typically uniform throughout the sample and does not result in collapse as air-drying does.

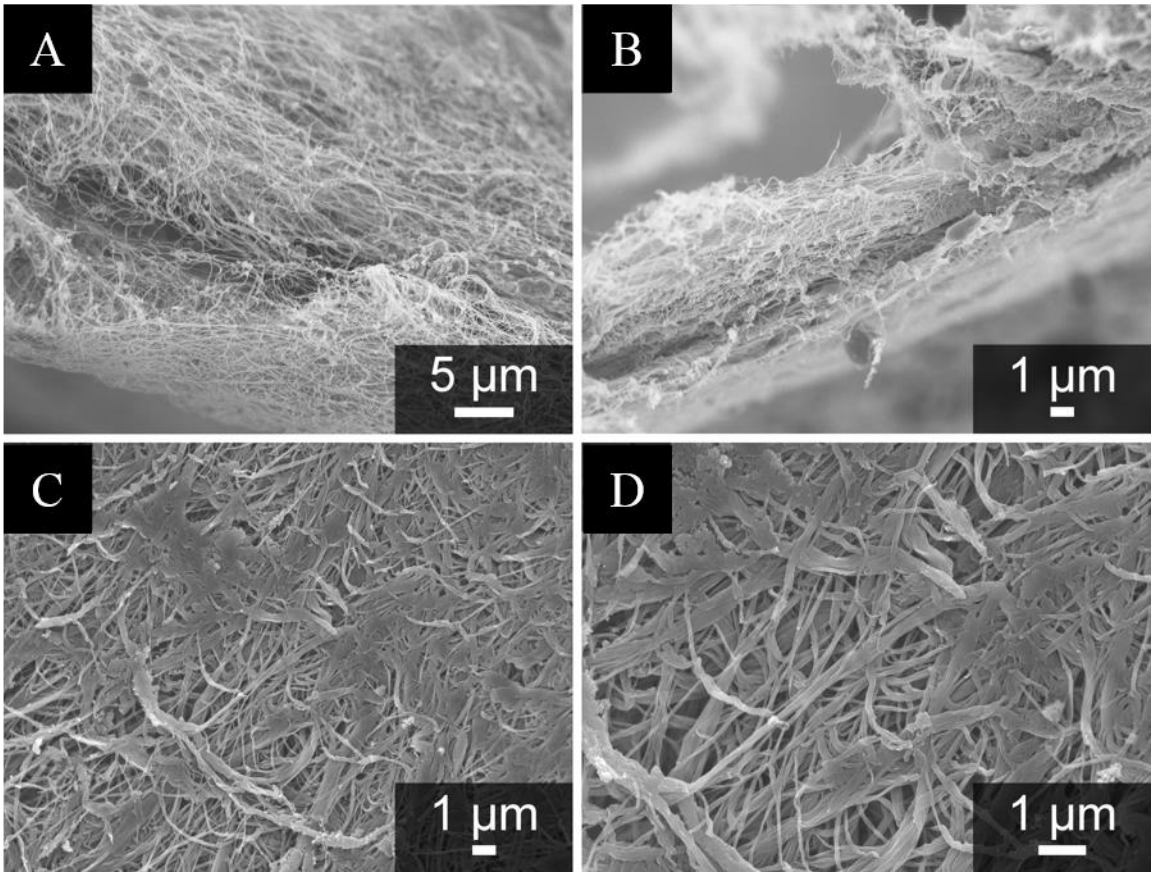

Figure 7.2: Cross-sectional SEM of a 9:1 hydrogel at lower magnification (a) and higher magnification (b). The lower magnification shows a fibrillar network of consistently sized fibrils. The higher magnification shows the same fibrillar microstructure as well as aggregates (arrow) formed on the surface of the sample. Surface SEM of the same hydrogel at lower magnification (c) and higher magnification (d) reveals a denser structure with thicker fibrils. At the higher magnification it becomes clear that these larger structures actually consist of several intertwined smaller fibrils.

7.3.2 Mechanical properties

Uniaxial tensile tests were performed on hydrogel and xerogel samples. Results of these studies are presented in Table 7.1 and illustrated with bar graphs in Figures 7.3 and 7.4.

Silica-collagen hydrogel and xerogel samples all had significantly higher relaxed moduli when compared to pure collagen xerogel samples. There was not a statistical difference in tensile properties between 3:1 and 9:1 compositions. However, xerogel composites experienced an order of magnitude increase in mechanical properties compared to the hydrogel state. The 9:1 xerogel composites were aged for 2 and 4 weeks. The relaxed modulus doubled in value for samples that underwent 2 weeks of aging. After 4 weeks, the relaxed modulus began to decrease but remained higher than unaged samples.

Table 7.1: Relaxed modulus and UTS values for different silica compositions, hydration states (H = hydrogel, X = xerogel), and aging times (2W = 2 weeks).

Sample	Rel. Mod. (Mpa)	UTS (Mpa)
Collagen X	0.07 ± 0.06	0.11 ± 0.07
9:1 H	0.16 ± 0.02	0.06 ± 0.01
3:1 X	2.51 ± 0.55	1.74 ± 0.72
9:1 X	2.33 ± 0.51	1.34 ± 0.76
9:1 X, 2W	4.94 ± 0.79	1.7 ± 0.37
9:1 X, 4W	3.62 ± 0.56	1.26 ± 0.39

The hydrogel samples and the 9:1 xerogels were too fragile for suture pullout tests. However, an example of a rupture strength-displacement curve for 3:1 xerogel specimens is shown in Figure 7.5. The material displayed strain-hardening behavior prior to failure, and proceeded to rupture in a ductile manner. The rupture strength of the 3:1 xerogels was 0.161 ± 0.073 N/mm.

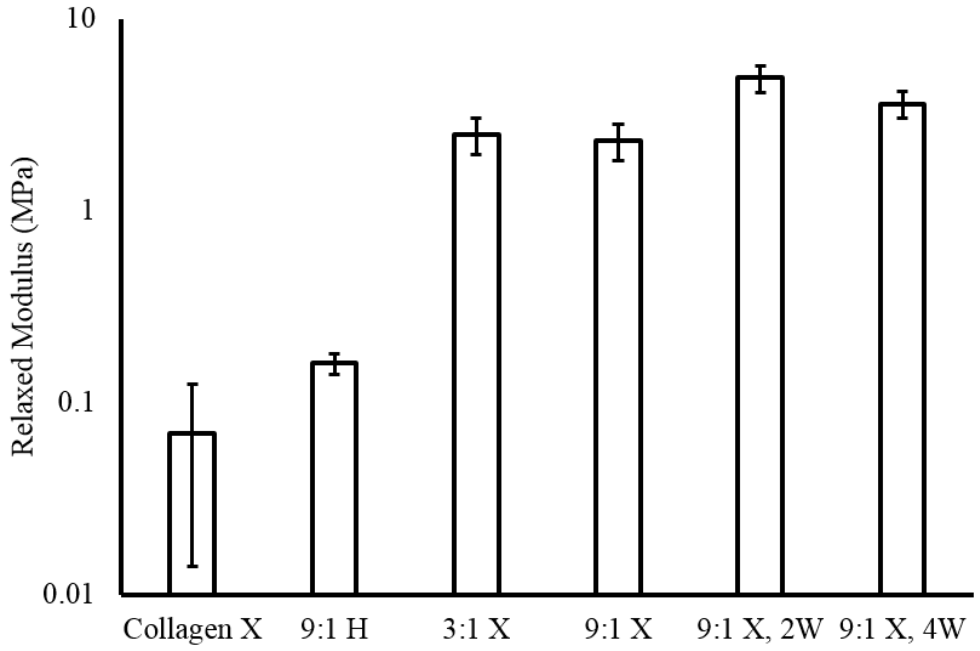

Figure 7.3: Relaxed modulus bar graph (log scale) with associated confidence intervals.

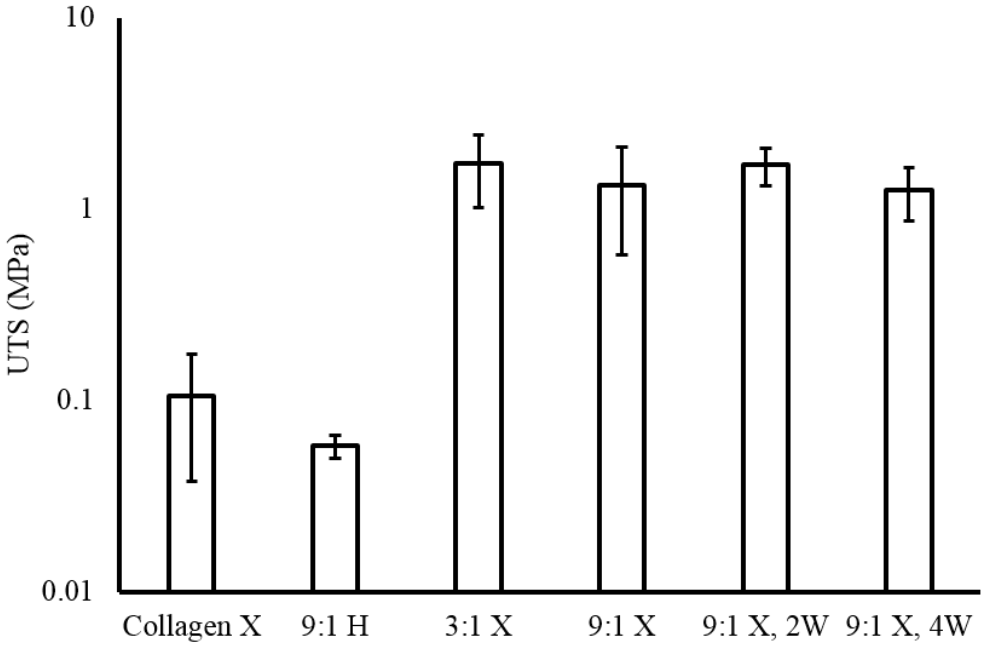

Figure 7.4: UTS bar graph (log scale) with associated confidence intervals.

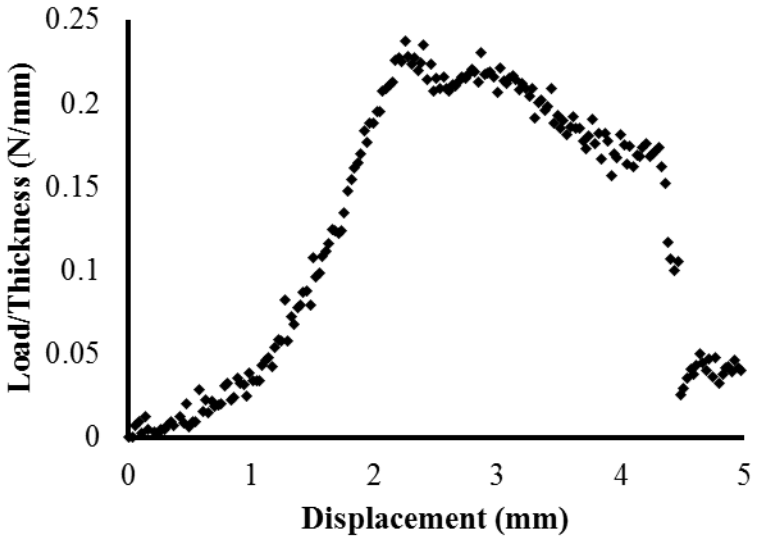

Figure 7.5: Force-displacement curve for a 3:1 xerogel from a suture pullout test. The material displayed strain-hardening behavior in the initial part of the curve followed by a linear region. The material then failed and continued to rip until complete fracture.

7.3.3 Optical properties

Transmittance increased as wavelength increased from the ultraviolet to the infrared for both compositions and hydration states. In general, hydrogels had a higher transmittance than xerogels (Figure 7.6, top), and lower silica compositions had higher transmittance. The transmittance spectra for all compositions and hydration states are shown in Figure 7.6 (bottom, $n > 30$). The transmittance of the rabbit cornea was from data published by McLaren and Brubaker[188].

The refractive index was 1.334 and 1.332 for the 9:1 and 3:1 compositions respectively. Creation of a xerogel increased the index of refraction of both compositions to 1.403 and 1.389, respectively.

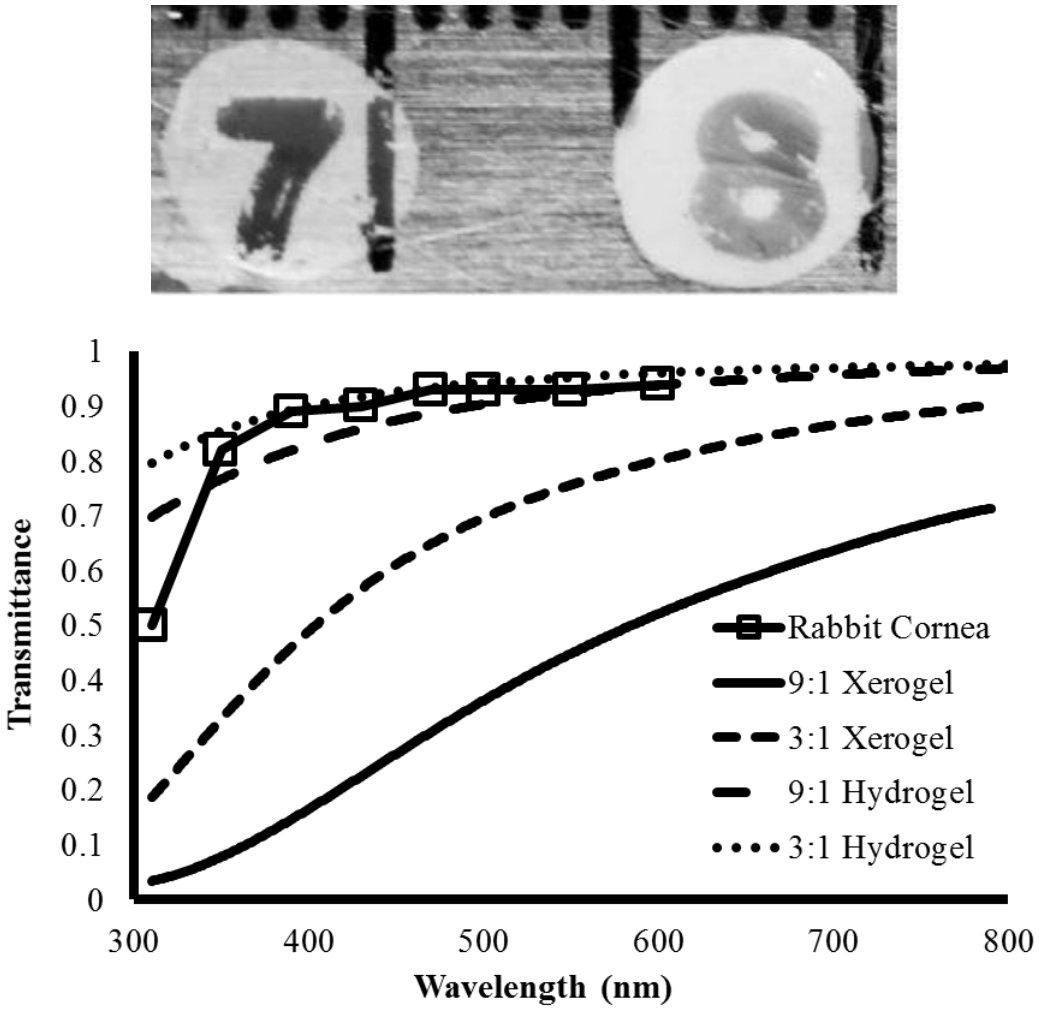

Figure 7.6: Optical characterization of the hybrid material. Light transmission curves in the visible range for 3:1 and 9:1 compositions in the hydrogel and xerogel states. The rabbit cornea curve was taken from data tabulated by McLaren and Brubaker[188]*. All hybrid curves were adjusted to a common thickness of 0.3 mm.*

7.3.4 *Ex Vivo* biocompatibility

Eight rabbit corneas underwent surgery to implant a hybrid construct, and two control corneas underwent surgery without implantation. In all corneas, epithelial defects immediately after surgery were approximately 5 to 6 mm at the widest diameter (Figure 7.7). In the two

control corneas, complete re-epithelialization of the exposed bare stroma took 8 and 15 days. In experimental corneas, two corneas became contaminated during the culture period and were excluded from analysis; this contamination was unrelated to sterility of the implants. In the remaining six implanted corneas, complete re-epithelialization of the exposed implant took 5.5 ± 2.4 days (range 3–10 days; Figure 7.7, Table 7.2).

Epithelialization of the implant surface was confirmed by light microscopy in all cases (Figure 7.8). An early stratified epithelium was noted with longer culture duration, but there was no evidence of stromal cell migration into the implants at the end of the culture period (Figure 7.9). Regenerated epithelium stained positive for keratin AE1/AE3 in all cases (Figure 7.9, Table 7.2). There was no evidence of epithelial basement membrane deposition over the hybrid surface when samples were analyzed using TEM, although the basal epithelial cell membrane was intimately associated with the hybrid surface (Figure 7.10).

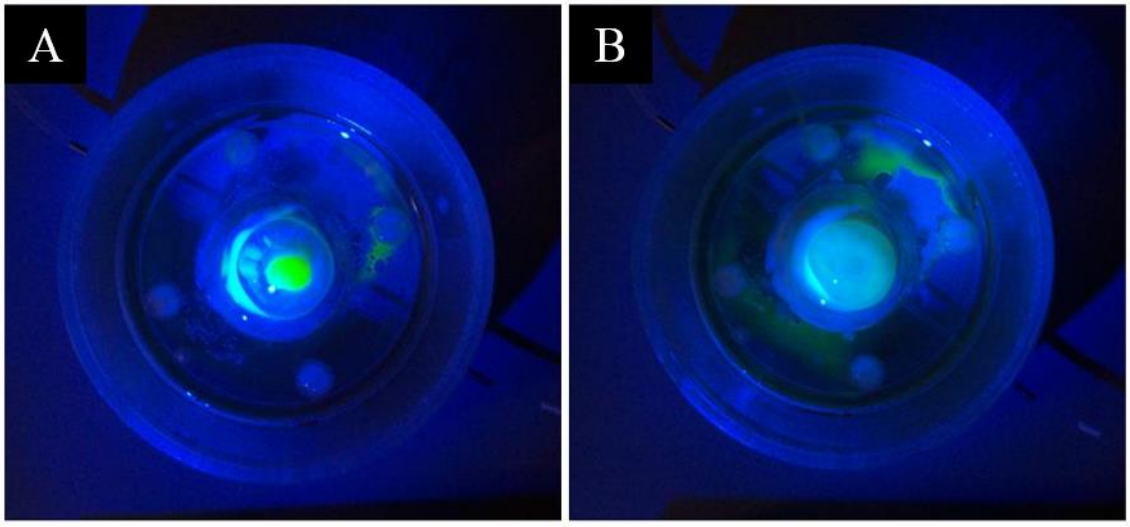

Figure 7.7: Assessment of closure of corneal epithelial defect. Left: The epithelial defect created by central lamellar keratectomy stained with sodium fluorescein. The size of the epithelial defect

was observed daily until closure. Right: The same cornea after closure of the epithelial defect, devoid of central staining.

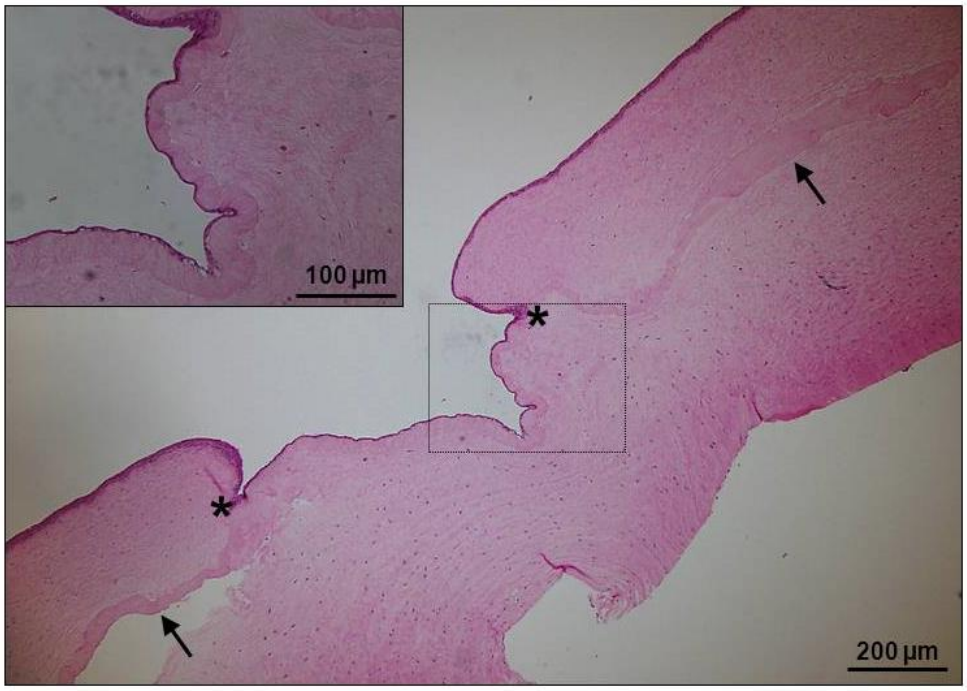

Figure 7.8: Light microscopy images of implanted rabbit cornea stained with Hematoxylin and eosin. The peripheral implant (arrows) was enveloped in a paracentral lamellar pocket of rabbit stroma, and the center of the implant was exposed in the region of the anterior lamellar keratectomy (denoted by asterisks). A thin layer of epithelium covered the implant and was continuous with the epithelium at the edge of the keratectomy. Epithelial closure occurred after 5 days, and culture was maintained after closure for an additional 5 days. Inset, Higher magnification image of the area denoted by the box showing an intact thin layer of epithelium covering a thin implant. Vacuolization of basal cells was noted over the surface of the implant, but similar changes were also noted in the peripheral native cornea where the epithelium had not been disrupted. Thus, vacuolization was most likely a manifestation of cellular changes due to organ culture.

Table 7.2: Results of ex vivo organ culture studies.

	Epithelial Defect			Histological Analysis		
	Size (mm)	Time to Closure (Days)	Time in Organ Culture (Days)	Number of Layers of Epithelial Cells (Mean (Range))	Keratin AE1/AE3 Staining	Collagen IV Staining
Implanted Corneas						
1	5.5 x 4	6	9	1 (1-2)	+	-
2	5 x 4	5	10	2 (1-3)	+	-
3	5 x 5	10	10	1 (1-2)	+	-
4	5 x 5	5	7	3 (1-5)	+	-
5	5 x 5	3	7	3 (2-6)	+	-
6	5 x 6	4	7	5 (4-8)	+	-
Controls						
1	7 x 7	15	17	3 (1-5)	+	-
2	5 x 5	8	10	2 (1-4)	+	-

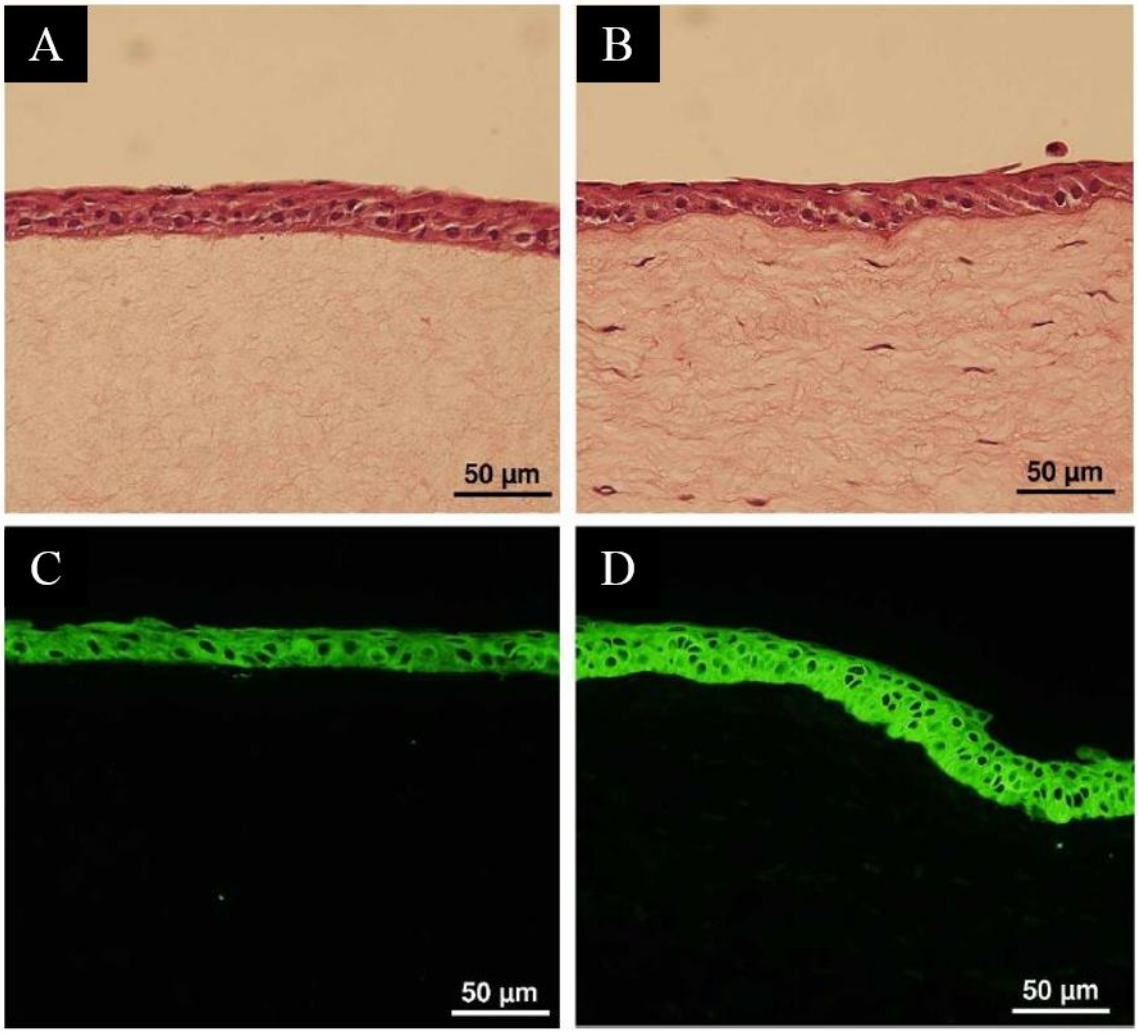

Figure 7.9: (a,c) Stratified rabbit corneal epithelium attached to the acellular and amorphous implant. This section was located at the center of the exposed stromal implant within the lamellar keratectomy. Epithelial closure occurred after 4 days, and culture was maintained after closure for an additional 3 days. (b,d) Normal rabbit anterior cornea with stratified epithelium attached to cellular stroma. (a,b) Hematoxylin and Eosin staining. (c,d) Positive staining with keratin AE1/AE3 indicates the regenerated cell layer has an epithelial phenotype separate from the acellular implant.

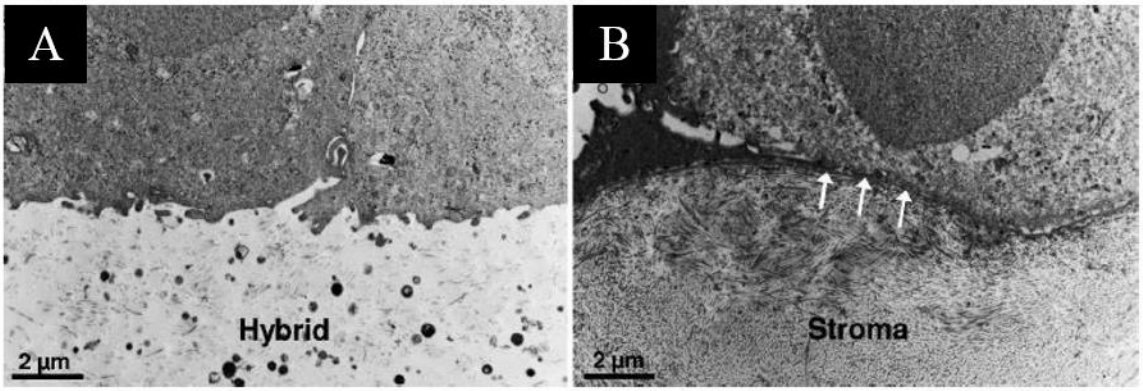

Figure 7.10: Transmission electron microscopy of the basal epithelium. (a) The basal epithelial cell membrane was intimately associated with the surface of the hybrid material, although basement membrane was not visible. (b) *Normal rabbit basal epithelium with basement membrane (*arrows*) between the basal epithelial cell and the fibrillar stroma.*

7.4 Discussion

7.4.1 Material properties of hybrid

Qualitatively, the hybrid materials fabricated using the given manufacturing method were ductile and relatively easy to handle when compared to pure collagen gels made from soluble collagen of the same concentration. SEM images displayed the hybrid's fibrillar morphology. The absence of D-banding indicated that the collagen fibrils were coated with silica particles. Ono et al.[21] displayed this assumed microstructure with similar fibril diameters for TEOS-collagen hybrids, where TEM images showed contrast between the silica coating and collagen fibril center. Additional studies are necessary to quantify important microstructural properties such as fibril diameter, spacing, and orientation of silica-collagen hybrids as these properties are critical for high optical quality in the native cornea.

The hydrogels had higher transmittance than the native cornea but were too weak to be sutured without fracture. The relaxed modulus and UTS of the 3:1 and 9:1 xerogels were similar.

The 9:1 xerogel composition had a relaxed modulus of 2.33 MPa, which increased to 4.94 after 2 weeks of aging in an aqueous environment at ambient temperature. The modulus value was taken over the strain range of 8-12%. Values in the 2-3 MPa range have been reported for the cornea for slow strain rates (Table 2.1). Therefore, the xerogel samples are comparable to the native cornea. The increase in strength and stiffness from the hydro- to xerogel state was likely due to the higher concentration of collagen in the xerogels. Even after rehydration, the xerogel volume decreased by approximately 90% with respect to the original hydrogel volume.

The 3:1 composition was stronger and more transparent than the higher silica composition. The silica aggregates in the 9:1 composition are indicative of structural heterogeneities, which may account for the differences in biomechanical and optical properties observed in these samples. Some of the 9:1 xerogel samples were strong enough to withstand suture placement, but failed while being loaded into the tensile test apparatus. The 3:1 rehydrated xerogels had a 0.161 ± 0.073 N/mm rupture strength. Liu et al.[65] reported suture strengths in the range of approximately 0.07 to 0.40 N/mm for collagen hydrogels cross-linked with carbodiimide. The human cornea has a rupture strength that exceeds the tensile strength of the nylon sutures used; that is, the sutures fail before the cornea ruptures in suture tests of the native cornea. Menovksy et al.[189] reported a tensile strength of 0.35 ± 0.02 N for 10-0 nylon sutures. This indicates that the suture strength of human cornea is significantly higher than silica–collagen hybrids. Additionally, UTS values of xerogel samples did not exceed 2 MPa, while multiple groups have reported UTS values for the cornea greater than 10 MPa (Table 2.1).

The indices of refraction for hydrogel samples were both approximately the same as that of water. After samples were dehydrated, the refractive indices increased for both silica compositions. This was to be expected because the index of refraction of silica without water is approximately 1.45[190]. Additionally, samples with higher silica content yielded higher indices of refraction closer to that of silica when compared to samples with lower silica content.

The epithelium of the human cornea has a refractive index of approximately 1.40, and the refractive index of the stroma ranges from 1.37 to 1.38[191]. The 3:1 and 9:1 xerogels had refractive indices of 1.389 and 1.403, respectively, which fall close to the human cornea indices. The small difference between the 3:1 sample and that of the human stroma could be eliminated by minor adjustments in silica content.

The transmittance characteristics of these hybrid materials have a distinct advantage over many other materials that have been investigated (Fig. 4). The 3:1 xerogel mimics native cornea closely in both the visible and UV spectrum[39]. The 3:1 hydrogel has transmittance in the visible spectrum that is similar to that of rabbit cornea in vivo[40,188], although transmittance does not drop as quickly at wavelengths below 350 nm as it does in the living cornea. The high transmittance to 400 nm is consistent with measurements in human corneas where the corneas were not removed from the globe and were minimally disturbed[188]. Parameters such as pH, silica:collagen composition, synthesis and manufacturing methodology, collagen concentration, and hydration state are currently being investigated in more detail to optimize the mechanical and optical properties of these hybrid gels. The relationship between optical properties, strength, and initial collagen concentration should be carefully investigated. Dehydration of the gels led to improved mechanical properties, but this dehydration also resulted in a decreased transmittance. An increase in initial collagen concentration could result in a denser fibril network, yielding a transparent hydrogel with similar mechanical properties to the xerogels presented in this paper. Also, higher concentrations of collagen have been shown to assemble into highly organized fibrils[192] which could potentially decrease light scattering.

7.4.2 Biocompatibility

For the initial biocompatibility studies, our goal was to show that corneal epithelium regenerates and covers the surface of the implant. Without a continuous epithelial covering and cellular attachment, the implant would be prone to degradation and infection *in vivo*. With our organ culture method and a surgical technique established by Evans et al.[106], we found that the implanted bio-hybrid consistently supported complete re-epithelialization within an average of 1 week. While the control corneas in this study took longer to re-epithelialize, they were anatomically different from the experimental corneas with a significant discontinuity at the edge of the 200-μm-deep keratectomy; we would have expected a simple epithelial defect to close within 3 days if we had not performed a keratectomy. Using immunohistochemistry, we confirmed the epithelial phenotype with keratin AE1/AE3 staining, but were unable to detect visible basement membrane formation using TEM. The lack of visible basement membrane may be explained by the short culture time after closure of the epithelial defect[106], and longer-term studies *in vivo* will be required to convincingly confirm cell attachment and formation of focal adhesion complexes. Epithelialization of any artificial corneal material is critical to its success because the material is more likely to be retained. Fagerholm et al.[11] showed that slow epithelialization of a cross-linked collagen hydrogel implanted into human corneas resulted in initial thinning of the corneas. While these initial results are encouraging and represent a biocompatibility advantage compared to current plastic keratoprostheses, which do not support epithelium, further studies are needed to determine epithelial outcomes *in vivo*.

With initial favorable characteristics of the silica–collagen bio-hybrid, *in vivo* studies are planned to assess biocompatibility for a longer duration post implantation. These studies will enable assessment of corneal cellular changes[193], transparency and backscatter[134,188], and oxygen transmissibility[194]. Although the initial implants did not require suturing to the recipient cornea,

based on the suture pullout tests, an overlay suturing technique will be required in vivo, similar to that used by Fagerholm et al.[11]

7.5 Conclusion

In this chapter, a copolymerization process was used to synthesize silica-collagen composites. Gels with different silica compositions and hydration treatments were characterized and compared to the cornea. Mechanical properties of the gels were improved upon silica addition, and the relaxed modulus continued to increase when samples were aged in aqueous conditions for 2 weeks. Xerogel composites had stiffness values similar to the cornea, but did not possess the same transparent behavior. The silica-collagen composites showed good *ex vivo* biocompatibility by allowing for re-epithelialization, which is important for preventing infection and regulating the hydration of the cornea. Therefore, xerogel silica-collagen composites may have potential use for partial thickness implantation, but a full-thickness implant using this material would be too hazy.

In future work, higher collagen concentrations should be used in order to improve the mechanical properties of the gel without increasing light scattering associated with xerogels. Due to the viscous nature of collagen solutions close in concentration to the cornea, a copolymerization of silica and collagen will be difficult to fabricate due to the required mixing step which introduces bubbles to the construct. A two-step process is introduced in Chapter 8, which allows for the collagen network and silica deposition to be controlled in separate steps.

Chapter 8

Silica-collagen nanocomposite via Stöber method

8.1 Introduction

While Chapter 7 showed mechanical properties of collagen hydrogels can be improved with silica addition, the improvement was either not a significant enough increase to match corneal mechanical properties or was accompanied by a decrease in optical properties. This chapter describes a two-step process utilizing the methods from Chapters 4-6 to produce highly concentrated collagen gels with improved mechanical and optical properties, followed by a controlled silica deposition resulting in gels with improved degradation resistance and mechanical behavior.

Highly concentrated collagen hydrogels (>50 mg/mL) made *in vitro* approach the optical and mechanical behavior of the cornea, but degrade rapidly in physiological conditions[46]. Sol-gel chemistry has been used to prepare silica-collagen hydrogels with improved mechanical properties[18]. Silica gels derived from the sol gel process have also been shown to exhibit controllable biodegradation behavior[24,25]. Previous chapters describe published work on silica-collagen xerogel and hydrogel materials[195]. These materials were able to withstand implantation on explanted rabbit corneas and allowed for re-epithelialization, which is important for integration with native tissue[10,56].

In similar studies, researchers have primarily used copolymerization methodology to synthesize silica-collagen hydrogels[15,18,186,196]. However, this involves mixing silica sol and collagen in their liquid states, which is problematic with collagen solutions that are highly concentrated and therefore more viscous. This work proposes a two-step process in which a collagen hydrogel is first formed followed by second silica deposition onto the previously formed

collagen fibrils. In order to strengthen the network with silica without reducing light transmission, a controlled sol gel process was developed that limits silica condensation to a smooth uniform coating around the collagen fibrils. This chapter also characterizes the microstructures produced by this new method of silica-collagen hydrogel synthesis. Macroscopic biomechanical and optical characteristics of the nanocomposite material are also reported. Additionally, the effects of different aging conditions on chemical bonding of the silica network are characterized and the degradation of the material in the presence of collagenase is quantified. This novel method of constructing silica-collagen nanocomposites permits modulation of the biomechanical, optical and degradation properties of biocompatible gels and therefore represents an important candidate material for corneal replacement.

8.2 Methods

A two-step process was used to make hydrogels of varying collagen concentration and silica content by first forming concentrated collagen hydrogels and subsequently performing a controlled silica deposition (Figure 8.1). Briefly, collagen hydrogels were made using the methods described in section 3.2. The hydrogels were then soaked in PLL to give collagen fibril surfaces a positive charge. These cationic samples were soaked either in a Ludox suspension or Stöber solution. In both cases, the samples were kept in their initial solution for one day, and then placed in a fresh Stöber solution. After silica deposition, different aging densification steps were performed. These included soaking in an alkaline ethanol solution, soaking in a TEOS/ethanol solution, and exposing to UV light. All of these methods are described in detail in section 3.6.

The microstructure of these gels was characterized using SEM procedures described in section 3.13. Raman spectroscopy (section 3.7) was used to characterize the chemical structure

of the silica network formed around the collagen fibrils. Methods from sections 3.8 and 3.9 were used to quantify the relaxed modulus and spectral light transmittance of the hydrogels, respectively. Degradation resistance of hydrogels was characterized using a collagenase degradation procedure described in section 3.12. In order to characterize the hydrogels at different points throughout the deposition process, Table 8.1 contains abbreviations that were used to describe samples in the following sections.

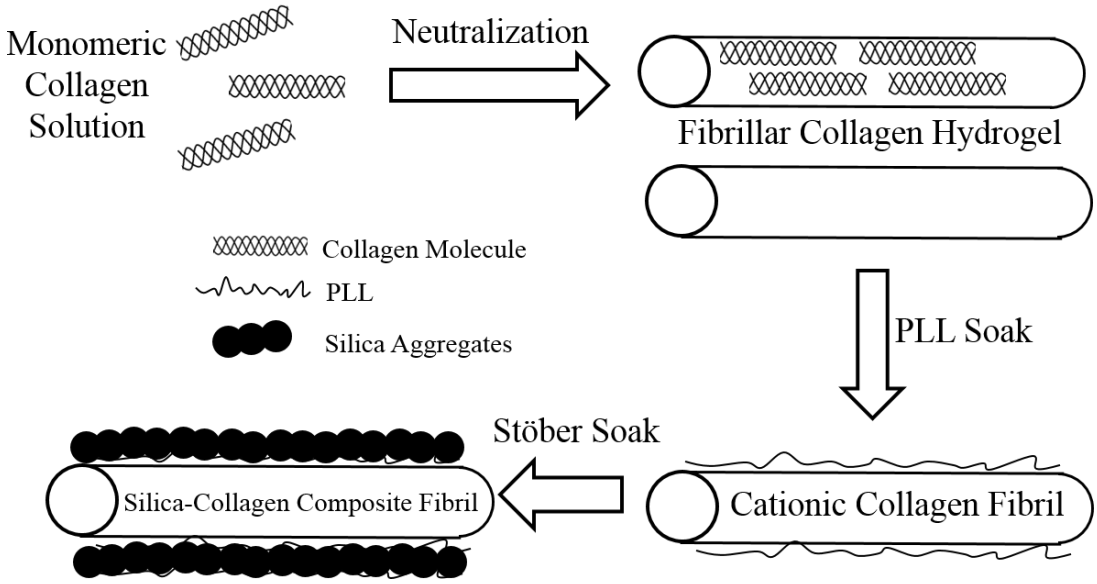

Figure 8.1: Diagram of two-step silica deposition process

Table 8.1: Sample labels used in the following sections that correspond to the final step of each hydrogel treatment.

Sample Label	*Sample Description*
Control	**Collagen Hydrogel**
+PLL	After PLL addition
+TEOS	After 5 day Stöber soak
	After 1 day NH_4OH/Ethanol soak
TAn	After n day TEOS/Ethanol soak
TAn-UVm	After m hour UV exposure

8.3 Results

8.3.1 Microstructure

A dilute collagen concentration of 5 mg/mL was used to show the influence of PLL on the formation of a nanocomposite (silica/collagen) gel. Figure 8.2(c) illustrates that in the absence of PLL surface modification, silica formed large (> 1 μm) aggregrates, leaving the majority of collagen fibril surfaces exposed. However, when hydrogels were pretreated with PLL, small diameter silica aggregration (< 100 nm) occured preferentially at the surface of collagen fibrils (Figure 8.2(b),(d)). These experiments showed that the presence of silica at the fibril surface affected the fixation and drying process of the gel which caused collapse of the network and fibril bundling (Figure 8.2(d),(f)). However, it was apparent that in PLL treated samples there was silica at the fibril surface and an absence of large homogeneous silica aggregrates.

At higher collagen concentrations (50 mg/mL), a uniform silica coating was observed. Figure 8.3 compares the microstructure of 50 mg/mL pure collagen hydrogel to that of hydrogels pretreated with PLL and soaked in Stöber solution for three days. After silica deposition, there was a statistically significant increase in fibril diameter from 18.5±0.7 to 48.9±1.3 nm (n = 100 measurements for each nominal value).

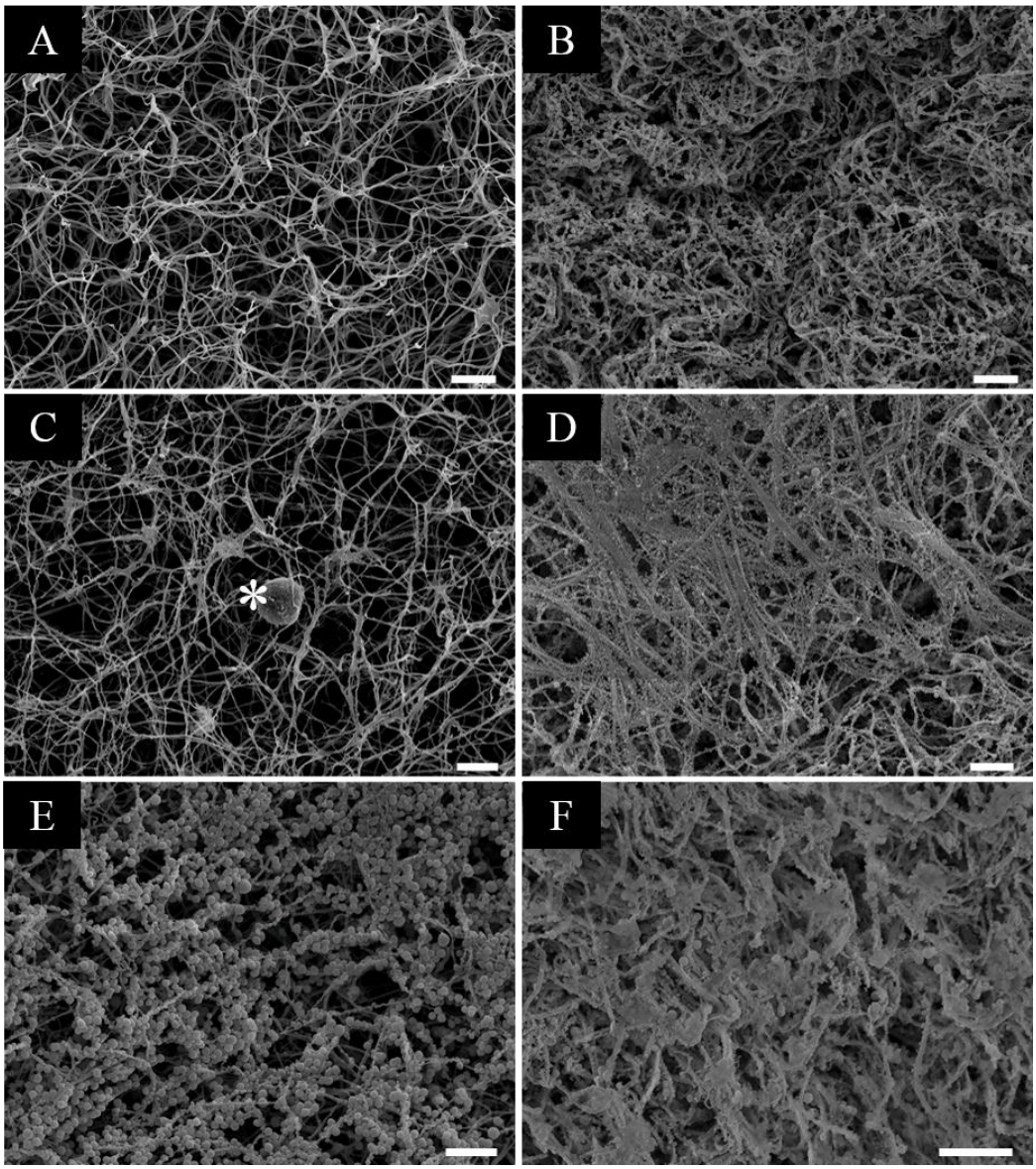

Figure 8.2: SEM images of control collagen hydrogel (a), silica-collagen hydrogels with PLL after 1 day (b), 2 days (d), and 3 days (f) of TEOS soak (R=4000), and without PLL after 1 day soak in R=4000(c) and R=400(e) TEOS bath. Asterisk marks large silica aggregate. (Each white scale bar = 1 µm in length)

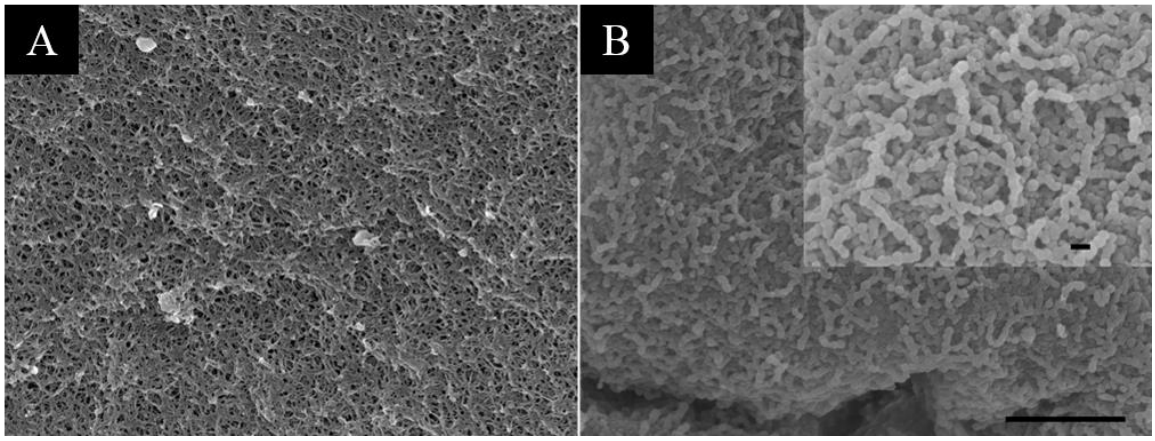

Figure 8.3: SEM image of 50 mg/mL hydrogel before (a) and after (b) PLL treatment and three-day TEOS soak. The inset is of the same sample at a higher magnification. The scale bar in the bottom right is 1 µm long and the inset scale bar is 50 nm long.

8.3.2 Chemical composition

Raman spectroscopy was performed to characterize the chemical composition and bonding present at different steps of the silica-collagen hydrogel synthesis. Figure 8.4 (b) showed that after soaking collagen in PLL solution, there was a significant amplitude increase in peaks centered about 2940 cm^{-1} which are associated with –CH bonds[197]. The increase in peak amplitude at 2940 cm^{-1} suggested that PLL was present even after rinsing and removal of solvent from the hydrogel. Upon soaking the material in Stöber solution, a sharp peak appeared at approximately 430 cm^{-1} (Figure 8.4(c)) which is associated with siloxane bonds (Si – O – Si) bending[198]. Additionally, an increase in –CH bonds was present, which was likely due to the alkyl side chains of TEOS that remained unhydrolyzed. After aging and UV exposure (Figure 8.4(e)), the decrease of -CH bonds indicated a higher degree of TEOS hydrolysis, while the broadening and shift to a higher frequency of the siloxane peak indicated an increase in condensation of the silica network[199].

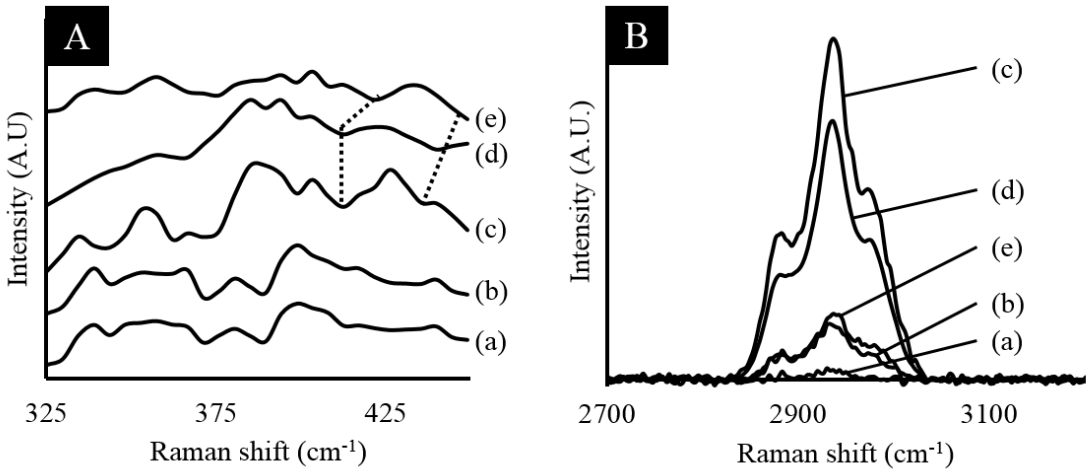

Figure 8.4: Raman spectra of (A) low and (B) high frequency ranges: (a) collagen, (b) +PLL, (c) +TEOS, (d) TA10, and (e) TA10-UV4. The dotted lines highlight the change and shift of the silica peak.

8.3.3 Collagenase degradation resistance

As described previously, unmodified collagen gels are sensitive to collagenase degradation. The deposition of silica using PLL can be used to modulate the degradation of collagen (Figure 8.5). The addition of TEOS reduced the rate of degradation for the collagen gels. Furthermore, aging of the nanocomposite hydrogels played a role in further reducing the degradation rate of the gels. Degradation testing was concluded on a sample-by-sample basis, ending when the gels became too weak to handle. The differences in residual weight percentage between the control, TA2-UV4, and TA10-UV10 at times above 200 min were statistically significant. The gel that was aged for 10 days in TEOS/Ethanol and exposed to UV for 4 h maintained mechanical stability for twice as long as the control and over 200 min longer than the sample that was aged for 2 days in TEOS/Ethanol.

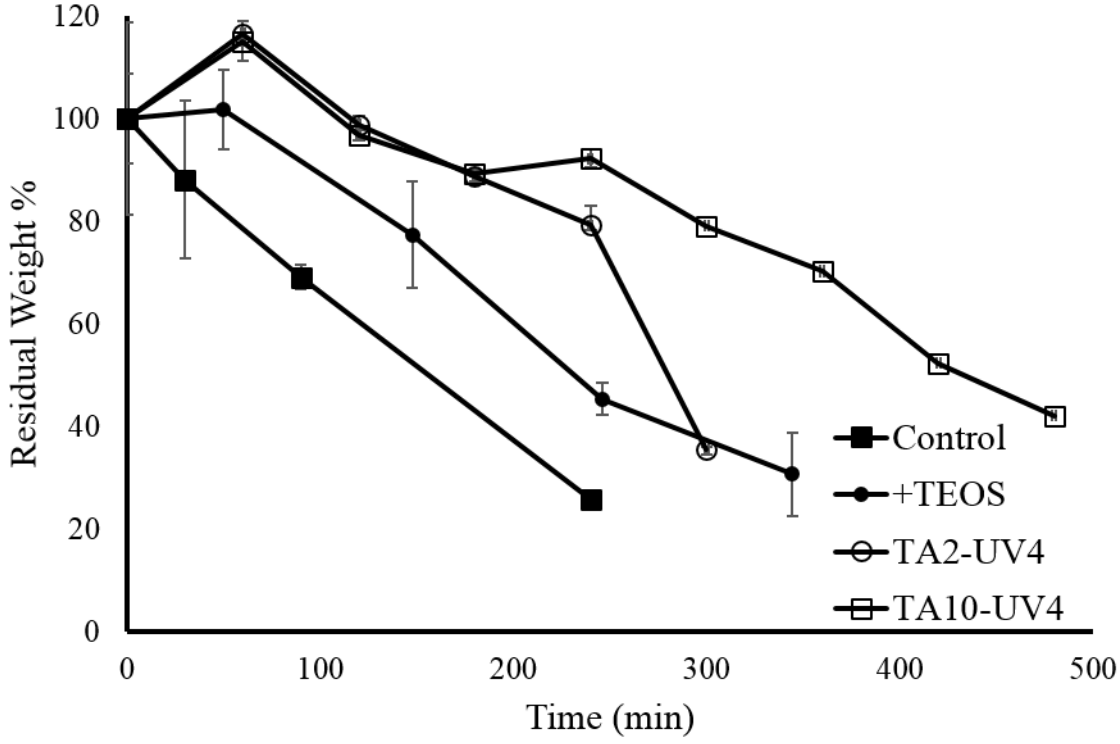

Figure 8.5: Collagenase degradation measured in terms of sample mass versus time for silica-collagen hydrogels (50 mg/mL collagen concentration). Error bars represent confidence intervals (n=4).

8.3.4 Spectral transmittance

The 50 mg/mL control had a reduced spectral transmittance at lower wavelengths compared to data published by Walsh et al. for the human cornea (Figure 8.6)[40]. However, the spectral transmittance of gels did not change significantly after silica deposition, aging, and UV exposure.

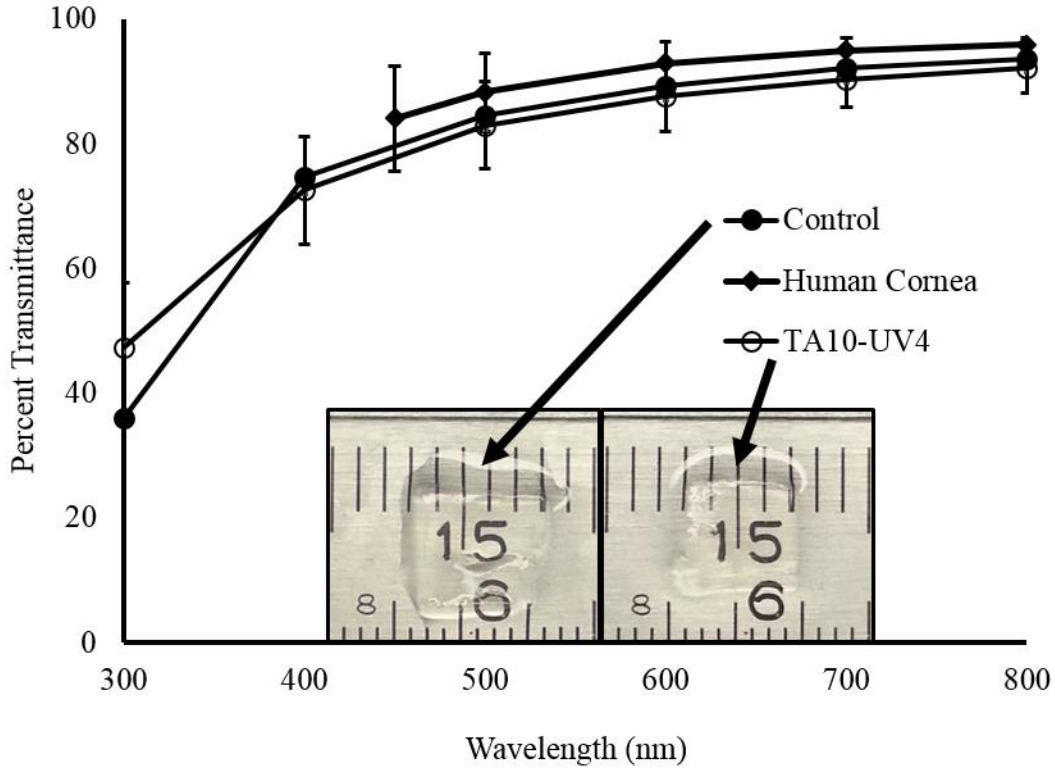

Figure 8.6: Spectral transmittance of control and silica-collagen hydrogels in comparison to published results for the human cornea[40]*. The inset contains images of the control sample (left) and silica-collagen hydrogel (right) on top of a ruler, displaying their similar transparent behavior. Error bars represent confidence intervals.*

8.3.5 Mechanical properties

The addition of silica resulted in an increase in stiffness for three different collagen concentrations (Figure 8.7, Table 8.2). For 5 mg/mL concentration gels, the control sample was too weak to handle and a significant increase in stiffness, soaking in PLL and adding Ludox silica spheres (Figure 8.8). The stiffness of the gels further increased after the silica spheres were cross-linked with TEOS. For 50 mg/mL concentration gels, stiffness increased by approximately

two orders of magnitude after silica deposition, aging and UV exposure. While the UV exposure alone contributed significantly to the stiffening of collagen fibrils, the TA10+UV4 samples experienced a significant increase in stiffness when compared to both control and UV samples, indicating that the addition of a TA10 soaking step can impart significant additional stiffness to the gel. The 100 mg/mL gels followed the same trend.

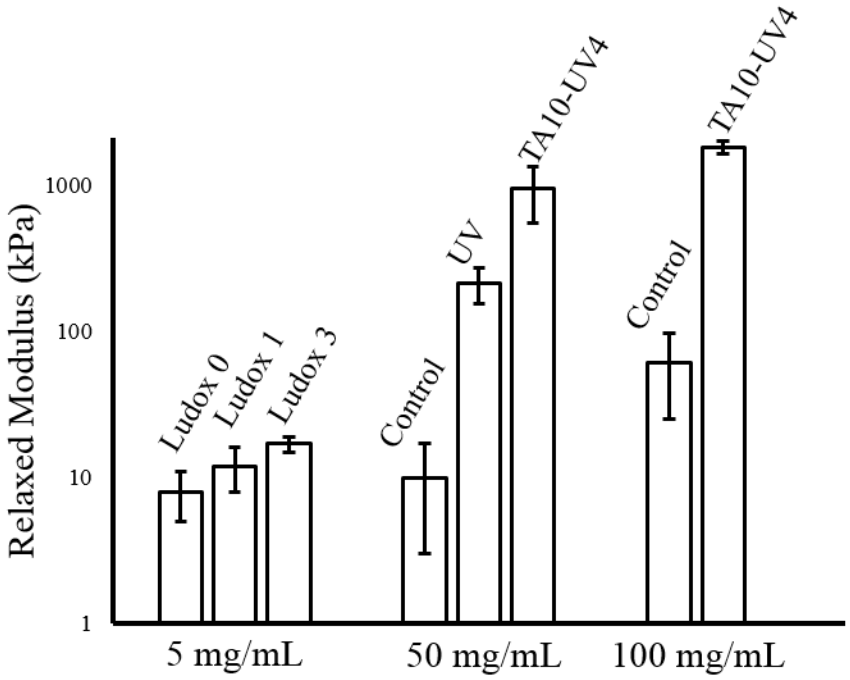

Figure 8.7: Relaxed moduli for different collagen concentrations and silica deposition treatments. 5 mg/mL: soaked in Ludox for 1 hour (Ludox 0), followed by aging in TEOS solution for 1 day (Ludox 1) and for 3 days (Ludox 3). Error bars represent confidence intervals (N=4).

Table 8.2: Tabulated relaxed moduli of silica-collagen composites.

Collagen Concentration	Sample	Relaxed Modulus (kPa)
5 mg/mL	Control	Too weak to handle
	Ludox 0	8±3
	Ludox 1	12±4
	Ludox 3	17±2
50 mg/mL	Control	10±7
	UV4	214±60
	TA10-UV4	945±391
100 mg/mL	Control	61±36
	TA10-UV4	1820±180

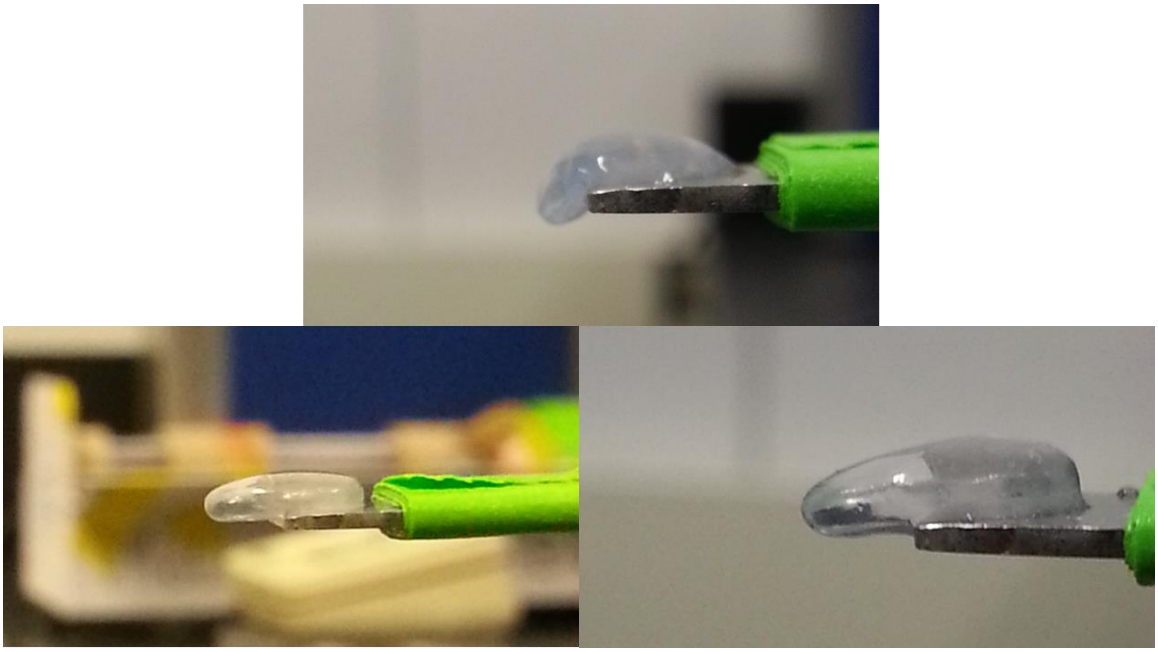

Figure 8.8: (top) Control hydrogel, (bottom) Silica-collagen composite hydrogel (Ludox 3). Due to the significant increase in rigidity upon silica deposition, hydrogel samples can be handled and maintain their shape, as opposed to the control samples, which are difficult to manipulate without resulting in mechanical failure.

8.4 Discussion

In this study, the combination of PLL treatment of the collagen network with Stöber soaking resulted in uniform deposition of silica onto collagen fibrils. PLL has been used in layer-by-layer silica coating in previous work[200,201]. Cationic PLL gives the collagen fibril surface a uniform positive charge in neutral conditions. The hydrogel can then be soaked in a silica precursor solution containing hydrolyzed TEOS molecules that have negative charge, which are electrostatically attracted to the positively charged collagen fibril surface. Without pretreating the collagen surface with PLL, aggregation between silica particles is energetically preferred over silica deposition at the collagen surface (Figure 1(c),(e)). This outcome agrees with past work that involving silica deposition onto gold nanoparticles[202].

When using Stöber solutions, the H_2O:Si molar ratio, R, is critical. Figure 8.2(e) shows that R should be kept above 400 to avoid micron-size silica clusters. The more dilute the silica precursor, the more likely that polymerization takes place at the collagen surface, thereby limiting particle growth and light scattering. Additionally, Figure 8.3 shows that this deposition technique can be used on highly concentrated hydrogels, resulting in a uniform increase in fibril diameter without a reduction in spectral transmittance (Figure 8.6). Further characterization of this conformal silica coating must be performed. It is possible that this conformal layer is not present at certain distances relative to the surface. This could be a limiting factor for increasing degradation resistance of the gels. Knowing that silica increases the index of refraction of collagen gels, backscattering intensities using confocal microscopy can be measured at different depths in the sample. Collagen fibrils without a silica coating will backscatter less light compared to composite fibrils. Therefore, backscatter intensity-depth profiles should be used in future studies to detect silica coatings. By performing these experiments, a critical sample thickness can be identified to achieve a homogeneous silica-collagen fibrils structure and the

relationship between this critical thickness and collagen concentration can be quantified. It is expected that this critical thickness will increase with decreasing collagen concentration as decreasing collagen concentration correlates with decreasing fibril density and increasing pore size.

Aging and UV exposure proved to be important in reducing the degradation rate of the gels. Gels that were not aged showed only a slight increase in degradation resistance. One can see from the intensity increase in the –CH peak region of the Raman spectra for these gels that the silica network formed around collagen is not highly condensed and retains some of its alkyl side chains. The condensation of silica around collagen is increased and fewer of the silica molecules retain their alkyl side chains after aging and densifying the network with UV exposure, which results in a significant reduction in degradation rate. It has been shown by Viitala et al. that the dissolution of silica is reduced by further increasing the extent of condensation and reducing the number of silanol (Si-OH) groups present in the gel[24,25]. The aging and densification methods used in this chapter are one way of doing this, but can potentially result in cracking of the silica network which may expose collagen fibrils to solvent.

For future studies, alternative modifications of the silica network may prove to be more effective. For example, dipodal silanes have been used to improve the hydrolytic stability of silica gels[100,203]. Also, PEG-silanes with various chemistries can be used to change the behavior of silica networks (vary porosity, hydrophobicity, act as cross-linkers between silanol groups). Preliminary results using dipodal silanes already show improved hydrolytic stability. No quantifiable data is available yet, but 5 mg/mL silica-collagen composites maintain improved mechanical properties after being kept in an aqueous environment for over two months. Without a dipodal silane treatment, silica-collagen composites experience significant swelling and become unstable after approximately one week.

The mechanical stiffness of gels was increased upon silica deposition, aging and UV exposure. For 5 mg/mL gels, the addition of Ludox spheres was critical in improving the mechanical properties of the gels, causing them to transition from weak gels that did not maintain their shape to gels capable of being handled and manipulated without material failure. This result was further exaggerated for longer Stöber soaking times. Higher concentrations of collagen had mechanical properties approaching those of the native cornea with stiffness values of approximately 1 MPa. While it is difficult to make comparisons due to differences in testing protocols, corneal stiffness values of 0.8–5 MPa have been reported for strains ranging from 4–10%[41,44,45,204]. For strains above 10%, the stiffness of the cornea has been estimated to be 35–60 MPa[42,205]. However, these cited results did not allow for the material to relax and often used high strain rates. Because of the viscoelastic behavior of collagenous tissue, stiffness values are often overestimated at high strain rates.

8.5 Conclusion

A two-step method for silica-deposition onto collagen fibrils was used to increase the stiffness and reduce the enzymatic degradation rate of collagen hydrogels without reducing visible light spectral transmittance. Chemical characterization via Raman spectroscopy and in vitro degradation experiments showed that aging and densification of the deposited silica resulted in a reduction of degradation rate. Future experiments to further reduce the degradation rate with other chemical modifications of the silica network have been proposed. Additionally, it has been suggested that further microstructural characterization needs to be performed to determine if the same homogeneous coating of silica at the surface of gels is found throughout the thickness of the sample. There may be a critical thickness for gels that cannot be exceeded without resulting in

inhomogeneous composite fibrils, necessitating that a layer-by-layer method be used with this deposition method beyond certain thicknesses.

Chapter 9

Conclusion/Future Work

9.1 Conclusions

The long-term objective of this project is to create an artificial material suitable for full-thickness corneal replacement. The short-term goal of this dissertation was to develop an artificial construct that mimics the cornea's biomechanical, optical, and biocompatibility behavior. In order to fulfill this short-term goal, **we hypothesized that the chemical and microstructural properties of silica-collagen composites can be tuned to yield favorable mechanical and degradation behavior sufficient for corneal replacement without reducing the optical properties of the gel.**

This hypothesis was supported with the research presented here in Chapters 5-8, but not by way of a copolymerization process. In Chapter 7, the biocompatibility of silica-collagen hydrogels was proven to be sufficient for corneal replacement, as the hydrogels were completely re-epithelialized in *ex vivo* tissue culture (partial thickness implant into excised rabbit cornea). Additionally, the mechanical properties of hydrogels were improved when xerogels were formed by desiccation, in agreement with results reported for silica-collagen xerogels designed for bone replacement[18]. However, this improvement in mechanical properties resulted in a significant reduction in visible light transmittance. It is possible that this material could potentially be used for partial thickness implantation, but would be unsuitable for full-thickness keratoplasty due to its limited transmittance. SEM imaging experiements showed that the high degree of light scattering present in xerogels was due to both large fibril bundles formed during dehydration, and to large silica aggregates formed in the presence of high concentrations of silica precursor.

A method that separates collagen polymerization and silica coating into two steps was shown to be effective in producing silica-collagen hybrids with good optical and mechanical behavior. A collagen hydrogel was formed using an ammonia vapor neutralization process, and the hydrogel was then coated with silica using the Stöber soaking method. Chapter 8 showed that silica coatings nanometers in thickness can be applied to collagen fibril surfaces using this two step process. In order to increase silica formation at the fibril surface and reduce aggregation in the extrafibrillar space, PLL was to provide collagen fibrils with positive charge, and therefore attract negatively charged silica precursor molecules. Other groups have shown that depositing silica onto nanoparticles requires surface treatment to produce uniform deposition[200–202]. The results in chapter 9 agree with work by Liz-Marzan et al., who showed that dilute silica concentrations (R>1000) must be used to reduce interactions between silica particles.

This two-step coating process resulted in transparent silica-collagen hydrogels with stiffness values of approximately 0.94±0.39 MPa and 1.82±0.18 MPa for 50 and 100 mg/mL collagen concentrations respectively, which are close to the range of values reported for the cornea (see Table 2.1). At 5 mg/mL collagen concentrations, the mechanical stiffness was also significantly improved while maintaining transparency. After silica addition, these originally weak samples were much stronger and became capable of maintaining their originally geometry, even when handled. Additionally, the degradation resistance of the gels was significantly improved compared to control samples, especially after aging and UV exposure increased the condensation and density of the deposited silica networks.

This work comprises Aim 2 of this thesis, which proposed to tune the mechanical and degradation behavior of collagen hydrogel without reducing the optical properties of the gel. The success of the experiments described here show that this aim has been completed. While the degradation rate of these gels is still more rapid than that of the cornea, preliminary results from continuing work have shown that silica deposition can be improved to enhance the hydrolytic

resistance of the gels (discussed in next section). Therefore, this method shows great potential to yield a material suitable for corneal replacement, which supports the long-term objective of this project.

Aim 1 of this thesis proposed to tune the optical properties of collagen hydrogels by controlling features such as fibril spacing, diameter, and orientation. In the first step of the two-step process to create silica coated collagen hydrogels, the mechanical properties of 5 mg/mL hydrogels were improved by an order of magnitude when the collagen solution was dialyzed to a 50 mg/mL concentration. Chapter 4 showed that this increase in concentration did not result in opacification when ammonia vapor neutralization method was used instead of buffer neutralization. Chapter 4 also showed that the optics of hydrogels are heavily dependent on the diameter of fibrils, and rapid neutralization using ammonia vapor exposure produced much smaller fibrils and therefore more transparent hydrogels. Also, as fibril spacing decreases with increasing collagen concentration above 50 mg/mL, the transparency of hydrogels begins to reduce significantly. This result agrees with observations by Gobeaux et al.[121].

Previous groups using the same Rayleigh scattering model used in Chapter 4 showed that transparency of the cornea is not due to its semi-crystalline fibril arrangement[110,111]. It has been proposed that Fourier components of the spatial density fluctuations dominate the cornea's optics, and keeping the wavelengths of these fluctuations significantly smaller than the incident wavelength reduces light scattering[107]. The results in Chapter 4 qualitatively confirm this theory. Transparent ammonia vapor neutralized samples had fibrils uniformly distributed as shown in TEM cross-sections, while opaque buffer neutralized samples contained large fibril clusters as well as large voids with no fibrils. Due to significant overestimates of transmittance made by the Rayleigh scattering model compared to experimental findings, it was suggested that features not incorporated in the model contribute significantly to light scattering. Therefore, it was

hypothesized that aligned fibril arrays reduce the size and frequency of nodes, resulting in increased transparency of the gel.

Based on this hypothesis, Chapters 5 and 6 showed that it was possible to reduce light scattering in collagen hydrogels by increasing fibril alignment. It was hypothesized that fibril alignment reduces fibril intersections, which in turn reduces light scattering. This hypothesis appears to be true based on the transmittance results of gels with biomodal fibril arrangement induced via nanowire alignment, and gels with unidirectional alignment obtained after addition of nanocrystalline cellulose particles. Both of these fibril alignment methods increased the transmittance of collagen hydrogels, fulfilling the objectives of Aim 1. The alignment produced from magnetic nanowires was unique in that it produced fibril alignment in two orthogonal directions parallel to the hydrogel surface (5 mg/mL collagen hydrogels). This alignment required covalent interactions between collagen molecules and the nanowires' functionalized surface, which was mediated using a cross-linking agent (CDI). In addition to optical improvements, these aligned hydrogels were biocompatible, and induced attachment and alignment of actin filaments in top-seeded arachnoid cells.

When NCC was added to highly concentrated collagen hydrogels (150 mg/mL), there was a strong unidirectional alignment that was not present for pure collagen samples of the same concentration. There was also a significant reduction in the average and standard deviation of fibril diameters upon NCC addition. It was proposed that hydrogen bonding between the polar surface of NCC particles and hydroxylated amino acid side chains of collagen molecules dictated alignment. This was supported by results that showed alignment did not result in the presence of methylcellulose instead of NCC (which contains hydroxyl groups on its surface). The NCC-collagen hydrogels were also biocompatible, and promoted attachment and proliferation of seeded HFFs on the top surface. In addition to optical improvements, some preliminary results showed a slight increase in mechanical properties of the gels when NCC was added to 5 mg/mL collagen

hydrogels (2% NCC). However, more samples must be acquired to produce a statistically significant result.

The methods proposed and executed in this dissertation have been used to improve the mechanical stability, optical transparency, and enzymatic degradation resistance of collagen hydrogels. Although more experiments (suggested in the following section) should be carried out to further characterize and develop these methods, the silica-collagen hydrogels presented here show great potential for corneal replacement.

9.2 Future work

A great deal of progress has been made toward the development of an artificial cornea replacement in this thesis. With that said, there is still work that needs to be done to build on the results presented. The presented methods for producing transparent hydrogels via NCC addition or magnetic nanowire alignment need to be further characterized and optimized. The same can be said about the PLL-templated silica deposition process. Once these methods are optimized, work to combine these processes with an automated manufacturing technique to produce sterile clinical implants can begin.

9.2.1 Collagen hydrogel optics

As suggested in Chapter 4, further characterization must be carried out to quantify the number, size, and scattering contributions of fibril nodal points. It was hypothesized that these nodal points are partially responsible for the deviation of experimental results from the Rayleigh scattering model. In order to eliminate sample preparation artifacts, confocal reflectance microscopy would be a great way to characterize scattering events throughout the thickness of hydrogel samples. It is difficult to interpret structures such as fibril nodes and bundling using

SEM, and TEM involves time-consuming sample preparation methods that may be altering the native fibrillar structure. Confocal imaging techniques have been used to characterize the microstructure of collagen hydrogels[135,136], as well as the cornea[206–208]. Comparing the confocal results of aligned samples from Chapter 5 with the amorphous samples of Chapter 4 could add support to current optical theories presented, as well as assist in defining an alignment length scale necessary for producing transparent hydrogels.

9.2.2 Optimization of nanowire-collagen aligned hydrogels

The alignment results in Chapter 5 show great potential for producing transparent hydrogels for corneal replacement, as well as other tissue engineering applications that require multi-directional alignment for improved mechanical properties. Mechanical testing of aligned hydrogels needs to be performed to quantify improvements in mechanical stiffness that result from the orthogonal arrangement of fibrils. These hydrogels can also be used as a synthetic environment to observe mechano-responses of different cell types *in vitro*.

In the context of the present project, optimizing this technique for corneal replacement will require this alignment using high collagen concentrations. The optimal length, diameter, and concentration of nanowires for alignment/transmittance will require more experiments to identify. For higher concentrations, it is hypothesized that smaller nanowire diameters will be necessary to reduce nanowire contributions to light scattering. However, the aspect ratio of nanowires will be limited by the nanowires' ability to align with the applied magnetic field. An increase in aspect ratio reduces the magnetic moment of the nanowire. Also, solution viscosity increases with collagen concentration. Determining the alignment limitations of nanowires in different collagen concentrations will dictate whether this technique will be useful for producing transparent hydrogels suitable for cornea replacement.

9.2.3 2-D template alignment of collagen using NCC

The results from Chapter 6 show that NCC has the ability to align highly concentrated collagen hydrogels. More experiments are required to understand this alignment mechanism. Specifically, understanding how the crystallinity of NCC particles affects collagen molecule arrangement will provide additional insight necessary before proposing an alignment mechanism. The methods used in Chapter 6 did not control or quantify the amorphous regions of cellulose still present in the NCC suspension. By using previously described acid hydrolysis methods with x-ray diffraction spectroscopy, crystallinity can be modulated and measured. Cellulose in its natural state is composed of nanocrystals and amorphous regions. Nanocrystals with diameters on the order of 10 nm and aspect ratios larger than 100 are possible to isolate using currently available acid hydrolysis techniques. Using these nanocrystal suspensions may result in improved alignment and transparency due to the increase in their crystallinity and reduced width.

Chapter 4 showed that 100 mg/mL hydrogels in contact with a cellulose dialysis membrane during fibril formation had an organized structure at the contacted surface. This alignment was not observed throughout the bulk of the sample and therefore did not result in an increase in transparency. Further characterization should be performed to quantify a length scale for this surface alignment effect. Even if surface alignment only stretches over distances on the order of micrometers, cellulose membranes can be candidate template surfaces used in 3D printing of aligned collagen hydrogels.

9.2.4 Characterizing and improving scalability of silica deposition onto collagen

Chapter 8 showed promising uniform silica coating results. However, the effective distance that this coating covers is still unknown. One way to probe the entire thickness and

assess silica coating is to perform confocal microscopy experiments that estimate the reflectance/backscatter of incident light at various focal planes[133,134]. The results in Chapter 7 showed that a measureable increase in refractive index occurs upon silica addition. The refractive index of solvent can be tuned with sucrose, and the intensity of back-scattered light will be minimized when the refractive index of the solvent matches the effective refractive index of the composite fibrils. By performing this technique at different depths, a refractive index profile with respect to axial distance can be compiled. A uniform refractive index profile would be indicative of homogeneous silica deposition. Confocal Raman spectroscopy could also be used to estimate the degree of silica deposition at different depths within a sample. However, it may be difficult to sense silica-associated peaks within hydrated composites.

Once the effectiveness of the PLL-Stober soaking method is characterized, improvements can be made to allow for silica deposition at larger distances from the sample surface. Additionally, the effects of collagen concentration (and therefore pore size) can be observed. Once a uniform coating is confirmed to exist throughout the bulk of the material, stabilizing agents can be added to improve the stability of the deposited silica network. For example, various PEG-silane molecules have been used to passivate the surface of mesoporous colloidal silica which prevented rapid degradation in physiological environments[101,102]. Dipodal silanes have been used as cross-linking agents which improve strength as well as hydrolytic stability of various materials[100,203].

9.2.5 Conclusion

The work presented in this dissertation will act as a foundation for the experiments proposed in the previous sections. With further characterization of the alignment techniques and silica deposition procedure introduced, silica-collagen composites can be improved and optimized

in terms of biomechanical, optical, and degradation properties. Ultimately, these future experiments are the next step in fulfilling the long term goal of manufacturing silica-collagen implants suitable for corneal replacement.

Bibliography

1. Whitcher J, Srinivasan M, Upadhyay M. Corneal blindness: a global health perspective. *Bull World Health Organ*. 2001;79(3):233-236.

2. EBAA. 2010-2011, A Year in Review. 2010.

3. Beck R, Gal R, Mannis M, et al. Is donor age an important determinant of graft survival? *Cornea*. 1999;18(5):503-510.

4. Greiner MA, Li JY, Mannis MJ. Longer-term vision outcomes and complications with the Boston type I keratoprosthesis at the University of California, Davis. *Ophthalmology*. 2011;118(8):1543-1550.

5. Aldave AJ, Kamal KM, Vo RC, Yu F. The boston type I keratoprosthesis: improving outcomes and expanding indications. *Ophthalmology*. 2009;116(4):640-651.

6. Aldave AJ, Sangwan VS, Basu S, et al. International results with the Boston type I keratoprosthesis. *Ophthalmology*. 2012;119(8):1530-1538.

7. Aquavella J V, Qian Y, McCormick GJ, Palakuru JR. Keratoprosthesis: the Dohlman-Doane device. *Am J Ophthalmol*. 2005;140(6):1032-1038.

8. EBAA. Eye Bank Association of America. 2010-2011, A Year in Review. 2011.

9. Hicks CR, Crawford GJ, Lou X, et al. Corneal replacement using a synthetic hydrogel cornea, AlphaCor: device, preliminary outcomes and complications. *Eye*. 2003;17(3):385-392.

10. Ma JJK, Graney JM, Dohlman CH. Repeat penetrating keratoplasty versus the Boston keratoprosthesis in graft failure. *Int Ophthalmol Clin*. 2005;45(4):49-59.

11. Fagerholm P, Lagali NS, Merrett K, et al. A biosynthetic alternative to human donor tissue for inducing corneal regeneration: 24-month follow-up of a phase 1 clinical study. *Sci Transl Med*. 2010;2(46):46ra61.

12. Fagerholm P, Lagali NS, Ong JA, et al. Stable corneal regeneration four years after implantation of a cell-free recombinant human collagen scaffold. *Biomaterials*. 2014;35:2420-2427.

13. Doillon CJ, Watsky MA, Hakim M, et al. A collagen-based scaffold for a tissue engineered human cornea: Physical and physiological properties. *Int J Artif Organs*. 2003;26(8):764-773.

14. Chen S, Osaka A, Hanagata N. Collagen-templated sol–gel fabrication, microstructure, in vitro apatite deposition, and osteoblastic cell MC3T3-E1 compatibility of novel silica nanotube compacts. *J Mater Chem*. 2011;21(12):4332.

15. Coradin T, Helary C, Livage J. A novel route to collagen-silica biohybrids. *Mater Res Soc Symp Proc*. 2002;726:1-5.

16. Desimone MF, Hélary C, Mosser G, Giraud-Guille M-M, Livage J, Coradin T. Fibroblast encapsulation in hybrid silica–collagen hydrogels. *J Mater Chem*. 2010;20(4):666.

17. Eglin D, Coradin T, Giraud Guille MM, Helary C, Livage J. Collagen-silica hybrid materials: sodium silicate and sodium chloride effects on type I collagen fibrillogenesis. *Biomed Mater Eng*. 2005;15(1-2):43-50.

18. Heinemann S, Coradin T, Worch H, Wiesmann HP, Hanke T. Possibilities and limitations of preparing silica/collagen/hydroxyapatite composite xerogels as load-bearing biomaterials. *Compos Sci Technol*. 2011;71(16):1873-1880.

19. Lee E-J, Jun S-H, Kim H-E, Koh Y-H. Collagen-silica xerogel nanohybrid membrane for guided bone regeneration. *J Biomed Mater Res A*. 2012;100(4):841-847.

20. Niu L, Jiao K, Qi Y, et al. Infiltration of silica inside fibrillar collagen. *Angew Chem Int Ed Engl*. 2011;50(49):11688-11691.

21. Ono Y, Kanekiyo Y, Inoue K, Hojo J, Nango M, Shinkai S. Preparation of novel hollow fiber silica using collagen fibers as a template. *Chem Lett*. 1999;6:475-476.

22. Chen S, Osaka A, Ikoma T, et al. Fabrication, microstructure, and BMP-2 delivery of novel biodegradable and biocompatible silicate-collagen hybrid fibril sheets. *J Mater Chem*. 2011;21(29):10942-10948.

23. Viitala R, Jokinen M, Maunu SL, Jalonen H, Rosenholm JB. Chemical characterization of bioresorbable sol-gel derived SiO2 matrices prepared at protein-compatible pH. *J Non Cryst Solids*. 2005;351(40):3225-3234.

24. Viitala R, Jokinen M, Rosenholm JB. Mechanistic studies on release of large and small molecules from biodegradable SiO2. *Int J Pharm*. 2007;336(2):382-390.

25. Viitala R, Jokinen M, Tuusa S, Rosenholm JB, Jalonen H. Adjustably bioresorbable sol-gel derived SiO2 matrices for release of large biologically active molecules. *J Sol-Gel Sci Technol*. 2005;36(2):147-156.

26. Radin S, Falaize S, Lee MH, Ducheyne P. In vitro bioactivity and degradation behavior of silica xerogels intended as controlled release materials. *Biomaterials*. 2002;23(15):3113-3122.

27. Kortesuo P, Ahola M, Karlsson S, Kangasniemi I, Yli-Urpo A, Kiesvaara J. Silica xerogel as an implantable carrier for controlled drug delivery-evaluation of drug distribution and tissue effects after implantation. *Biomaterials*. 2000;21(2):193-198.

28. Falaize S, Radin S, Ducheyne P. In vitro behavior of silica-based xerogels intended as controlled release carriers. *Jounal Am Ceram Soc*. 1999;82(4):969-976.

29. Desimone MF, Helary C, Quignard S, et al. In vitro studies and preliminary in vivo evaluation of silicified concentrated collagen hydrogels. *ACS Appl Mater Interfaces*. 2011;3(10):3831-3838.

30. Hjortdal JO, Jensen PK. In vitro measurement of corneal strain, thickness, and curvature using digital image processing. *Acta Ophthalmol Scand*. 1995;73:5-11.

31. Beurman RW, Pedroza L. Ultrastructure of the human cornea. *Microsc Res Tech*. 1996;33(4):320-335.

32. DelMonte DW, Kim T. Anatomy and physiology of the cornea. *J Cataract Refract Surg*. 2011;37(3):588-598.

33. Komai Y, Ushiki T. The three-dimensional organization of fibrils in the human cornea and sclera. *Invest Ophthalmol Vis Sci*. 1991;32(8):2244-2258.

34. Meek KM, Leonard DW. Ultrastructure of the corneal stroma: a comparative study. *Biophys J*. 1993;64(1):273-280.

35. Muller LJ, Pels E, Schurmans LR, Vrensen GF. A new three-dimensional model of the organization of proteoglycans and collagen fibrils in the human corneal stroma. *Exp Eye Res*. 2004;78(3):493-501.

36. Meek KM, Dennis S, Khan S. Changes in the refractive index of the stroma and its extrafibrillar matrix when the cornea swells. *Biophys J*. 2003;85(4):2205-2212.

37. Meek KM, Leonard DW, Connon CJ, Dennis S, Khan S. Transparency, swelling and scarring in the corneal stroma. *Eye*. 2003;17(8):927-936.

38. Meek KM. The cornea and sclera. In: Fratzl P, ed. *Collagen*. Vol Springer science & business media; 2008:359-396.

39. Van den Berg TJTP, Tan KEWP. Light transmittance of the human cornea from 320 to 700 nm for different ages. *Vision Res*. 1994;34(11):1453-1456.

40. Walsh J, Bergmanson J, Koehler L, Doughty M, Fleming D, Harmey J. Fibre optic spectrophotometry for the in vitro evalutation of ultraviolet radiation (UVR) sprectral transmittance of rabbit corneas. *Physiol Meas*. 2008;29(3):375.

41. Elsheikh A, Anderson K. Comparative study of corneal strip extensometry and inflation tests. *J R Soc Interface*. 2005;2(3):177-185.

42. Andreassen TT, Simonsen AH, Oxlund H. Biomechanical properties of keratoconus and normal corneas. *Exp Eye Res*. 1980;31:435-441.

43. Nash IS, Greene PR, Foster CS. Comparison of mechanical properties of keratonus and normal corneas. *Exp Eye Res*. 1982;35:413-423.

44. Hoeltzel DA, Altman P, Buzard K, Choe K-I. Strip extensiometry for comparison of the mechanical response of bovine, rabbit, and human corneas. *J Biomech Eng*. 1992;114:202-215.

45. Wollensak G, Spoerl E, Seiler T. Stress-strain measurements of human and porcine corneas after riboflavin-ultraviolet-A-induced cross-linking. *J Cataract Refract Surg*. 2003;29:1780-1785.

46. Liu W, Deng C, McLaughlin CR, et al. Collagen-phosphorylcholine interpenetrating network hydrogels as corneal substitutes. *Biomaterials*. 2009;30:1551-1559.

47. Beck RW, Gal RL, Mannis MJ, et al. Is donor age an important determinant of graft survival? *Cornea*. 1999;18(5):503-510.

48. Dohlman CH, Schneider HA, Doane MG. Prosthokeratoplasty. *Am J Ophthalmol*. 1974;77(5):694-700.

49. Hartmann L, Watanabe K, Zheng LL, et al. Toward the development of an artificial cornea: improved stability of interpenetrating polymer networks. *J Biomed Mater Res B Appl Biomater*. 2011;98(1):8-17.

50. Aquavella J V, Qian Y, McCormick GJ, Palakuru JR. Keratoprosthesis: current techniques. *Cornea*. 2006;25(6):656-662.

51. Crawford GJ, Hicks CR, Lou X, et al. The Chirila Keratoprosthesis: phase I human clinical trial. *Ophthalmology*. 2002;109(5):883-889.

52. Gomaa A, Comyn O, Liu C. Keratoprostheses in clinical practice-a review. *Clin Experiment Ophthalmol*. 2010;38(2):211-224.

53. Chirila T V. An overview of the development of articial corneas with porous skirts and the use of PHEMA for such an application. *Biomaterials*. 2001;22(24):3311-3317.

54. Jiraskova N, Rozsival P, Burova M, Kalfertova M. AlphaCor artifical cornea: clinical outcome. *Eye*. 2011;25(9):1138-1146.

55. Hicks CR, Crawford GJ, Chirila T V, et al. Development and clinical assessment of an artifical cornea. *Prog Retin Eye Res*. 2000;19(2):149-170.

56. Hicks CR, Crawford GJ, Lou X, et al. Corneal replacement using a synthetic hydrogel cornea, AlphaCor: device, preliminary outcomes and complications. *Eye*. 2003;17(3):385-392.

57. Wong AC, Yiu EP. Boston keratoprosthesis for ocular chemical injury: one-year clinical outcome. *HKJ Ophthalmol*. 2012;16:24-29.

58. Tan A, Tan D, Tan X-W, Mehta J. Osteo-odonto keratoprosthesis: systematic review of surgical outcomes and complication rates. *Ocul Surf*. 2012;10(1):15-25.

59. Marchi V, Ricci R, Pecorella I, Ciardi A, Di Tondo U. Osteo-odonto-keratoprosthesis. *Cornea*. 1994;13(2):125-130.

60. Jacob JT, Rochefort JR, Bi J, Gebhardt BM. Corneal epithelial cell growth over tethered-protein/peptide surface-modified hydrogels. *J Biomed Mater Res part b Appl Biomater*. 2005;72(1):198-205.

61. Uchino Y, Shimmura S, Miyashita H, et al. Amniotic membrane immobilized poly(vinyl alcohol) hybrid polymer as an artificial cornea scaffold that supports a stratified and differentiated corneal epithelium. *J Biomed Mater Res part b Appl Biomater*. 2007;81(1):201-206.

62. Germain L, Carrier P, Auger FA, Salesse C, Guerin SL. Can we produce a human corneal equivalent by tissue engineering? *Prog Retin Eye Res*. 2000;19(5):497-527.

63. Myung D, Farooqui N, Zheng LL, et al. Bioactive interpenetrating polymer network hydrogels that support corneal epithelial wound healing. *J Biomed Mater Res A*. 2009;90(1):70-81.

64. Myung D, Koh W, Ko J, et al. Biomimetic strain hardening in interpenetrating polymer network hydrogels. *Polymer (Guildf)*. 2007;48(18):5376-5387.

65. Liu Y, Griffith M, Watsky MA, et al. Properties of porcine and recombinant human collagen matrices for optically clear tissue engineering applications. *Biomacromolecules*. 2006;7(6):1819-1828.

66. Eyre D. Collagen: molecular diversity in the body's protein scaffold. *Science (80-)*. 1980;207(4437):1315-1322.

67. Fraser R, MacRae T, Suzuki E. Chain conformation in the collagen molecule. *J Mol Biol*. 1979;129(3):463-481.

68. Rich A, Crick F. The molecular structure of collagen. *J Mol Biol*. 1961;3(5):1961.

69. Ramachandran GN. *Treatise on Collagen*. Academic press; 1967.

70. Piez KA, Miller A. The structure of collagen fibrils. *J Supramol Struct*. 1974;2:121-137.

71. Hulmes D. Collagen diversity, synthesis and assembly. In: Fratzl P, ed. *Collagen: Structure and Mechanics*. Vol Springer; 2008:15047.

72. Kadler KE, Holmes DF, Trotter JA, Chapman JA. Collagen fibril formation. *Biochem J*. 1996;316:1-11.

73. Comper W, Veis A. The mechanism of nucleation for in vitro collagen fibril formation. *Biopolymers*. 1977;16:2113-2131.

74. Christiansen DL, Huang EK, Silver FH. Assembly of type I collagen: fusion of fibril subunits and the influence of fibril diameter on mechanical properties. *Matrix Biol*. 2000;19:409-420.

75. Gelman RA, Poppke DC, Piez KA. Collagen fibril formation in vitro. *J Biol Chem*. 1979;254(22):11741-11745.

76. Williams BR, Gelman RA, Poppke DC, Piez KA. Collagen fibril formation: optimal in vitro conditions and preliminary kinetic results. *J Biol Chem*. 1978;253(18):6578-6585.

77. Silver F. Type I collagen fibrillogenesis in vitro: additional evidence for the assembly mechanism. *J Biol Chem*. 1981;256:4973-4977.

78. Silver F. A molecular model for linear and lateral growth of type I collagen fibrils. *Collagen Relat Res*. 1982;2:219-229.

79. Silver F. A two step model for lateral growth of collagen fibrils. *Collagen Relat Res*. 1983;3:167-180.

80. Silver F, Langley K, Trelstad R. Type I collagen fibrillogenesis: initiation via reversible linear and lateral growth steps. *Biopolymers*. 1979;18(2523-2535).

81. Ward NP, Hulmes DJ, Chapman JA. Collagen self-assembly in vitro: electron microscopy of initial aggregates formed during the lag phase. *J Mol Biol*. 1986;190:107-112.

82. Goh M, Paige M, Gale M, Yadegari I, Edirisinghe M, Strzelczyk J. Fibril formation in collagen. *Physica A*. 1997;239:95-102.

83. Otter A, Scott PG, Kotovych G. Type I collagen alpha-1 chain c-telopeptide: solution structure determined by 600-MHz proton NMR spectroscopy and implications for its role in collagen fibrillogenesis. *Biochemistry*. 1988;27:3560-3567.

84. Capaldi MJ, Chapman JA. The c-terminal extrahelical peptide of type I collagen and its role in fibrillogenesis in vitro. *Biopolymers*. 1982;21:2291-2313.

85. Helseth DL, Lechner JH, Veis A. Role of the amino-terminal extrahelical region of type I collagen in directing the 4D overlap in fibrillogenesis. *Biopolymers*. 1979;18:3005-3014.

86. Helseth DL, Veis A. Collagen self assembly in vitro. *J Biol Chem*. 1981;256(14):7118-7128.

87. Kuznetsova N, Leikin S. Does the triple helical domain of type I collagen encode molecular recognition and fiber assembly while telopeptides serve as catalytic domains. *J Biol Chem*. 1999;274(51):36083-36088.

88. Leibovich S, Weiss JB. Electron microscope studies of the effects of endo- and exopeptidase digestion on tropocollagen. *Biochim Biophys Acta*. 1970;214:445-454.

89. Miyahara M, Hayashi K, Berger J, et al. Formation of collagen fibrils by enzymatic cleavage of precursors of type I collagen in vitro. *J Biol Chem*. 1984;259(15):9891-9898.

90. Wood G. The formation of fibrils from collagen solutions: a mechanism of collagen fibril formation. *Biochem J*. 1960;75(3):598-605.

91. Holmes D, Capaldi M, Chapman J. Reconstitution of collagen fibrils in vitro; the assembly process depends on the initiation procedure. *Int J Biol Macromol*. 1986;8(3):161-166.

92. Saeidi N, Karmelek KP, Paten JA, Zareian R, DiMasi E, Ruberti JW. Molecular crowding of collagen: highly organized collagenous tissue. *Biomaterials2*. 2012;33:7366-7374.

93. Giraud-Guille M-M. Liquid crystalline phases of sonicated type I collagen. *Biol cell*. 1989;67(1):97-101.

94. Giraud-Guille M-M, Besseau L, Martin R. Liquid crystalline assemblies in collagen in bone and in vitro systems. *J Biomech*. 2003;36:1571-1579.

95. Neame P, Kay C, McQuillan D, Beales M, Hassell J. Independent modulation of collagen fibrillogenesis by decorin and lumican. *Cell Mol life Sci*. 2000;57:859-863.

96. Prockop D, Fertala A. Inhibition of the self-assembly of collagen I into fibrils with synthetic peptides demonstration that assembly is driven by specific bind sites on the monomers. *J Biol Chem*. 1998;273(25):15598-15604.

97. Birk DE, Fitch JM, Babiarz JP, Doane KJ, Linsenmayer TF. Collagen fibrillogenesis in vitro: interaction of types I and V collagen regulates fibril diameter. *J Cell Sci*. 1990;95:649-657.

98. Brinker C, Scherer GW. *Sol-Gel Science: The Physics and Chemistry of Sol-Gel Processing*. Academic press; 2013.

99. Heinemann S, Heinemann C, Jager M, Neunzehn J, Wiesmann H, Hank T. Effect of silica and hydroxyapatite mineralization on the mechanical properties and the biocompatibility of nanocomposite collagen scaffolds. *ACS Appl Mater Interfaces*. 2011;3(11):4323-4331.

100. Matinlinna J, Lassila L, Vallittu P. The effect of a novel silane blend system on resin bond strength to silica-coated Ti substrate. *J Dent*. 2006;34:436-443.

101. Lin Y, Abadeer N, Haynes C. Stability of small mesoporous silica nanoparticles in biological media. *Chem Commun*. 2011;47:532-534.

102. Cauda V, Schlossbauer A, Bein T. Bio-degradation study of colloidal mesoporous silica nanoparticles: Effect of surface functionalization with organo-silanes and poly(ethylene glycol). *Microporous mesoporous Mater*. 2010;132(1-2):60-71.

103. Sharma A, Orlowski G, Zhu Y, et al. Inducing cells to disperse nickel nanowires via integrin-mediated responses. *Nanotechnology*. 2015;26(13):135102.

104. Hæreid S, Dahle M, Lima S, Einarsrud M-A. Preparation and properties of monolithic silica xerogels from TEOS-based alcogels aged in silane solutions. *J Non Cryst Solids*. 1995;186:96-103.

105. Lam C, Hansen E, Hubel A. Arachnoid cells on culture plates and collagen scaffolds: phenotypes and transport properties. *Tissue Eng part A*. 2011;17(13&14):1759-1766.

106. Evans MD, McFarland GA, Xie RZ, Taylor S, Wilkie JS, Chaouk H. The use of corneal organ culture in biocompatibility studies. *Biomaterials*. 2002;23(5):1359-1367.

107. Benedek GB. Theory of transparency of the eye. *Appl Opt*. 1971;10(3):459-473.

108. Freegard TJ. The physical basis of transparency of the normal cornea. *Eye*. 1997;11:465-471.

109. Maurice DM. The structure and transparency of the cornea. *J Physiol*. 1957;136(2):263-286.

110. Hart RW, Farrell RA. Light scattering in the cornea. *JOSA*. 1969;59(6):766-773.

111. Goldman JN, Benedek GB. The relationship between morphology and transparency in the nonswelling corneal stroma of the shark. *Invest Ophthalmol*. 1967;6(6):574.

112. Freund D, McCally RL, Farrell R. Direct summation of fields for light scattering by fibrils with application to normal corneas. *Appl Opt*. 1986;25(16):2739-2746.

113. Gusnard D, Kirshner R. Cell and organelle shrinkage during preparation for scanning electron microscopy: effects of fixation, dehydration and critical point drying. *J Microsc*. 1977;110(1):51-57.

114. Fullwood N, Meek K. A synchotron X-ray study of the changes occuring in the corneal stroma during processing for electron microscopy. *J Microsc*. 1993;169(1):53-60.

115. Cassel J. Collagen aggregation phenomena. *Biopolymers1*. 1966;4:989-997.

116. Trelstad R, Hayashi K, Gross J. Collagen fibrillogenesis: intermediate aggregates and suprafibrillar order. *Cell Biol*. 1976;73(11):4027-4031.

117. Gelman R, Williams B, Piez K. Collagen fibril formation: evidence for a multistep process. *J Biol Chem*. 1979;254(1):180-186.

118. Gale M, Pollanen M, Markiewicz P, Goh M. Sequential assembly of collagen revealed by atomic force microscopy. *Biophys J*. 1995;68:2124-2128.

119. Gross J, Kirk D. The heat precipitation of collagen from neutral salt solutions: some rate-regulating factors. *J Biol Chem*. 1958;233:355-360.

120. Bensusan H, Hoyt B. The effect of various parameters on the rate of formation of fibers from collagen solutions. *J Am Chem Soc*. 1958;80(3):719-724.

121. Gobeaux F, Mosser G, Anglo A, et al. Fibrillogenesis in dense collagen solutions: a physicochemical study. *J Mol Biol*. 2008;376(5):1509-1522.

122. Achilli M, Mantovani D. Tailoring mechanical properties of collagen-based scaffolds for vascular tissue engineering: the effects of pH, temperature and ionic strength on gelation. *Polymers (Basel)*. 2010;2(4):664-680.

123. Stamov D, Stock E, Franz C, Jahnke T, Haschke H. Imaging collagen type I fibrillogenesis with high spatiotemporal resolution. *Ultramicroscopy*. 2015;149:86-94.

124. Hulmes D, Miller A, Parry D, Piez K, Woodhead-Galloway J. Analysis of the primary structure of collagen for the origins of molecular packing. *J Mol Biol*. 1973;79:137-148.

125. Trus B, Piez K. Molecular packing of collagen: three-dimensional analysis of electrostatic interactions. *J Mol Biol*. 1976;108:705-732.

126. Bernengo J, Herbage D, Marion C, Roux B. Intermolecular interaction studies on native and enzyme-treated acid-soluble collagen. *Biochem Biophys acta*. 1978;532:305-314.

127. Ripamonti A, Roveri N, Braga D, Hulmes D, Miller A, Timmins P. Effects of pH and ionic strength on the structure of collagen fibrils. *Biopolymers*. 1980;19:965-975.

128. Rosenblatt J, Devereux B, Wallace D. Injectable collagen as a pH-sensitive hydrogel. *Biomaterials*. 1994;15(12):985-995.

129. Hu X, Knight D, Grant R. The effect of deamination and/or blocking arginine residues on the molecular assembly of acid-extracted rat tail tendon collagen. *Tissue Cell*. 1996;28(2):215-222.

130. Suarez G, Veliz M, Nagel R. Role of hydrophobic interactions in collagen fibril formation: effect of alkylureas in vitro. *Arch Biochem Biophys*. 1980;205(2):422-427.

131. George A, Veis A. FTIRS in H2O demonstrates that collagen monomers undergo a conformational transition prior to thermal self-assembly in vitro. *Biochemistry*. 1991;30:2372-2377.

132. Roeder B, Kokini K, Sturgis J, Robinson J, Voytik-Harbin S. Tensile mechanical properties of three-dimensional type I collagen extracellular matrices with varied microstructure. *J Biomech Eng*. 2002;124:214-222.

133. Erie J, McLaren J, Patel S. Confocal microscopy in ophthalmology. *Am J Ophthalmol*. 2009;148(5):639-646.

134. McLaren J, Bourne W, Patel S. Standardization of corneal haze measurement in confocal microscopy. *Invest Ophthalmol Vis Sci*. 2010;51:5610-5616.

135. Yang Y, Kaufman L. Rheology and confocal reflectance microscopy as a probe of mechanical properties and structure during collagen/hyaluronan self-assembly. *Biophys J*. 2009;96(4):1566-1585.

136. Yang Y, Leone L, Kaufman L. Elastic moduli of collagen gels can be predicted from dimensional confocal microscopy. *Biophys J*. 2009;97(7):2051-2060.

137. Beuerman RW, Pedroza L. Ultrastructure of the human cornea. *Microsc Res Tech*. 1996;33(4):320-335.

138. Bitar M, Salih V, Brown RA, Nazhad SN. Effect of multiple unconfined compression on cellular dense collagen scaffolds for bone tissue engineering. *J Mater Sci Mater Med*. 2007;18(2):237-244.

139. Girton T, Barocas V, Tranquillo R. Confined compression of a tissue-equivalent: collagen fibril and cell alignment in response to anisotropic strain. *J Biomech Eng*. 2002;124(5):568-575.

140. Vader D, Kabla A, Weitz D, Mahadevan L. Strain-induced alignment in collagen gels. *PLoS One*. 2009;4(6):e5902.

141. Braziulis E, Diezi M, Biedermann T, et al. Modified plastic compression of collagen hydrogels provides an ideal matrix for clinically applicable skin substitutes. *Tissue Eng part C Methods*. 2012;18(6):464-474.

142. Cheema U, Chuo C, Sarathchandra P, Nazhat SN, Brown R. Engineering functional collagen scaffolds: cyclical loading increases material strength and fibril aggregation. *Adv Funct Mater*. 2007;17(14).

143. Caliari SR, Harley BA. The effect of anisotropic collagen-GAG scaffolds and growth factor supplementation on tendon cell recruitment, alignment, and metabolic activity. *Biomaterials*. 2011;32(23):5330-5340.

144. Matthews JA, Wnek GE, Simpson DG, Bowlin GL. Electrospinning of collagen nanofibers. *Biomacromolecules*. 2002;3(2):232-238.

145. Zhong S, Teo WE, Zhu X, Beuerman RW, Ramakrishna S, Yung LYL. An aligned nanofibrous collagen scaffold by electrospinning and its effects on in vitro fibroblast culture. *J Biomed Mater Res part A2*. 2006;79(3):456-463.

146. Phu D, Wray LS, Warren R V, Haskell RC, Orwin EJ. Effect of subtrate composition and alignment on corneal cell phenotype. *Tissue Eng part A*. 2011;17(5 and 6):799-807.

147. Wray LS, Orwin EJ. Recreating the microenvironment of the native cornea for tissue engineering applications. *Tissue Eng part A*. 2009;15(7):1463-1472.

148. Guo C, Kaufman LJ. Flow and magnetic field induced collagen alignment. *Biomaterials*. 2007;28(6):1105-1114.

149. Lee P, Lin R, Moon J, Lee LP. Microfluidic alignment of collagen fibers for in vitro cell culture. *Biomed Microdevices*. 2006;8(1):35-41.

150. Lanfer B, Freudenberg U, Zimmerman R, Stamov D, Korber V, Werner C. Aligned fibrillar collagen matrices obtained by shear flow deposition. *Biomaterials*. 2008;29(28):3888-3895.

151. Saeidi N, Sander EA, Ruberti JW. Dynamic shear-influenced collagen self-assembly. *Biomaterials*. 2009;30(34):6581-6592.

152. Cheng X, Gurkan UA, Dehen CJ, et al. An electrochemical fabrication process for the assembly of anisotropically oriented collagen bundles. *Biomaterials*. 2008;29(22):2008.

153. Tranquillo R, Girton T, Bromberek B, Triebes T, Mooradian D. Magnetically oriented tissue-equivalent tubes: application to a circumferentially orientated media-equivalent. *Biomaterials*. 1996;17(3):349-357.

154. Torbet J, Malbouyres M, Builles N, et al. Orthogonal scaffold of magnetically aligned collagen lamellae for corneal reconstruction. *Biomaterials*. 2007;28(29):4268-4276.

155. Tidu A, Ghoubay-Benallaoua D, Lynch B, et al. Development of human corneal epithelium on organized fibrillated transparent collagen matrices synthesized at high concentrations. *Acta Biomater*. 2015;22:50-58.

156. Walsh JF, Manwaring ME, Tresco PA. Directional neurite outgrowth is enhanced by engineered meningeal cell-coated substrates. *Tissue Eng*. 2005;11(7-8):1085-1094. doi:10.1089/ten.2005.11.1085.

157. Boote C, Hayes S, Ahahussin M, Meek KM. Mapping collagen organization in the human cornea: left and right eyes are structurally distinct. *Invest Ophthalmol Vis Sci*. 2006;47(3):901-908.

158. Kirkwood J, Fuller G. Liquid crystalline collagen: a self-assembled morphology for the orientation of mammalian cells. *Langmuir*. 2009;25:3200-3206.

159. Huang N, Okogbaa J, Lee J, et al. The modulation of endothelial cell morphology, function, and survival using anisotropic nanofibrillar collagen scaffolds. *Biomaterials*. 2013;34(16):4038-4047.

160. Lanfer B, Seib F, Fruedenberg U, et al. The growth and differentiation of mesenchymal stem and progenitor cells cultured on aligned collagen matrices. *Biomaterials*. 2009;30:5950-5958.

161. Stylianou A, Yova D, Alexandratou E. Nanotopography of collagen thin films in correlation with fibroblast responsee. *J Nanophotonics*. 2013;7:073590-073591 - 16.

162. Lam CH, Hansen EA, Jansen C, Bryan A, Hubel A. The characterization of arachnoid cell transport II: paracellular transport and blood-cerbrospinal fluid barrier formation. *Neuroscience*. 2012;222:228-238.

163. Abahussin M, Hayes S, Knox Cartwright N, et al. 3D collagen orientation study of the human cornea using x-ray diffraction and femtosecond laser technology. *Invest Ophthalmol Vis Sci*. 2009;50(11):5159-5164.

164. Elsheikh A, Brown M, Alhasso D, Rama P, Campanelli M, Garway-Heath D. Experimental assessment of corneal anisotropy. *J Refract Surg*. 2008;24:178-187.

165. Birk D. Type V collagen: heterotypic type I/V collagen interactions in the regulation of fibril assembly. *Micron*. 2001;32:223-237.

166. Chakravarti S, Magnuson T, Lass JH, Jepsen KJ, LaMantia C, Carroll H. Lumican regulates collagen fibril assembly: skin fragility and corneal opacity in the absence of lumican. *J Cell Biol*. 1998;141:1277-1286.

167. Danielson K, Baribault H, Holmes D, Graham H, Kadler K, Iozzo R. Targeted disruption of decorin leads to abnormal collagen fibril morphology and skin fragility. *J Cell Biol*. 1997;136(3):729-743.

168. Rada J, Cornuet P, Hassell J. Regulation of corneal collagen fibrillogenesis in vitro by corneal proteoglycan core proteins. *Exp Eye Res*. 1993;56:635-648.

169. Habibi Y, Lucia L, Rojas O. Cellulose nanocrystals, chemistry, self-assembly, and applications. *Chem Rev*. 2010;110(6):3479-3500.

170. Peng B, Dhar N, Liu H, Tam K. Chemistry and applications of nanocrystalline cellulose and its derivatives: a nanotechnology perspective. *Can J Chem Eng*. 2011;9999:1-16.

171. Zhang J, Elder T, Pu Y, Ragauskas A. Facile synthesis of spherical cellulose nanoparticles. *Carbohydr Polym*. 2007;69(3):607-611.

172. Lu P, Hsieh Y. Preparation and properties of cellulose nanocrystals: rods, spheres, and networks. *Carbohydr Polym*. 82AD;2(2010):329-336.

173. Wang N, Ding E, Cheng R. Preparation and liquid crystalline properties of spherical cellulose nanocrystals. *Langmuir*. 2008;24(1):5-8.

174. Hamad W, Hu T. Structure-process-yield interrelations in nanocrystalline cellulose extraction. *Can J Chem Eng*. 2010;88(3):392-402.

175. Bai W, Holbery J, Li K. A technique for production of nanocrystalline cellulose with a narrow size distribution. *Cellulose*. 2009;16:455-465.

176. Bondeson D, Mathew A, Oksman K. Optimization of the isolation of nanocrystals from microcrystalline cellulose by acid hydrolysis. *Cellulose*. 2006;13:171-180.

177. Li W, Wang R, Liu S. Nanocrystalline cellulose prepared form softwood kraft pulp via ultrasonic-assisted acid hydrolysis. *BioResources*. 2011;6(4):4271-4281.

178. Elazzouzi-Hafraoui S, Nishiyama Y, Putaux J, Heux L, Dubreuil F, Rochas C. The shape and size distribution of crystalline nanoparticles prepared by acid hydrolysis of native cellulose. *Biomacromolecules*. 2007;9(1):57-65.

179. Greminger G, Savage A. Methylcellulose and its derivatives. In: Whistler R, BeMiller J, eds. Vol New York: Academic Press Inc; 1959:580.

180. Orwin E, Boren M, Hubel A. Biomechanical and optical characteristics of corneal stromal equivalent. *J Biomech Eng*. 2003;125(4):439.

181. Crabb R, Hubel A. Influence of matrix processing on the optical and biomechanical properties of a corneal stroma equivalent. *Tissue Eng part A*. 2008;14(1):173-182.

182. Duncan T, Tanaka Y, Shi D, Kubota A, Quantock A, Nishida K. Flow-manipulated, crosslinked collagen gels for use as corneal equivalents. *Biomaterials*. 2010;31(34):8996-9005.

183. Liu Y, L G, Carlsson D, et al. A simple, cross-linked collagen tissue substrate for corneal implantation. *Invest Ophthalmol Vis Sci*. 2006;47(5):1869-1875.

184. Crabb R, Chau E, Evans M, Barocas V, Hubel A. Collagen film-based corneal stroma equivalent. *Tissue Eng*. 2006;12(6):1565-1575.

185. Fagerholm P, Lagali N, Carlsson D, Merrett K, Griffith M. Corneal regeneration following implantation of a biomimetic tissue-engineered substitute. *Clin Transl Sci*. 2009;2(2):162-164.

186. Coradin T, Allouche J, Boissiere M, Livage J. Sol-gel biopolymer/silica nanocomposites in biotechnology. *Curr Nanosci*. 2006;2:219-230.

187. Brasack I, Bottcher H. Biocompatibility of modified silica-protein composite layer. *J Sol-Gel Sci Technol*. 2000;19:479-482.

188. McLaren J, Brubaker R. Measurement of transmission of ultraviolet and visible light in the living rabbit cornea. *Curr Eye Res*. 1996;15(4):411-421.

189. Menovsky T, Beek J, van Gemert M. Effect of the CO2 milliwatt laser on tensile strength of microsutures. *Lasers Surg Med*. 1997;20:64-68.

190. Haynes W. Optical properties of selected organic and inorganic materials. In: *CRC Handbook of Chemistry and Physics*. Vol 92nd ed. Boca Raton, FL: CRC Press/Taylor and Francis; 2012:163-164.

191. Patel S, Marshall J, Fitzke F. refractive-index of the human corneal epithelium and stroma. *J Refract Surg*. 1995;11:100-105.

192. Besseau L, Giraud-Guille M. Stabilization of fluid cholesteric phases of collagen to ordered gelated matrices. *J Mol Biol*. 1995;251:197-202.

193. Erie J, McLaren J, Patel S. Confocal microscopy in ophthalmology. *Am J Ophthalmol*. 2009;148:639-646.

194. McLaren J, Dinslage S, Dillon J, Roberts J, Brubaker R. Measuring oxygen tension in the anterior chamber of rabbits. *Invest Ophthalmol Vis Sci*. 1998;39:1899-1909.

195. DiVito M, Rudisill S, Stein A, Patel S, McLaren J, Hubel A. Silica hybrid for corneal replacement: optical, biomechanical, and ex vivo biocompatibility studies. *Invest Ophthalmol Vis Sci*. 2012;53(13):8192-8199.

196. Eglin D, Shafran K, Livage J, Coradin T, Perry C. Comparative study of the influence of several silica precursors on collagen self-assembly and of collagen on "Si" speciation and condensation. *J Mater Chem*. 2006;16(43):4220-4230.

197. Casper P. Automated depth scanning confocal microspectrometer for rapid in vivo determination of water concentration profile in human skin. *Raman Spectrosc*. 2000;31:813-818.

198. Matos M, Ilharco L, Almeida R. The evolution of TEOS to silica gel and glass by vibrational spectroscopy. *J Non Cryst Solids*. 1992;147:232-237.

199. Bertoluzza A, Fagnano C, Morelli M. Raman and infrared spectra on silica gel evolving toward glass. *J Non Cryst Solids*. 1982;48:117-128.

200. Boissiere M, Meadows P, Brayner R, Helary C, Livage J, Coradin T. Turning biopolymer particles into hybrid capsules: the example of silica/alginate nanocomposites. *J Mater Chem*. 2006;16:1178-1182.

201. Zhu S, Xiang J, Li X, et al. Poly(L-lysine)-modified silica nanoparticles for the delivery of antisense oligonucleotides. *Biotechnol Appl Biochem*. 2004;39(2):179-187.

202. Liz-Marzan L, Giersig M, Mulvaney P. Synthesis of nanosized gold-silica core-shell particles. *Langmuir*. 1996;12(18):4329-4335.

203. Van Ooij W, Zhu D, Jayaseelan S, Fu Y, Teredesai N. Silane based chromate replacements for corrosion control, paint adhesion, and rubber bonding. *Surf Eng*. 2000;16:386-396.

204. Nyquist G. Rheology of the cornea: experimental techniques and results. *Exp Eye Res*. 1968;7(2):183-188.

205. Simonsen A, Andreassen T, Bendix K. The healing strength of corneal wounds in the human eye. *Exp Eye Res*. 1982;35(3):287-292.

206. Jalbert I, Stapleton F, Papas E, Sweeney D, Coroneo M. In vivo confocal microscopy of the human cornea. *Br J Ophthalmol*. 2003;87(2):225-236.

207. Guthoff R, Zhivov A, Stachs O. In vivo confocal microscopy, an inner vision of the cornea - a major review. *Clin Experiment Ophthalmol*. 2009;37(1):100-117.

208. Auran J, Koester C, Kleiman N, et al. Scanning slit confocal microscopic observation of cell morphology and movement within the normal human anterior cornea. *Ophthalmology*. 1995;102(1):33-41.

209. Leonard D, Meek K. Refractive indices of the collagen fibrils and extrafibrillar material of the corneal stroma. *Biophys J*. 1997;72:1382-1387.

210. Katz E, Li S. The intermolecular space of reconstituted collagen fibrils. *J Mol Biol*. 1973;73:351-369.

211. Hodge A, Petruska J. *Aspects of Protein Structure. Vol. 1*. Vol (Ramachandran G, ed.). New York: Academic Press; 1963.

Appendix

A.1 Corneal Fibril Unit Cell

Throughout Chapter 4, fibril spacing was quantified by using the unit cell (Figure A.1) Meek and Leonard used for the cornea[34]. Even though hydrogels made *in vitro* differ significantly from this ideal configuration, it was convenient to report fibril spacings of hydrogels as nearest neighbor distances if this configuration was assumed. In Figure A.1, the circles represent the cross-sections of fibrils that have directions normal to the viewing plane. Each cell is composed of four fibrils that make corners of an equilateral parallelogram. The diameter of each fibril is denoted as d, the interfibrillar spacing as D, and the Bragg spacing as p.

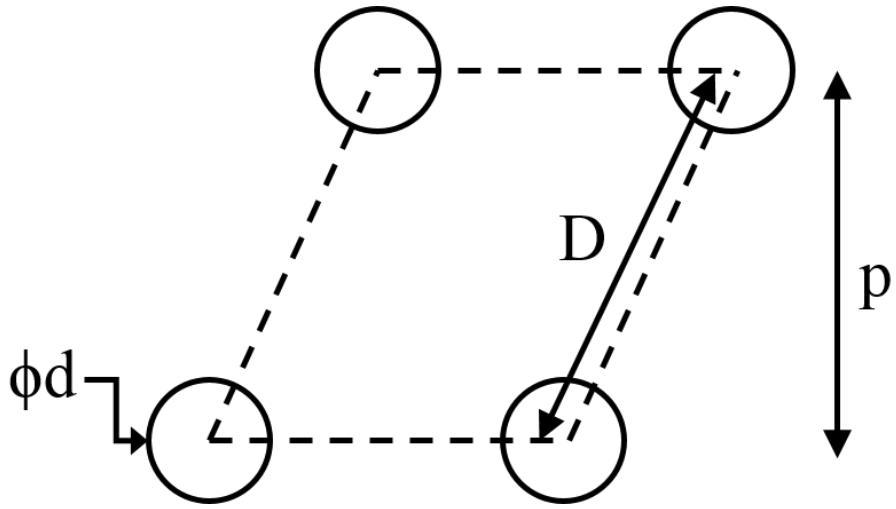

Figure A.1: Unit cell reported by Meek and Leonard that approximates the corneal stroma microstructure[34]

According to Meek and Leonard[34], D is approximately equal to 1.12p. Considering that each unit cell contains one fibril on average, the fibril volume fraction reduces to Equation A.1.

$$Fibril\ Volume\ Fraction = 1.12 * \frac{\pi d^2}{4D^2} \quad \text{(Eq. A.1)}$$

A.2 Fibril Spacing Quantification

There are two ways to quantify fibril spacing of a collagen hydrogel. The experimental method involves counting the number of fibrils F that are in a TEM cross-sectional image of a known area A. By assuming the microstructure shown in Figure A.1, the next neighbor distance can be calculated using Equation A.2.

$$D = 1.12[F/A]^{-1/2} \quad \text{(Eq. A.2)}$$

If the collagen concentration C (in mg/mL), and average fibril diameter d are known, the next neighbor spacing can be estimated using geometrical arguments and experimental data reported for type I collagen fibrils. Details of this derivation can be found in the work reported by Leonard and Meek[209]. Using the experimental values listed in Table A.1 for type I collagen, Equation A.3 was derived.

$$D = 23.5\sqrt{\frac{d^2}{C}} \quad \text{(Eq. A.3)}$$

Table A.1: Experimental values found for type I collagen molecules and fibrils used in the derivation of Equation A.3.

Property	Value	Reference
Partial specific volume	0.71 mL/g	Katz and Li, 1973[210]
D-Period	65 nm	Meek and Leonard, 1993[34]
Molecular weight	283 kDa	Katz and Li, 1973[210]
Intermolecular Bragg spacing	1.63 nm	Meek and Leonard, 1993[34]
Packing angle of molecules	60°	Katz and Li, 1973[210]
Gap between molecules	0.6*D-period	Hodge and Petruska, 1963[211]